Gamma-Ray Imaging Observations
of Supernova 1987A

Thesis by

David M. Palmer

In Partial Fulfillment of the Requirements

for the Degree of

Doctor of Philosophy

California Institute of Technology

Pasadena, California

1992

(Submitted February 28, 1992)

Acknowledgements

I would like to thank my parents, Leigh and Evelyn, my sister, Andie, and my brothers, Eric and Aaron. After being born into the right family, all other choices and chances are unimportant.

I would also like to thank my advisor, Tom Prince.

This work would not have been possible without all the people who designed, built, and worked on GRIP over the past decade: Bill Althouse, Dan Burke, Wally Campbell, Rick Cook, Alan Cummings, Mark Finger, Marty Gould, John Grunsfeld, William Heindl, Steve Schindler, Chris Starr, Edward Stone, James Weger, and the people of Caltech's Central Engineering Services. This work would not have been as pleasant without the other members of Caltech's Space Radiation Labs—especially my officemates Deepto Chakrabarty, Eric Christian, Andrea Ghez, J. Eric Grove, Jeff Hammond, and Alycia Weinberger.

The balloon launches were handled by the personnel of the National Scientific Balloon Facility, who deserve recognition and gratitude for their skill and support.

Abstract

The Caltech imaging γ-ray telescope has made four balloon flights from Alice Springs, Australia, to observe the hard X-ray and γ-ray emission from Supernova 1987A as it evolved between 1987 May and 1989 April. We have detected γ-rays with the time behavior and spectral signature expected from freshly-synthesized radioisotopes embedded in a cloud of ejecta. In particular, we detect the 847 and 1238 keV γ-ray lines produced by the decay of ^{56}Co, and the continuum spectrum expected from Compton scattering of these γ-rays. The results of these observations are compared with other measurements and with theoretical models of supernovae, and it is found that our results are consistent with core-collapse models for SN 1987A in which the centrally-produced radioisotopes have propagated outwards to mix with the ejecta.

Table Of Contents

List of Figures

List of Tables

Chapter 1
Introduction

A supernova is an exploding star: a sudden fireball that, for a few months, becomes hundreds of millions of times more luminous than the Sun.

Supernovae are not merely spectacular, they play an important role in the evolution of the universe, including the parts of the universe that affect us directly. These explosions create and disperse heavy elements—it is believed that most of Earth's material was ejected by supernovae. It has also been suggested that supernovae accelerate cosmic rays, trigger star formation, and may even have helped to shape the early universe.

Using observations of supernovae and supernova remnants, theorists have developed models to explain these dramatic events. Until recently, however, there had been no supernovae during the era of modern instrumentation close enough to provide rigorous tests of these theories.

In February, 1987, the supernova SN 1987A exploded in the Large Magellanic Cloud, a satellite galaxy to ours just 50 kiloparsecs (kpc) away. This was the closest known supernova since before the invention of the telescope, and the first chance to study a nearby supernova with the array of astronomical tools that had been developed since the days of naked eye astronomy. SN 1987A has

been observed with almost every major instrument capable of pointing at it, at wavelengths from the radio to ultra-high energy γ-rays, and in neutrinos. A large fraction of the astronomical community's total resources has been dedicated to this one object.

γ-ray telescopes, developed within the past few decades, are important tools for understanding this once-in-a-lifetime event. The high-energy processes in exploding stars are well matched by the energies observed in γ-ray astronomy. After the first few months, most of the energy emitted by a supernova is originally produced as γ-rays and is visible at optical and lower frequencies only because it is scattered, absorbed, and re-radiated in the cloud of ejecta thrown off by the supernova.

This thesis describes the Caltech γ-ray observations of SN 1987A. We made four observations using a balloon-borne imaging telescope, and found that the high-energy flux from the supernova bore the spectral signatures and time behavior of freshly created radioactive material in an expanding ejecta cloud. These measurements have provided a greater understanding of at least one type of supernova.

1.1   Motivation for γ-Ray Observations

It had been expected for decades that γ-ray observations of supernovae would be useful to the understanding of these events. Measurements of γ-rays from a supernova would provide information about supernova nucleosynthesis, and about the other processes that occur during the early stages of the explosion. γ-ray emissions could be a major component of the total energy output of the supernova, and so it would be important to measure them in order to determine the sources contributing to the supernova luminosity. The γ-ray spectrum is

expected to evolve over time as different radioisotopes decay and as non-radioactive sources, such as a central compact object, become relatively more important. As a result, γ-ray measurements can be used to determine the final state of the supernova remnant.

Fowler & Hoyle (1964) predicted on the basis of theoretical calculations that ^{56}Ni (which decays with a 6 day half-life to the longer-lived radioisotope ^{56}Co) would be synthesized in large quantities by supernovae. Before SN 1987A, the primary astronomical observational evidence for this was the evolution of supernova luminosities at late times ($\gtrsim$ a few months), which is consistent with the power output that would be expected from the decay of ^{56}Co. These light curves decline with exponential time constants of 70-140 days, depending on the type of supernova (Doggett & Branch 1985). For comparison, the decay time of ^{56}Co is $\tau_{1/e} = 111$ days. Atomic cobalt lines detected in the infrared spectrum of a supernova (Woosley, Axelrod & Weaver 1981) provided additional evidence of ^{56}Ni production.

Clayton, Colgate & Fishman (1969) predicted that future γ-ray telescopes might be able to directly detect the γ-rays emitted by decaying radioisotopes. Because the radioisotopes are predicted to be produced near the center of the exploding star (for some types of supernovae), the absorption and scattering of the γ-rays would provide information about the spatial structure of the supernova ejecta (Clayton 1974). It would also be possible to tell whether the radioisotopes remain near the center of the ejecta, or are distributed outwards by hydrodynamic instabilities and other effects.

γ-rays that do not escape the supernova are absorbed by the ejecta, providing heat which is re-radiated as UV, optical, and IR (UVOIR) photons.

After a few months, during which the initial energy of the supernova explosion is radiated away, the total γ-ray and UVOIR luminosity provides a good approximation to the continuous power production within the supernova. Deviations of this luminosity from the exponential decay expected for ^{56}Co would indicate the presence of additional power sources.

Possible additional power sources include other radioisotopes, such as ^{57}Co ($\tau_{1/e}$= 391 days) and ^{44}Ti ($\tau_{1/e}$= 68 years), or the energy produced by a central compact object, such as an accreting black hole or neutron star. The detection of other isotopes would constrain theories of nucleosynthesis and of stellar interiors. If either a black hole or a neutron star were detected, this would constrain theories of nuclear and particle physics as well as of supernovae.

1.2 γ-Ray Observations

When SN 1987A was discovered, predictions were made, based on simplifying assumptions, that detectable levels of γ-rays would not be able to escape from the supernova ejecta until almost a year after the explosion (*e.g.,* Chan & Lingenfelter 1987; Ebisuzaki & Shibazaki 1988b; Woosley, Pinto & Ensman 1988). The explicit simplifications included ignoring predicted processes which could result in earlier emergence of γ-ray flux (Falk & Arnett 1973), but the magnitude of these processes and the extent to which they would affect the evolution of the flux was not predictable.

As the first known supernova in the era of γ-ray astronomy close enough to potentially be visible in γ-rays, any measurements or upper limits of SN 1987A's high energy emissions would be enlightening. A week after the discovery of the supernova, NASA issued an Announcement of Opportunity to fly X-ray and γ-ray telescopes on balloons and rockets (Riegler 1987). The first

balloon payload, which included a high-energy spark-chamber telescope that had been in storage for over a decade, observed SN 1987A less than eight weeks after its discovery (Sood *et al.* 1988).

The second balloon payload, the Caltech Gamma-Ray Imaging Payload (GRIP), is the instrument which made the measurements that are the focus of this thesis. We flew GRIP a total of four times in a two-year period from Alice Springs, Australia, to observe SN 1987A.

In addition to the balloon observations, which eventually totaled more than two dozen flights using over a dozen different instruments, space-based instruments also observed the γ-ray emissions of SN 1987A. The observations made by these γ-ray instruments are summarized in Chapter 7. As will be discussed, these measurements of the high-energy emission from SN 1987A have made a significant contribution to the understanding of supernovae.

1.3   Summary

Chapter 2 is a discussion of the theories and models which have been developed to explain supernovae in general and SN 1987A in particular.

Chapter 3 describes the Caltech imaging instrument which was used to make these observations.

Chapter 4 gives the details of each of the four observations of SN 1987A made with this instrument.

Chapter 5 describes our analytical procedure, including a comparison of imaging and non-imaging techniques.

Chapter 6 describes the results of our observations and analysis, including the measured γ-ray spectrum of SN 1987A.

Chapter 7 is a discussion and summary of these results. To demonstrate some of the basic techniques employed in understanding the evolution of the supernova based on our measurements, I use our data to reject a simple model for the structure of the SN 1987A ejecta. I then compare our measurements with those obtained using other instruments, and with the more detailed models described in Chapter 2. I parameterize our observations in terms of the escaped energy and X-ray and γ-ray photons, and compare that to the results of optical observations. I also describe future measurements which may provide additional understanding of SN 1987A.

Chapter 8 presents the general conclusions of this thesis.

The appendices supply details of some of the more technical aspects of the GRIP instrument. Appendix A describes the coded aperture imaging technique used in GRIP. γ-ray measurements made using imaging techniques are affected more by inaccuracies in the instrument pointing direction than measurements made using more traditional techniques. However, the imaging technique also provides information which allows these effects to be controlled. Appendix B places limits on these pointing effects. Appendix C gives the details of our observations, including the line-of-sight atmospheric depths and the timing of our observation sequences.

Chapter 2
Theory and Models

Before SN 1987A, the observational data on supernovae were very limited. Since the invention of the telescope and other astronomical instruments there had been no detected supernovae nearer than the Andromeda Galaxy. As a result, observations of most supernovae have been at visible wavelengths, starting an unknown time after the initial explosion, and usually continuing for only a few months after discovery. From these earlier observations, classification schemes had been developed for supernovae and theories developed to explain each class. Because of the narrow scope of observations for most supernovae, these theories were not heavily tested.

SN 1987A, on the other hand, has been observed across the electromagnetic spectrum from radio to γ-rays and in neutrinos, beginning with optical observations of the progenitor star well before the explosion and continuing to the present. As a result, theories and models of SN 1987A are much more dependable than those of other supernovae, and our understanding of supernovae in general, especially those similar to SN 1987A, is on a much firmer footing than it was before 1987.

Much of the description that follows is taken from a review article by Arnett, Bahcall, Kirshner, & Woosley (1989a), written in 1989, after two years of SN 1987A observation.

2.1   Types of Supernovae

Supernovae are believed to occur by two different mechanisms. Some supernovae are powered by the rapid and catastrophic fusion burning of white dwarfs. Others are powered by gravitational collapse in supergiants: massive, young, bright stars.

Despite the dramatic differences in the physical processes of these two types of supernovae, the gross observable effect of both is similar: the sudden appearance of a brilliant object which releases $\sim 10^{51}$ ergs of kinetic and electromagnetic energy into its environment and then slowly dims.

The difference in mechanisms is not reflected in the standard nomenclature, which is based on observational, rather than theoretical, differences and similarities. The taxonomy is based on the presence or absence of lines in the optical spectrum, and on the time-dependence of the light curve. Figure 2.1, adapted from a review paper by Harkness & Wheeler (1990), shows the basic classification scheme.

Gravitational collapse certainly powered SN 1987A, and probably powered most other Type II supernovae are as well. Type Ib and Ic supernovae are also widely believed to be gravity powered. Type Ia supernovae, on the other hand, are almost certainly fusion powered.

Many supernovae are unique in one respect or another, leading to classifications such as IIpec (peculiar). SN 1987A may be considered Type IIpec, since it is neither a Type IIP nor a Type IIL, but other low-luminosity Type II

SUPERNOVA CLASSIFICATION

Maximum light spectra

H /*no* H

SN II

Light curve shape

II L   II P   II peculiar   SN 1987A

SN I

Si /*no* Si

Ia

He /*no* He

Ib   Ic
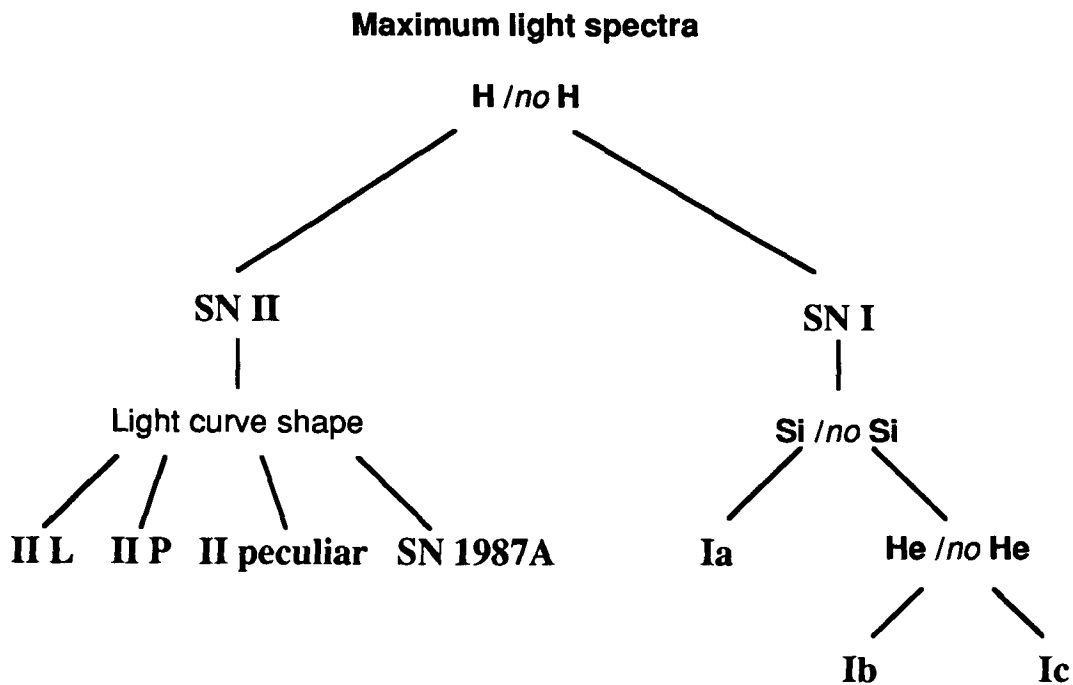
<u>Figure 2.1</u> — The observational classification scheme of supernovae based on lines in the optical spectrum at maximum light. Type II supernovae have hydrogen lines, Type I supernovae do not. Type II supernovae are subclassified by the shape of their light curve: "II Linear," "II Plateau," and "II peculiar." This last class includes SN 1987A and many other supernovae with behavior atypical of Types IIL and IIP. Type I supernovae with silicon lines tend to follow the light curve of Figure 2.2 and, if so, are called Type Ia. Adapted from Harkness & Wheeler (1990).

plateau supernovae similar to SN 1987A have been observed (Young & Branch 1989) and so SN 1987A may be the prototype of a newly recognized class. Type Ia supernovae tend to be similar to each other, but the other classes show wide variations among their members.

2.1.1   Type Ia (Fusion-Powered) Supernovae

According to current theory, Type Ia supernovae are believed to originate as white dwarf stars, consisting primarily of carbon and oxygen (^{12}C and ^{16}O) (although O-Ne-Mg white dwarfs have also been suggested as Type Ia progenitors (Isern, Canal & Labay 1991)). If the mass of such a star is below the Chandrasekhar limit of ~1.4 solar masses ($M_\odot$), the pressures and temperatures of the star's interior are not high enough to burn the carbon and oxygen to heavier elements, and so it simply sits quiescently, supported by the pressure of its degenerate electrons. If the star accumulates additional mass from a companion star, the pressure can reach a critical value and reignite the star. From the point of ignition, a wave of nuclear combustion spreads to engulf the entire star. A large fraction of the material suddenly and explosively burns to heavy elements, leaving behind nothing but a rapidly expanding cloud of debris.

Type Ia supernovae tend to be very similar to each other, which is evidence for the critical mass aspect of this model. Figure 2.2, taken from Doggett & Branch (1985), shows a composite light curve of 38 different Type I supernovae, demonstrating their similarity. However, there are examples of peculiar Type Ia supernovae, and small but unambiguous variations among non-peculiar Type Ia's. For example, SN 1991T initially had a unique spectrum which later evolved into a more typical Type Ia spectrum, suggesting a physically distinct explosion mechanism (Filippenko *et al.* 1992). These variations are

usually detectable only because of observations that are more complete in time or spectral coverage than those available for the majority of supernovae.

2.1.2   Core Collapse Supernovae

The other standard supernova mechanism is driven by the energy released in the gravitational collapse of a massive ($\geq$12 M$\odot$) star.

Such stars live short lives; tens of millions of years. At the high pressures and temperatures of the interiors of these stars, the original hydrogen and helium is burned in fusion reactions to progressively heavier and heavier elements, releasing energy that heats and expands the star to support it against its own
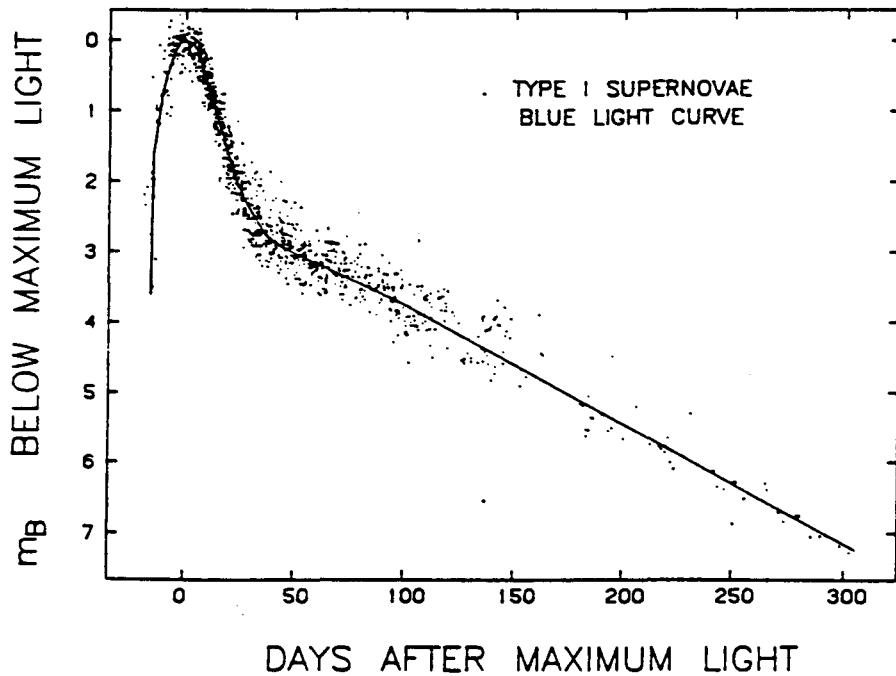
Figure 2.2 — Composite photographic (B band) light curve of 38 Type I supernovae. Taken from Dogget & Branch (1985).

weight. The dependence of the reaction rates with temperature and pressure allows the star to maintain homeostatic equilibrium (with a radius and temperature which vary as the star evolves) for as long as the star has fuel it can burn.

Synthesis of the heavier elements requires higher temperatures and pressures than the earlier hydrogen- and helium-burning stages. These high temperature reactions emit almost all of their energy in the form of neutrinos, which immediately escape. Only a small fraction of the generated power is retained in the star, requiring a much greater total power to moderate the burning. For a 20 $M_\odot$ star, the hydrogen burning stage lasts for ten million years and the helium burning stage for 1 million years, but the final step of burning 1.4 $M_\odot$ of silicon to iron takes only 2 days (Arnett *et al.* 1989a). During the silicon burn, the rate of energy production is 10^7 times as much as that during the hydrogen burn, but the power delivered to the star is not even doubled. 99.99998% of the energy produced at the center of the star in this stage is ghosted away by neutrinos.

After the material has fused to produce iron nuclei, further reactions would absorb energy rather than release it. The center of the star burns out first and forms an inert core of iron, supported by electron degeneracy pressure. Around this core are successive shells of still-burning lighter elements, arranged in an onion-like structure (see Figure 2.3).
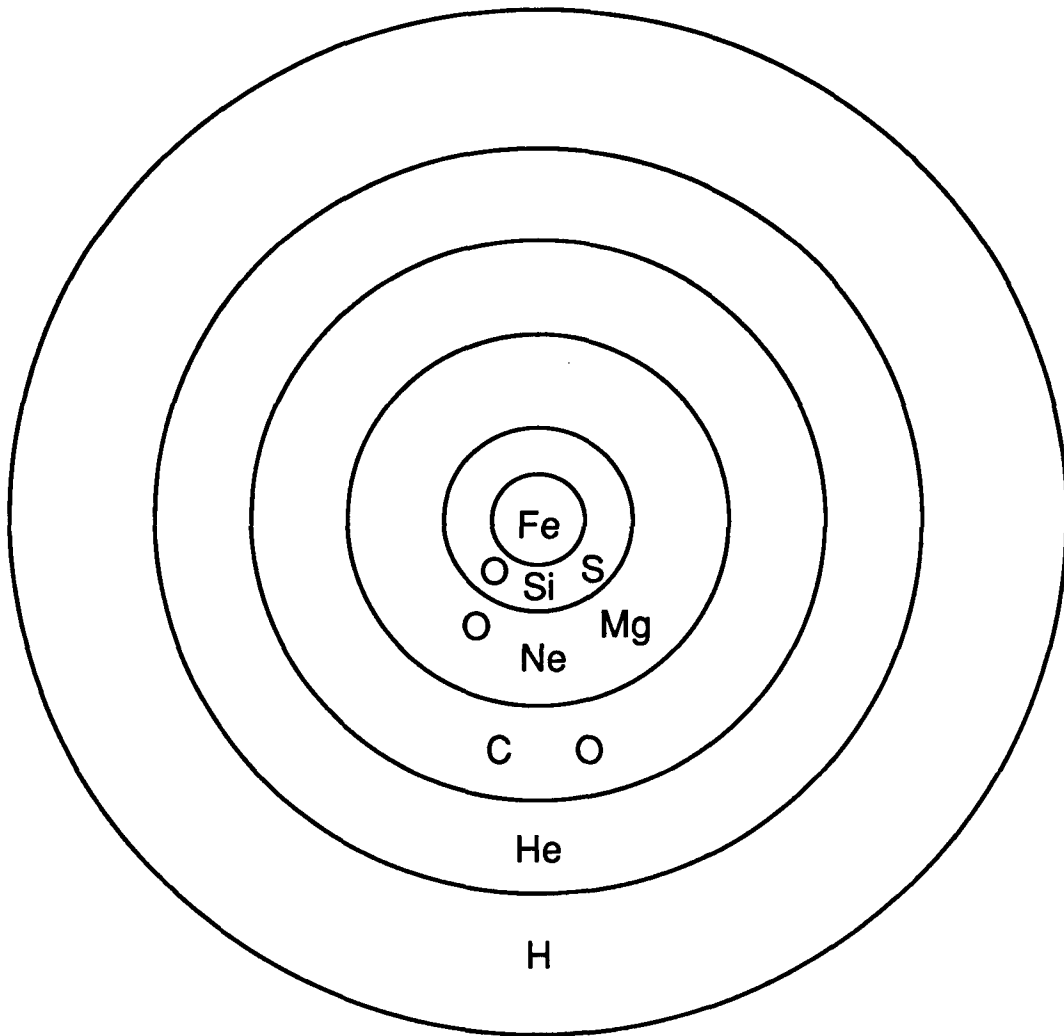
Figure 2.3 — The structure of a massive star at the onset of core collapse. The labels refer to the dominant elements in each layer. This figure is not to scale; SN 1987A's progenitor was ~40× the radius of the Sun but the iron core was approximately the same size as Earth, so a scale drawing would show the iron core as a dot 0.03 mm across. Based on Woosley & Weaver (1986).

When enough material has burned to iron, the core reaches a critical mass ($\sim$1.4 $M_\odot$) and the pressure at the center of the star is greater than can be supported by the degeneracy pressure of the electrons. The core collapses to several times nuclear density, a reduction in volume of six orders of magnitude, and then rebounds. The surrounding material, left unsupported by the collapse, falls inwards until it encounters the rebounding core. The resulting collision produces a shock wave that propagates outwards through the star. Exterior to the core, the shock wave hydrodynamically heats $\sim$0.08 $M_\odot$ of material to a temperature in excess of 5×10^9 K. At this temperature, the material rapidly burns in explosive nucleosynthesis to nuclear statistical equilibrium. This fully-processed material consists almost entirely of iron-group elements, primarily ^{56}Ni, with sufficient quantities of other isotopes (*e.g.*, ^{57,58}Ni, ^{61,62}Zn) to retain the pre-shock neutron-proton ratio (Thielemann *et al.* 1990), and small quantities of heavier elements. The shock wave cools as it propagates outwards from the core region. The $\sim$0.2 $M_\odot$ of material outside the newly-formed nickel shell reaches a temperature above 2×10^9 K and only partially burns, producing elements below the iron group. The remaining 90% of the star, while thrown explosively outwards by the shock, does not experience explosive nucleosynthesis and retains the elemental and isotopic composition developed during the sustained burning of the progenitor.

Neutrinos play an important part in the dynamics of the initial explosion. Some of these neutrinos are produced by electron capture on protons driven by the extreme pressure in the collapsing core, producing neutrons and electron neutrinos. The densities and temperatures in the collapsed core are high enough that all types of neutrinos and anti-neutrinos are produced thermally and reach significant densities (see, *e.g.*, Myra & Burrows 1990). During the collapse the

neutrinos are confined in the core, and act as a Fermi gas to provide pressure. As the core rebounds and becomes less dense (but still much denser than the original degenerate iron core) the neutrinos leak out of the core. These neutrinos may play a role in driving the shockwave outwards through the infalling material. Once the neutrinos emerge outside of the shock front, they do not affect the low (stellar) density unshocked material, and escape from the star without further interaction.

Core collapse supernovae are a hundred times more energetic than Type Ia supernovae. However, 99% of the energy ($\sim 10^{53}$ ergs) is emitted in the form of neutrinos. The quantity of energy that remains for powering the kinetic energy of the explosion and the electromagnetic emission is similar to that produced by the thermonuclear reactions in a Type Ia supernova. Core collapse supernovae tend to have a much wider variety of behavior than Type Ia supernovae, even though they are both triggered by the buildup of a critical mass. The collapsing cores are all similar, but the envelopes surrounding them may have large differences in mass, density, and other parameters, resulting in a wide range of observational properties. For example, a Type Ib or Ic supernova may be the result of a core collapse in a star which had previously ejected the hydrogen layer of its envelope.

2.1.3   Potential Variations and Other Mechanisms

Variations on these two main models have been proposed.

Fusion-powered supernovae need not conform to the narrow observed range of typical Type Ia behavior. An exploding white-dwarf-equivalent core embedded in a stellar envelope would be observationally similar to an ordinary Type II supernova (references are in Woosley 1990). This "Type I$_{\frac{1}{2}}$" supernova

would not produce large quantities of neutrinos, and would be several times more luminous than a core-collapse Type II at late times, but since only one supernova has ever been observed as a neutrino source, and most supernovae are too distant to allow detailed study of the tail of the light, these differences would typically go unnoticed.

A "neutrino bomb" is a postulated variation on a core collapse supernova (see Bahcall 1989 for references). Many computer models of supernovae fail to explode, and there is some speculation that these fizzled models may represent a subclass of real events. If the shock wave from the core bounce is not strong enough, and if the neutrinos are unable to push it outwards, the shock may die out and be swept back into the core by infalling material. The whole star would collapse onto itself, leaving only a black hole. All that would escape from such an event is a burst of neutrinos formed in the collapse.

Another suggested variation on a Type II, for stars of mass ~8-12 $M_\odot$, is the collapse of an O-Ne-Mg core, rather than the conventional Fe core collapse of stars $\geq 12 M_\odot$ (Miyaji, Nomoto & Sugimoto 1980; Schwartz, Wheeler & Harkness 1991). Under different conditions, an O-Ne-Mg core may ignite and totally disrupt the star, producing a fusion-powered supernova which leaves no collapsed core remnant.

These models and variations, and any others that may be invented, are not mutually exclusive. Supernovae are being discovered at a rapidly increasing rate (34 were reported in the first six months of 1991 compared to 18 in all of 1985) and a large fraction of these are either unique or unusual in some aspect or another. Any physically reasonable model may describe some subset of supernovae without invalidating the models which describe others.

2.2   Observations of SN 1987A

On February 24, 1987, Ian Shelton discovered a supernova in the Large Magellanic Cloud (LMC), only 50 kiloparsecs (kpc) away (Shelton 1987). This was the nearest and brightest supernova to be discovered since Kepler's supernova of 1604, and it rapidly became the most intensely studied extragalactic object ever.

The most basic observations of SN 1987A made in the period before γ-rays were detected, and their implications, are:

1) SN 1987A is at the same location as a previously-studied blue supergiant star.

2) A burst of neutrinos came from the direction of the supernova 3 hours before the first detected optical brightening (Bionta *et al.* 1987; Hirata *et al.* 1987). The number and energies of the neutrinos were consistent with standard models of core collapse supernovae.

3) The presence of hydrogen lines in the spectrum classifies SN 1987A as a Type II.

4) The light-curve in the infrared-ultraviolet region indicates that radioisotopes are an important source of energy for the supernova's luminosity after the first few months.

2.2.1   The Progenitor Star

By examining archival photographic plates made prior to the explosion of the supernova, it was determined that the star that exploded was a blue supergiant that had been catalogued by Sanduleak and given the designation Sk –69 202. This was only the second time that a supernova's progenitor star had been identified. (The only other supernova with an identified progenitor was the

extremely anomalous SN 1961V (see Doggett & Branch 1985) which is the prototype of the rare Type V.)

From these archival observations of Sk -69 202 and subsequent observations of SN 1987A, compared with models of stellar evolution and of core collapse supernovae, a reasonably complete description of the progenitor star has been compiled.

Sk -69 202, in its final stages, had a luminosity of approximately 4×10^{38} erg s^{-1} ($\sim10^5$ L$_\odot$). Its original (main sequence) mass was in the range 16–22 M$_\odot$, of which 5–7 M$_\odot$ formed a layered core of helium and heavier elements at the time of the explosion. A ~10 M$_\odot$ hydrogen envelope surrounded the core. The remainder of the original mass, perhaps a few M$_\odot$, was lost at some time during the star's evolution, and was later seen around the star after it was ionized by an initial ultraviolet flash from the supernova. As a B3 I supergiant, Sk -69 202 had a surface temperature of $\sim16{,}000$ K, and a radius of $3(\pm1)\times10^{12}$ cm.

2.2.1.1   A Blue Star

The identification of SN 1987A with the blue supergiant Sk -69 202 met some resistance at first, because at that time it was believed that only red supergiants could become supernovae. This belief was based on models of massive stars at the ends of their lives and the agreement between observed supernova behavior and models of core collapse in red supergiants, although blue supergiant supernovae had been suggested in the literature (referenced in §3 of Arnett *et al.* (1989a)).

It is now believed that Sk -69 202 had been a red supergiant at some time in its past, and later turned blue. During its red phase it ejected part of its

envelope, which became visible as an excitation nebula of material ionized by the supernova's initial UV flash (see §2.2.2). Modelling suggests that a supergiant may be blue at the end of its life if it has a low metallicity. Metallicity is the fraction of the original material in the star that is in the form of elements heavier than helium. High-metallicity stars such as our Sun, called Population I stars, are believed to include material that has already been partially burned and expelled by other stars, while the matter in low-metallicity Population II stars is closer to the primordial composition of hydrogen and helium. Population I stars are common in the disks of spiral galaxies, while stars in irregular galaxies, such as the LMC, are more likely to be Population II.

For two supergiant stars with the same mass and at the same stage of life, a Population II star will be bluer than a Population I star. The metals in a Population I star increase the opacity of the stellar envelope, allowing the net outward photon flux from the core to support and expand the star into a large-radius red supergiant. The envelope of a metal-poor Population II star is more transparent, and so it requires more energy production at the center to support it. This results in a hotter, more compact, and more energetic star; a blue supergiant.

Models predict that supernovae that start as blue supergiants tend to be dimmer than those that start as red supergiants. SN 1987A, at absolute photographic magnitude $M_B = -14$, was a factor of ~10 dimmer than what was considered typical of Type II SNe. The lower luminosity makes metal-poor supernovae much less likely to be detected. The lack of observed Type II supernovae in metal-poor galaxies led to the (fallacious) rule of thumb that Type II supernovae are found among Population I stars.

2.2.2 The SN 1987A UVOIR Light Curve

The "UVOIR" light curve of SN 1987A, the total power radiated by the supernova in the *Ultra*Violet, *O*ptical, and *Infra*Red bands, is shown in Figure 2.4. This is sometimes called the bolometric light curve, although the true bolometric light curve must include power emitted at other wavelengths as well. UVOIR luminosity measurements are based primarily on ground-based observations. These are much easier to obtain than satellite or balloon measurements of γ-rays, and so the dataset is denser, more precise, and more complete than the high-energy dataset.

The shape of the light curve is understood, and forms most of the basis for models of SN 1987A. The sequence of events that produces this light curve is as follows:

An initial spike in luminosity occurs as the shock wave reaches the surface of the star, heating it to $\sim 10^5$ K, reaching a peak intensity in the ultraviolet estimated to be over a hundred times as bright as it would later achieve at optical wavelengths. This spike was not observed for SN 1987A; by the time of the first UV observations, 33 hours after the estimated time of the shock breakout, the UV flux was declining rapidly, dropping by a factor of 1000 at 1400 Å in the following three days (Kirshner 1987). However, the UV flash is thought to be responsible for the ionization that was observed (beginning 3 months after the explosion) in a circumstellar shell around the supernova (Arnett *et al.* 1989a).
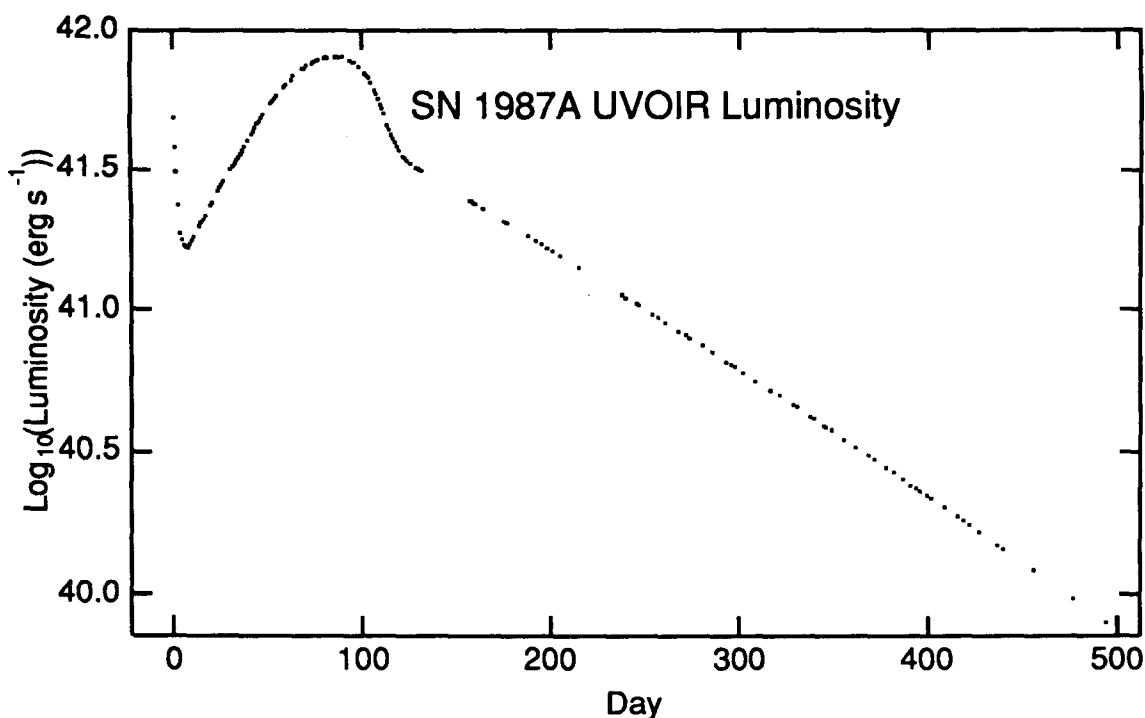
Figure 2.4 — SN 1987A luminosity at *Ultra*Violet, *Optical*, and *Infra*Red energies

(UVOIR luminosity) during its first 500 days. The first two data points are 27

and 36 hours after the neutrino burst, so these observations do not show the

initial UV spike. The luminosity is derived from measurements made at

wavelengths between 200 nm (U-band near-ultraviolet) and 5 μm (M-band

infrared) at Cerro Tololo Inter-American Observatory (CTIO) and European

Southern Observatory (ESO) (Suntzeff & Bouchet 1990). Measurements made

at other observatories, such as the South African Astronomical Observatory

SAAO (*e.g.*, Menzies *et al.* 1987; Catchpole *et al.* 1987, 1988, 1989; Whitelock *et*

al. 1988, 1989) give similar results during this time period.

The optical luminosity of the supernova grows over the next few hours as the shock wave blows the star apart, expanding the radiating surface by orders of magnitude. By the time the optical luminosity reaches a maximum, a day or so after the explosion, the total luminosity of the supernova is well into a decline as the edge of the ejecta cools. The total luminosity declines for a week as the cooling continues.

The expansion of the star continues to increase the radiating area while the surface of ejecta cools. After the first week the outermost part of the ejecta has cooled to a Sun-hot 6000 K. At this temperature the atoms in the ejecta recombine—the electrons bind to the nuclei to become a gas rather than a plasma—and the envelope becomes transparent to radiation from material below the surface.

As this deeper material, which had not previously had a chance to radiatively cool, releases its heat, its temperature also drops to the recombination temperature, and a wave of recombination propagates away from the surface. This recombination front forms the photosphere of the supernova, and is the location from which most of the luminosity is emitted.

The photosphere initially moves inwards into the ejecta more slowly than the ejecta moves outwards, so the photosphere is carried outwards with the expansion of the envelope. This increases its radiating surface area, while the temperature stays at the recombination temperature, so the flux starts to increase again. From day 10 to day 80, the effective radius of the photosphere (as approximated by a blackbody) increases by a factor of 2.6 (Catchpole et al. 1987), while the ejecta itself expands by a factor of 8. During this time, the effective

temperature stays approximately constant, between 6050 K and 5340 K (corresponding to a 40% variation in the radiation per unit area, $\propto T^4$).

The expansion adiabatically cools the ejecta, but the ^{56}Ni produced near the core decays with a 6.1 day half-life (Junde *et al.* 1987), pumping heat back into the envelope. This heat sustains the supernova luminosity, giving it a peak luminosity 80 days after the explosion that is higher than at any time after the first day. Without this radioactive heating, SN 1987A's luminosity would have reached its second peak after 40 days, at less than half the luminosity observed at day 80, and then abruptly dropped (Woosley 1988).

Gradually, the recombination wave reaches material that has expanded to lower densities (which increases the propagation speed) and is more slowly moving. Eventually it is moving faster than the outflow, and achieves a net inward velocity. The recombination wave starts to shrink, reducing its radiating surface, and the luminosity starts to decline again.

A month or so into the decline, around day 125, recombination is complete, and the light curve flattens out into an exponential tail with a time constant of 110^{+5}_{-10} days (*e.g.*, Catchpole *et al.* 1988; Suntzeff & Bouchet 1990). As the γ-ray measurements would demonstrate, the ejecta from SN 1987A contains large amounts of ^{56}Co, which has an exponential decay time constant of 111.26 days ($t_{1/2}$=77.12 days from the *Nuclear Data Sheets*, (Junde *et al.* 1987)). The conclusion drawn from this part of the light curve is that, during the exponential tail, the supernova is powered by the decay of this radioisotope. For SN 1987A, an initial production of ~0.07 M$_\odot$ of ^{56}Ni in the initial explosion, decaying to ^{56}Co with an 8.8 day time constant ($t_{1/2}$=6.10 days (Junde *et al.* 1987)) and then to ^{56}Fe, produces power equal to the UVOIR luminosity of SN 1987A for days ~145-265.

Measurements of earlier supernovae were based mainly on photographic magnitudes (equivalent to electronic measurements made using a blue B-band filter). For the case of SN 1987A, this is not a good approximation to the full UVOIR luminosity, due to the color changes as the supernova cools. The decay time constant of SN 1987A in the B band is 154 days during this time (Catchpole *et al.* 1988), which can be compared with values of 64, 145, and 90 days (with large uncertainties) for the exponential decay phases of Type I, IIP and IIL supernovae, respectively (Doggett & Branch 1985). This suggests that the luminosity of other supernovae might also display the same ~110 day decay time if measured over the UVOIR spectrum, rather than in B.

After 260 days the UVOIR luminosity of SN 1987A starts to drop below the level predicted by an exponential extrapolation using the decay time of ^{56}Co. The total luminosity continues along the exponential track, but some of the energy escapes in the form of γ-rays. With a correction for the γ-ray luminosity, the UVOIR luminosity due to ^{56}Co can be predicted. This correction is based on γ-ray measurements, such as those in this thesis.

If the UVOIR luminosity is greater than predicted, this could indicate the presence of an additional source of energy. This additional source may be radiation from a longer-lived isotope, such as ^{57}Co (391 day time constant), or it may be power produced by a compact central object, such as a pulsar or an accreting neutron star or black hole.

The extent to which such additional luminosity has been detected is unclear. Measurements of the UVOIR luminosity of SN 1987A by different groups can differ by more than a factor of 2 after day 1000 (Suntzeff *et al.* 1991). As SN 1987A cools (to a temperature below 200 K at day 900, Bouchet *et al.* 1991),

its spectrum shifts deeper and deeper into the infrared and the fraction of the flux that can be measured by the available instruments decreases. In addition, the flux from sources outside of the supernova must be eliminated or compensated for. These sources include other stars along the line of sight to SN 1987A, and energy from the earlier, brighter stages of SN 1987A reflected or re-radiated by dust and gas within a few light years of the supernova.

Finally, the fact that the spectrum of SN 1987A is non-thermal complicates the measurement of total luminosity. The luminosity measurements in the "I" band (infrared, ~8000Å) obtained by two major observatories (SAAO and CTIO) were discrepant by approximately 0.4 magnitudes (~40%) due to significant Calcium line flux included or excluded by the slightly different passbands of the filters used by those observatories (Hamuy $et\ al.$ 1990).

2.3   Gamma-Ray Processes in the Ejecta Of SN 1987A

Radioisotopes, especially those in the $^{56}Ni \rightarrow ^{56}Co \rightarrow ^{56}Fe$ chain, are the dominant energy source for most of the emission from SN 1987A between day 50 and at least day 1000 (Suntzeff $et\ al.$ 1992).

When an atom of ^{56}Co decays to ^{56}Fe, it produces an average of 2.9 γ-rays with an average total energy of 3.64 MeV. The γ-rays are produced at specific line energies, which are listed with their relative strengths in Table 2.1, and are associated with the transitions shown in Figure 2.5. The 511 keV γ-rays come from the direct or singlet positronium annihilation of positrons produced by the β^+-decay mode of ^{56}Co, which has a branching ratio of 19%. These positrons are ejected from the nucleus with an average energy of 600 keV, or 120 keV/decay. Additional energy (0.8 MeV/decay, on average) is released as neutrinos, and has no effect on the ejecta.

Energy: E_i (keV)	Branching Ratio: b_i (% of decays)	Notes
511	38.0	Assuming that all positrons decay in 2-γ mode
847	99.9	Strongest line
977	1.4	
997	1.4	
1038	14.1	
1175	2.3	
1238	68.4	Second strongest line
1360	4.3	
1771	15.5	
2015	3.2	
2035	8.1	
2598	17.4	
3202	3.0	
3253	7.6	
3273	1.8	
2253	6.0	Average energy, Σb_i for weaker (< 1%) lines
1245	292.5	Total energy: 3640 keV/decay in 2.93 γ-rays (Plus an additional 120 keV/decay in positron kinetic energy (19% of decays))

Table 2.1 — γ-ray lines from ^{56}Co decay, listing all lines with intensity greater than 1 γ-ray/100 decays. Data from *Nuclear Data Sheets* (Junde *et al.* 1987).

Some of these γ-rays, preferentially those emitted within a few mean free paths (MFPs) of the surface of the ejecta, escape directly from the ejecta without losing any energy and form a γ-ray line spectrum. If they are emitted from deeper in the ejecta, the γ-rays are more likely to Compton scatter, depositing some of their energy in the surrounding material before escaping, thus producing a continuum distribution. The γ-rays from deep inside the material are likely to scatter until they lose enough energy to be photoelectrically absorbed, depositing all of their energy in the ejecta.

The fraction of γ-rays that emerge, and how much energy they lose,
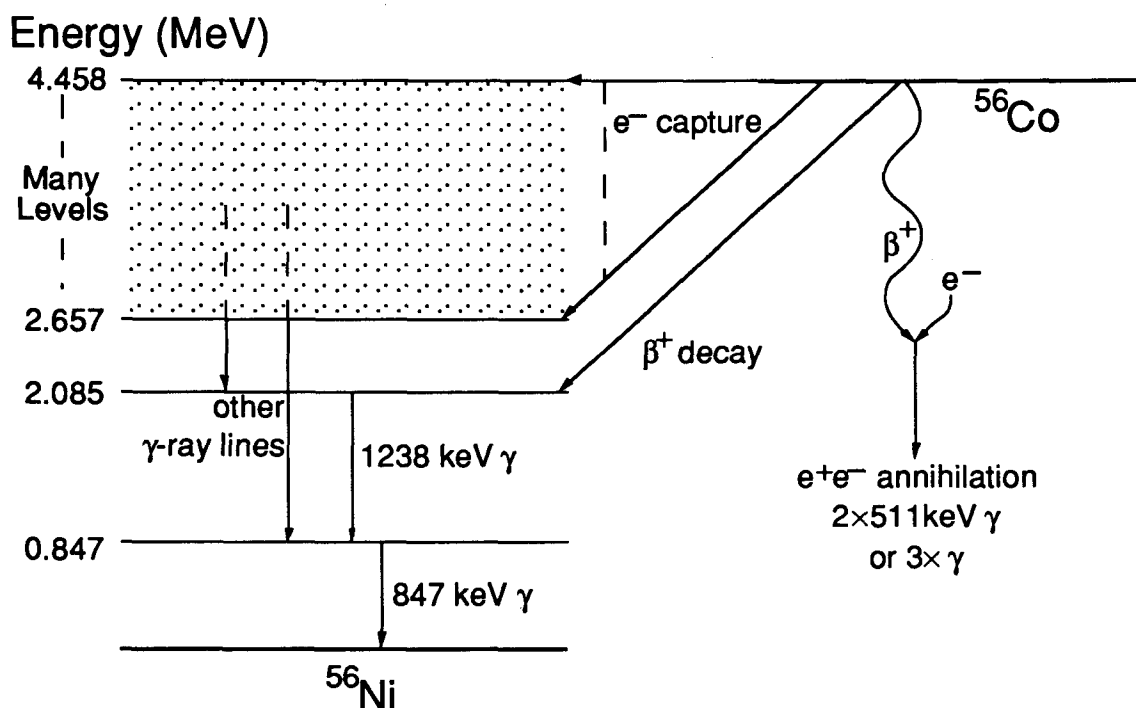
Figure 2.5 — Simplified level diagram for the decay of ^{56}Co → ^{56}Fe showing the most important γ-ray emission lines.

provides a measure of the depth at which the radioisotopes are buried and the characteristics of the intervening material. The energy loss may be determined by either measuring the γ-ray spectrum, or by measuring how much energy is re-radiated in the UVOIR bands.

The fraction of the ejecta that is probed by measurements of the emerging γ-rays, the top few γ-ray MFPs of the ejecta, increases with time as the ejecta spreads out and becomes more diffuse, and so the evolution of the γ-ray flux with time provides information on the location of the radiating material. This method of studying supernova envelopes was suggested by Donald Clayton (1974), who pointed out that the different MFPs for different line energies from the decay of ^{56}Co and ^{57}Co would allow the depth of a mixture of these isotopes to be derived from the strengths of these lines. Clayton calculated by a "simplistic analysis" that γ-ray line flux would not emerge from a supernova until two years had passed, but suggested that more physical models would predict the earlier emergence of flux. These more physical models would include the effects of hydrodynamic instabilities which could propel the centrally-produced radioisotopes to more exposed regions of the ejecta. He suggested that, due to the wide range of supernova behaviors, specific flux predictions for the next local supernova would have to wait until the supernova was observed.

In contrast to line measurements, the utility of measurements of the Compton-scattered continuum generally went unnoticed before SN 1987A. One paper even mentions that the continuum could be a nuisance, due to its contamination of line measurements (Woosley, Axelrod & Weaver 1981). However, the continuum measurements have been found to be as useful as the line measurements for our understanding of SN 1987A. The continuum γ-rays tend to come from deeper in the ejecta, since they scatter one or more times

before emerging, and thus probe a larger fraction of the ejecta. In theory, the distribution of radioisotopes down to a depth of many MFPs in the ejecta could be derived from a single sufficiently precise measurement of the continuum.

2.3.1   Interactions

γ-rays interact with the matter in the envelope of a supernova in three ways: Compton scattering, pair production, and photoelectric absorption. The interaction cross-sections for each of these processes depend on the energy of the γ-ray and the elemental composition of the ejecta. The transmission probability that a photon passes through a quantity x of material, measured in terms of column density (e.g., in units of g cm^{-2}), without interacting, is an exponential function given by:

$$T(E, x) = e^{-x/\lambda(E)}$$

where λ is the MFP (expressed as a column density) and may be written as a reciprocal sum:

$$\frac{1}{\lambda(E)} = \frac{1}{\lambda_c(E)} + \frac{1}{\lambda_{pp}(E)} + \frac{1}{\lambda_{pe}(E)} ,$$

where λ_c, λ_{pp}, and λ_{pe} are the partial MFPs corresponding to Compton scattering, pair production, and photoelectric absorption, respectively.

For photons at the two strongest line energies, 847 and 1238 keV, Compton scattering dominates. There is no pair production at energies below $2m_e = 1022$ keV, and the cross section does not approach that of Compton scattering below 100 MeV for the mix of elements composing the ejecta. Photoelectric absorption starts to dominate at energies below ~20 keV.

The first few interactions of the dominant line photons with the ejecta are usually Compton scatters. The photon will normally not be absorbed

photoelectrically until its energy is reduced to a few tens of keV. The typical range of a photon in the ejecta, therefore, is greater than its mean free path. The continuum photons, on average, come from deeper in the ejecta than the line photons.

2.3.2 Photon Number Balance

When a photon interacts in the ejecta by photoelectric, Compton, or pair production processes, the interaction decreases, leaves unchanged, or increases the number of photons, respectively:

1) A photoelectric interaction produces a free electron and an ionized atom. The ionized atom may release a fluorescence photon, but this may be ignored in our analysis—it is unlikely to escape the ejecta, and its energy is below the energy cutoff for the GRIP data analysis presented here. A photoelectric absorption, therefore, removes the photon from our dataset.

2) A Compton scattering transfers energy from a γ-ray to an electron, conserving the number of each type of particle.

3) A pair production interaction converts a photon into a positron and an electron. The positron interacts with the electrons in the ejecta to produce two or possibly three photons. However, pair production is relatively rare in the supernova ejecta, as it requires a photon with an energy well above the production threshold to interact with a heavy nucleus. For the line spectrum of ^{56}Co, fewer than 1% of the photons will interact by pair-production. For this discussion, I will ignore this process.

The number of γ-rays emitted by the supernova, therefore, is approximately the number of γ-rays produced by decaying ^{56}Co, minus the number which Compton scatter down to low energies and are then photoelectrically absorbed.

2.3.3   Energy Balance

The energy lost by the ^{56}Co γ-rays through Compton scattering and photoelectric absorption heats up the ejecta. This heat is then re-radiated, primarily as UVOIR flux shown in the exponential tail region of Figure 2.4.

Additional energy is deposited in the ejecta in the form of the kinetic energy of positrons produced in β-decay (19% branching ratio) of the ^{56}Co. The interaction of the positrons with the ejecta is complicated and beyond the scope of this thesis, but I will assume that all positrons deposit their kinetic energy in the ejecta and annihilate with electrons to produce γ-rays. I make this assumption because the positrons have a much shorter range than the γ-rays (~0.2 g cm^{-2} vs. 15 g cm^{-2} for 1 MeV γ-rays), and are therefore unlikely to escape at the times of our observations. The total positron kinetic energy is only 3% of the γ-ray energy. The decay of ^{56}Co also produces a neutrino, but that escapes the ejecta and its energy may be ignored.

The deviation of this region of the light-curve from an exponential decay with the ^{56}Co 111.26 day time constant is due to two sources: energy escaping from SN 1987A as γ-rays or positrons, or at other energies not measured by the UVOIR observations, and energy produced by sources other than ^{56}Co decay.

UVOIR telescopes, with focussing optics, much larger collecting areas, large numbers of photons, and almost-noiseless (by γ-ray standards) detectors,

can detect a much lower power flux than current γ-ray instruments. The UVOIR measurements can therefore continue long after the γ-ray flux has dropped below the sensitivity limits of current instruments at higher energies. The γ-ray flux at late times is estimated by creating models based on γ-ray measurements at earlier times, and using those models to predict the later escape probabilities.

2.3.4   Photon and Energy Production

If the ejecta of SN 1987A did not interact with the γ-rays from ^{56}Co decay, so that all could escape without losing energy, the total flux at Earth, $f_0(E, t)$, for each line i of energy E_i at time t ($t > 30$ days to allow the ^{56}Ni to decay to ^{56}Co), would be:

$$f_0(E_i, t) = b_i \frac{N_0}{4\pi r^2 \tau} e^{-t/\tau},$$

and the total number flux n_0 and energy flux p_0 due to the decay would be:

$$n_0(t) = \sum_i f_0(E_i, t) b_i$$

$$p_0(t) = \sum_i f_0(E_i, t) b_i E_i$$

where b_i is the branching ratio for production of the line, given in Table 2.1 and τ = 111.26 days is the mean lifetime of a ^{56}Co nucleus. N_0 is the number of ^{56}Co nuclei extrapolated backwards to $t = 0$, and is approximately equal to the number of ^{56}Ni nuclei produced (times a correction factor of 1.086 to adjust for the ^{56}Ni → ^{56}Co portion of the radioactive-series decay (Evans 1955)). Fluxes from other sources (such as ^{57}Co) become significant around day 750.

The distance to SN 1987A, r, need not be known for this analysis. What is important is the quantity $N_0 / 4\pi r^2$, which may be determined independently by measuring the UVOIR flux during the exponential tail and assuming that this represents the total energy production due to ^{56}Co decay in the ejecta.

.

This has been done by several groups. The main source of uncertainty in these measurements is the amount of interstellar extinction between SN 1987A and Earth, which may be as much as 40% at visual wavelengths. Using different values for the extinction, Suntzeff & Bouchet (1990) calculate 0.071 $M_\odot$ of ^{56}Ni produced, while Catchpole et $al.$ (1988) get a value of 0.078 $M_\odot$, where both values are normalized to a distance modulus of 18.5 magnitudes (a distance of 50.1 kpc). Taking conservatively large ranges for both distance and extinction, Suntzeff & Bouchet find acceptable values for the mass of ^{56}Ni produced to be in the 0.055-0.090 $M_\odot$ range. Since then, observations with the Hubble Space Telescope have measured the distance to SN 1987A to be 51.2±3.1 kpc (Panagia et $al.$ 1991), which reduces the allowed range to 0.061-0.084 $M_\odot$.

Adopting values of 0.075 $M_\odot$ of ^{56}Ni at a distance of 50.0 kpc, we get numerical values for the "transparent ejecta" line, photon number, and power fluxes of:

$$f_0(E_i, t) = 0.606 b_i\, e^{-t/\tau}\, \mathrm{cm}^{-2}\, \mathrm{s}^{-1}\,, \qquad (2.3.4.a)$$

$$n_0(E_i, t) = 1.77\, e^{-t/\tau}\, \mathrm{cm}^{-2}\, \mathrm{s}^{-1}\,,$$

and

$$p_0(t) = 2.21\, e^{-t/\tau}\, \mathrm{MeV}\, \mathrm{cm}^{-2}\, \mathrm{s}^{-1}\,.$$

2.4 SN 1987A γ-ray Emission Models

The early escape of γ-rays from SN 1987A shows that "simplistic" models of the evolution of the explosion are insufficient. These models assume a spherically-symmetric expansion of the supernova ejecta, with the radial distribution of the synthesized elements maintained as it was created during the explosion.

Later models place some ^{56}Co at shallower optical depths than the early models, allowing it to become visible more quickly as the ejecta dispersed. The physical mechanisms producing this redistribution require asymmetry in the ejecta, which is probably driven by Rayleigh-Taylor instability near the center of the explosion (Falk & Arnett 1973). This can extrude "fingers" of central material into the outlying regions of the ejecta, or propel the material as jets or "bullets." There may also be thin spots in the ejecta which reveal material near the center.

2.4.1   Fitting Line and Continuum Measurements to Models

The line spectrum of a model may be calculated from the fraction of the photons in each line that escape the ejecta without interacting. For the photons at line energies, the first interaction is usually a Compton scatter, and so the escape probability is a simple exponential of the integrated electron density between the ^{56}Co and the edge of the ejecta.

To calculate the continuum spectrum for a model, it is necessary to trace the paths of γ-rays through multiple scatters, which usually requires the use of Monte Carlo simulations.

For these reasons, line emission may be calculated analytically, but continuum emission predictions require Monte Carlo calculations. The simplicity of the line models, however, also means that line measurements are less sensitive to the composition and distribution of the ejecta. The continuum models, therefore, provide a better check of the theories of evolution of the envelope of the progenitor star.

2.4.2   Early Models

Early models of SN 1987A made certain simplifying assumptions. The ejecta was assumed to expand homologously and symmetrically—with no thin spots in the envelope and no "mixing" to disturb the stratification produced by nucleosynthesis in the progenitor star and the initial explosion.

Under these assumptions, it was predicted that significant γ-ray flux would not emerge until approximately a year after the explosion. It was appreciated at the time that these assumptions would, to some extent, be violated. However, there was not then, nor is there now, any way of accurately predicting *a priori* the extent to which the approximation is invalid.

Among these early models are those of: Bartunov *et al.* (1987), Chan & Lingenfelter (1988), Shibazaki & Ebisuzaki (1988), McCray *et al.* (1987), Woosley, Pinto & Ensman (1988), and Xu *et al.* (1988). Grebenev & Sunyaev (1987) produced Monte Carlo models with mixing and without spherical symmetry which indicated an earlier emission of γ-rays.

2.4.3   Post-Emergence Models

Early γ-ray detections, which showed line and continuum flux rising from below the sensitivity of all available instruments at early times to significant levels after approximately 5 months (Dotani *et al.* 1987; Sunyaev *et al.* 1987), triggered a second epoch of model production.

These later models include: Bussard, Burrows & The (1989), Chan & Lingenfelter (1988), Ebisuzaki & Shibazaki (1988a), Fu & Arnett (1989), Pinto & Woosley (1988), and Shigeyama & Nomoto (1990).

The complicated geometries produced in the explosion must be simplified to allow comparison to the limited data available, especially for models developed in response to just the earliest γ-ray detections. One commonly used simplification is to treat the ejecta as if it had spherical symmetry, and adjust the effective radial distribution of the ^{56}Co to match the data. Departures from spherical symmetry must be derived from other measurements (§2.5).

One of these spherically symmetric models, model 10HMM of Pinto & Woosley (1988) has become widely used for comparison to observations. This model is based on or consistent with the γ-ray data available by 1988 January, including the first two GRIP observations (an upper limit at day 85, and a measurement of both line and continuum flux at day 268). With these early observations, the radial distribution of the radioisotopes was underspecified, and the redistribution had to be done "in an arbitrary fashion."

2.4.4   Later Observations and Models

Measurements made by single instruments over long time periods provide homogeneous datasets that could be used to calculate more accurately the distribution of the radioisotopes in the ejecta.

Two such sets of measurements were made by instruments in space. (Meteorological considerations allow balloon instruments such as ours to observe only during two short periods each year.) One set of measurements was made using the HEXE instrument on the *Mir* space station, giving the continuum flux over an energy range of 15-200 keV. The other set of measurements was made with the GRS instrument on the *Solar Maximum Mission* (*SMM*) satellite, which measured the ^{56}Co line fluxes at 847, 1238, 2599, and 3250 keV.

These measurement sets were each used by the experimenters who produced them to calculate the radioisotope distribution. The resulting models were spherically symmetric.

2.4.4.1   The Sunyaev *et al.* Measurements and Model

The model of Sunyaev *et al.* (1990), which I will call S90, is based on the evolution of continuum measurements between 45 and 200 keV, as measured by the HEXE instrument in the Kvant module of the *Mir* space station.

These data were used in a Monte Carlo γ-ray transport model, using the predicted envelope given by Arnett (1988). The ^{56}Co was distributed in this model envelope to produce the best fit to the data, based on two different parameterizations. In one, the star was divided into 5 radial zones, in which the ^{56}Co fractions were independently varied. In the other, the radial distribution of the ^{56}Co was modelled by two Gaussians, with adjustable widths, positions, and heights. There is little difference in the resulting ^{56}Co distributions, as is shown in Figure 2.6. In both cases, the majority of the material is retained near the core while the remainder (~20%) is distributed in the outer 75% of the envelope.

2.4.4.2   The Leising and Share Measurements and Models

The models of Leising and Share (1990) are based on their measurements made using the GRS on *SMM*.

Figure 2.6 — Distributions of ^{56}Co as derived from measurements made by two space-borne instruments.

The solid curve is the ^{56}Co distribution derived from HEXE continuum measurements (Sunyaev *et al.* 1990), parameterized as the sum of two Gaussian distributions. This distribution is used in Model S90 to predict γ-ray fluxes. The crosses represent a fit to the same data using a different parameterization.

The rectangle is the ^{56}Co distribution parameterized as complete homogenization of the envelope within a certain cutoff radius, based on *SMM* line measurements (Leising & Share 1990). This distribution is the basis of Model LS3.

The parameterization of the LS3 ^{56}Co distribution does not allow it to be brought into closer agreement with the S90 distribution at shallow (high mass coordinate) depths. Variation of the parameters does not allow the local mass fraction of ^{56}Co to be greater than 0, but less than the average mass fraction ($\sim 5 \times 10^{-3}$).

This figure is taken from Sunyaev *et al.* (1990), with the LS3 distribution added.
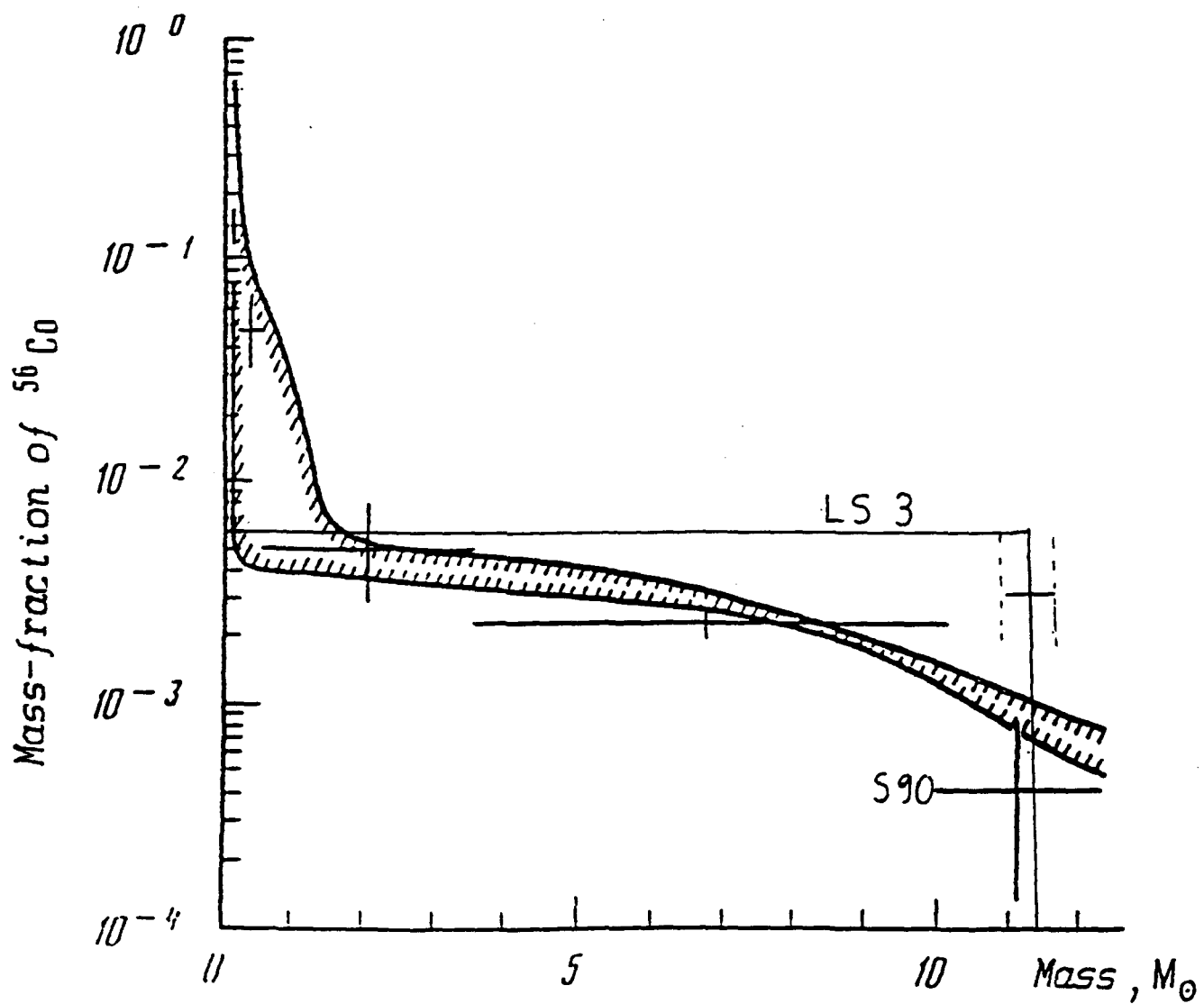
These observations required the instrument to measure something it was specifically designed to ignore—the γ-rays passing through a thick CsI active shield and hitting the main GRS detector. Although this mode of operation resulted in a low efficiency, the long observation times available from space allowed large amounts of data to be collected. The data were analyzed by the occultation method—determining the difference in count spectra between times when the supernova was hidden by or not hidden by Earth.

Despite the observational difficulties, the SMM data provides the most consistently sampled dataset for the evolution of line flux from SN 1987A, with a measurement for each 53 day period (set by the orbital precession period of the spacecraft) over a timespan of more than two years.

The line flux was fit to several different models. Model 1 assumed that all of the ^{56}Co was concentrated at a single optical depth. Model 2 placed fractions of the ^{56}Co at two optical depths. Model 3 evenly distributed the ^{56}Co between two optical depths. All of these models use the envelope model given in the Arnett *et al.* (1989a) review paper. I will call these models, LS1, LS2, and LS3.

The SMM data can rule out LS1, which results in either an earlier turn on or higher peak flux than is observed. The SMM data is consistent with both LS2 and LS3, and cannot distinguish between them. The SMM data does not contain enough information to require a more sophisticated model than LS2 or LS3. I will use the LS3 results for comparison to other experiments, but calculations using LS2 give similar results.

In the best fit to LS2, 5±1% of the ^{56}Co is in a layer of the ejecta that reaches unity optical depth (for 847 keV photons) at day 260±25, with the remainder not reaching unity depth until day 960±50.

In the best fit to LS3, the core material is homogenized with the envelope inside the layer that reaches unity optical depth on day 124±31, and outside the unity depth layer for day 1860±111. This distribution is shown on Figure 2.6 for comparison with the Sunyaev *et al.* models.

2.4.5   Comparison of Post-Emergence and Later Models

The 10HMM, S90, and LS3 models are summarized in Table 2.2. The models themselves are quite similar; all assuming a spherically-symmetric ejecta cloud and varying only in the distribution of radioisotopes in the ejecta.

Model Name (Reference)	Envelope Model	Source Data (observation time)	^{56}Co Radial Distribution
10HMM (Pinto & Woosley 1988)	Pinto & Woosley 1988	Early γ-ray measurements (1987)	"Arbitrary"
S90 (Sunyaev *et al.* 1990)	Arnett 1988	HEXE 45–200 keV continuum, (1987-1989)	2 Gaussians or 5 zones
LS3 (Leising & Share 1990)	Arnett *et al.* 1989	*SMM* line, (1987-1989)	Evenly through radial range

Table 2.2 — Models which are compared to the results in this thesis. All of these models are spherically symmetric, varying only in the radial distribution of the elements and isotopes.

2.5 Spherical Asymmetry

The spherical symmetry of the successful γ-ray models is not intended to prove that the ejecta itself is spherically symmetric—theory and observations indicate that it is not. It is believed that the mixing of the envelope is a result of Rayleigh-Taylor instabilities forcing "fingers" or clumps of material outwards through the overlying material to lower optical depths (Falk & Arnett 1973).

An understanding of asymmetry in the ejecta must be based on observations. Although computer modelling of the hydrodynamics of the early explosion (e.g., Arnett, Fryxell & Müller 1989b) does generate asymmetrical structure as a result of instabilities in the ejecta, accurate quantitative predictions of the final distribution of the central material is beyond the present state of the art, especially given our lack of knowledge of the progenitor star's initial conditions and the details of the explosion. The nebula surrounding SN 1987A, believed to be material ejected from the progenitor star SK -69 202 during its red supergiant and later phases, appears to be cylindrically symmetric (e.g., Luo & McCray 1991; Podsiadlowski, Fabian & Stevens 1991) which may be due to a companion or the rotation of the star. These would also induce spherical asymmetry in the ejecta.

Observational evidence for asymmetry in the ejecta exists:

1) The doppler-broadened profiles of atomic Fe lines in the infrared spectrum of SN 1987A show structure suggesting that fragments of iron-rich ejecta are travelling at speeds of up to 3000 km s^{-1}, significantly greater than the inner edge of the hydrogen envelope ($\sim$2100 km s^{-1}) (Spyromilio, Meikle & Allen 1990). Other IR spectra

further suggest that one "bullet," containing at least 3% of the total Fe produced, is moving with a line-of-sight velocity of ~3900 km s^{-1} in the direction away from us (Haas *et al.* 1990).

2) Polarimetry suggests asymmetry in the explosion (Jeffery 1987; Cropper *et al.* 1988).

3) High resolution γ-ray line spectra measured by the GRIS instrument on days 433 and 613 (Tueller *et al.* 1990), differ significantly from the spherically symmetric model predictions with respect to both line widths (2.9σ deviation) and line centroids (4.9σ deviation). In particular, these results may require a non-symmetric geometry for the expanding supernova remnant, containing both transparent and optically dense regions.

4) Kumagai *et al.* (1988) have found that a clumpy model sustains the X-ray flux for a longer time, in agreement with their measurements at 16-28 keV.

Nevertheless, the later spherically symmetric models are adequate to predict most of the behavior of SN 1987A, including all of our observations. In particular, the spherical models can be designed to produce good estimates of the total γ-ray luminosity as a function of time, which is the main contribution to the supernova luminosity outside of the UVOIR band. The spherically symmetric models, therefore, are useful for understanding the energy balance of the supernova.

Chapter 3
The GRIP Instrument

The Gamma Ray Imaging Payload (GRIP) is a balloon-borne γ-ray telescope developed, designed, and built by The California Institute of Technology (Althouse *et al.* 1985).

GRIP is sensitive over the energy range of 30 keV (limited by the attenuation of Earth's atmosphere at the altitudes obtained by scientific balloons) to 10 MeV (limited by the low flux of most sources at higher energies). Its angular resolution is as good as 0.6° over a 20° field of view (FOV) (depending on its configuration) and its spectral resolution is 16% FWHM at 100 keV and 6.5% at 1 MeV. Instrument characteristics are summarized in Table 3.1.

Many of the details of the instrument are given in Mark Finger's Ph.D. thesis (1987). The discussion here is concentrated on those points that are particularly relevant to the data analysis presented here, and those details that have changed since his thesis was written.

3.1   Coded Aperture Imaging

The technique used by GRIP to produce γ-ray images, above the energies where lenses, mirrors, and other traditional optical elements lose their effectiveness, is called coded-aperture imaging (Cook *et al.* 1984).

The basic elements of a coded-aperture imaging system are a mask and a position-sensitive photon detector. These are generally arranged parallel to each other and a distance apart, so that photons coming from a source in the field of view (FOV) must pass through the mask to reach the detector.

The GRIP Instrument	
Main Detector	41 cm diameter, 5.1 cm thick NaI(Tl)
Energy Range	30 keV-10 MeV
Imaging	Coded Aperture. 0.6° or 1.1° resolution, 20° or 14° field of view (see Table 3.2)
Mask-Detector Separation	2.5 m
Active Shielding	16 cm plastic (sides), 5 cm NaI (rear)
Pointing	Can point at elevations >25° above horizon, any azimuth relative to magnetic North
Operations	Autonomously follows observation plan, or can be commanded from ground
Maximum Data Rate	5300 events/s onboard recording (40 hrs) 1200 events/s redundant telemetry link
Operating Altitude	37 km (4 mbar pressure)
Balloon Size	6.5 - 8.0 $\times 10^5$ m^3 (23 - 28 $\times 10^6$ ft^3)
Weight	1400 kg (3100 lbs)

Table 3.1 — The GRIP instrument.

The mask is a pattern of opaque and transparent areas which either obstruct or allow the transmission of photons. A source in the FOV thus casts a shadow of the mask pattern onto the detector. The position of the source determines the position of the shadow pattern. Multiple sources in the field of view produce multiple superimposed shadow patterns, each shifted in the plane of the detector by an amount corresponding to the source's location on the sky.

This divides the detector into two different regions for any given point on the sky: the region that is exposed to that point in the sky, and the region that is not. The difference in incident flux between these two regions can be ascribed to flux coming from that point in the sky.

To recover the distribution of sources in the field of view, the shadow pattern is deconvolved with the mask pattern, yielding an image of the field of view. The mask pattern can be selected to optimize, by a chosen set of criteria, the image produced by this analysis. A description of the image reconstruction process is given in Appendix A.

For a given mask, the quality of the image produced by the reconstruction technique is determined by the accuracy with which the shadow pattern is measured. In the case of the GRIP instrument, the most significant restrictions on the measurement accuracy are imposed by the statistics of the photons measured by the detector and, to a lesser extent, the position resolution of the detector.

The photon statistics of measurements by the GRIP instrument are dominated by background events. In our observations of SN 1987A, for example, fewer than 1% of the γ-ray events used in the data analysis were actually from the supernova. The imaging system of a γ-ray telescope must therefore be designed to cancel background variation at the $\sim 10^{-3}$ level.

3.1.1   Hexagonal Uniformly Redundant Arrays

GRIP uses a rotating mask with a pattern called a hexagonal uniformly redundant array (HURA) to reduce the systematic variations in the counting rate to the level required. This class of patterns is described in more detail in Cook *et al.* (1984) and Finger (1987). HURAs have properties which make them suitable for coded-aperture imaging. The most important of these are uniform redundancy and rotational antisymmetry.

Uniform redundancy refers to the property that the auto-correlation function of the pattern is constant, except near the origin and the points of translational symmetry. This results in an image with uniform statistics across the field of view (Fenimore & Cannon 1978). It also allows the analysis technique called "back-projection," described in Cook *et al.* (1984), to be used as a computationally-efficient deconvolution method to recover a sky image from the modulation pattern on the detector.

Rotational antisymmetry allows the mask to be replaced by its antimask, which is the same mask pattern with opaque and transparent areas interchanged (except for the central cell of each pattern), by rotating it 60° about a point of symmetry. Analysis can be done by taking the difference in count rates for the mask and antimask orientations at each point on the detector, which eliminates effects due to position-dependent variations in background. The rotation can be done continually, many times during each observation, which cancels out slow variations in background and reduces the effects of fast variations that are not correlated with the mask position.
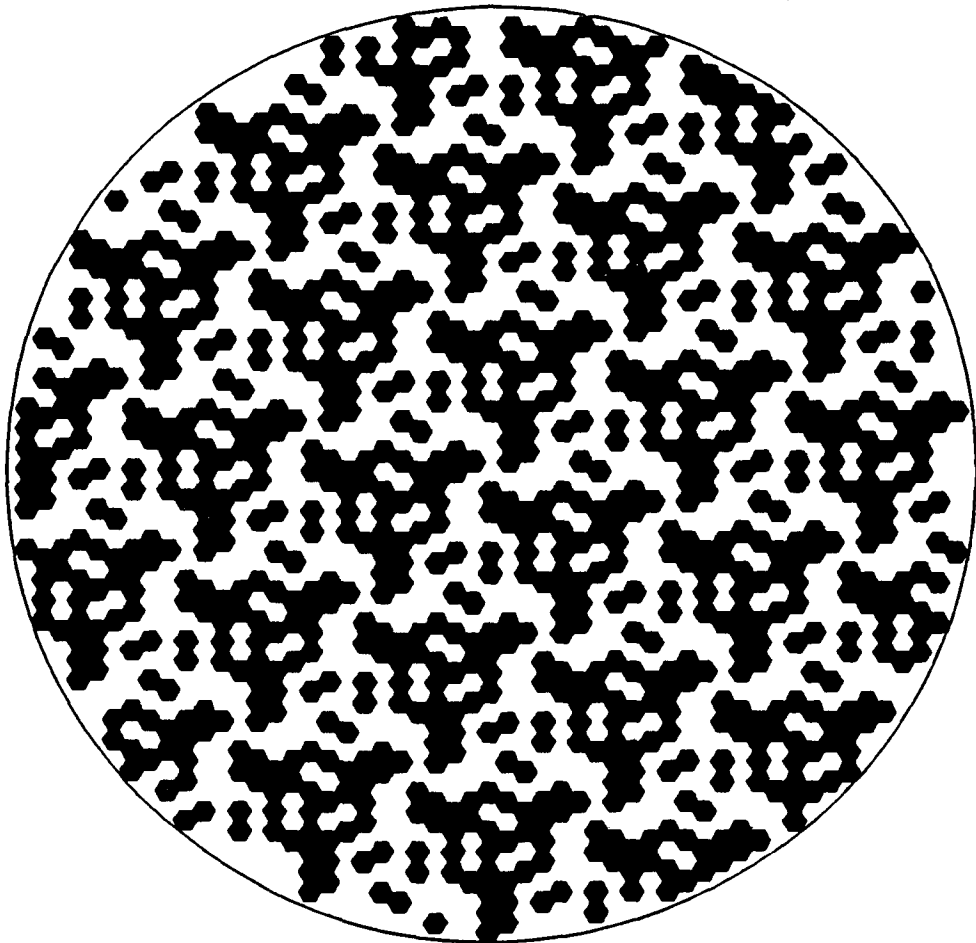
Figure 3.1a — Mask for configuration I

Figure 3.1a-b — The mask patterns used in the two GRIP configurations. The
black hexagons are the hexagonal lead blocks. The cells are 2.5 cm flat-flat
for the configuration I mask (Figure 3.1a), 4.8 cm flat-flat for the
configuration II mask (Figure 3.1b). The large circle, the rim of the mask
support structure, is 1.2 m in diameter in both cases.
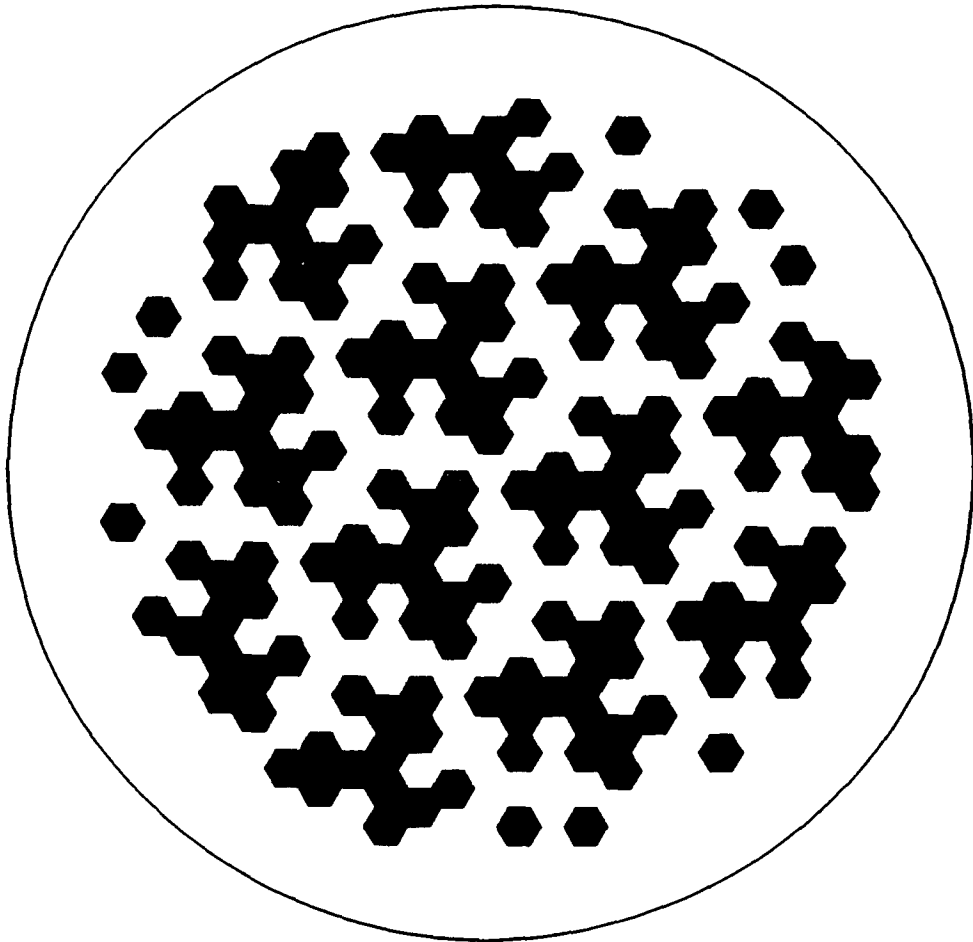
Figure 3.1b — Mask for configuration II

The two patterns used on GRIP, for different observations, are shown in Figure 3.1a-b. The HURA patterns consists of a unit pattern (of 79 and 31 cells for the two GRIP masks) repeated to tile the plane of the mask. The mask is continuously rotated about the telescope axis at approximately 1 revolution per minute. In addition to cancelling almost all background variation, the rotation also breaks the translational symmetry of the image caused by the repetition of the mask pattern.

3.2 Components

The conceptually important components of the GRIP imaging system are shown in Figure 3.2.

The position-sensitive NaI(Tl) camera plate, which is the main detector of the instrument, is geometrically shielded so that it is most sensitive to the γ-rays coming from the direction of the mask. The detector and its shield are described in more detail in §3.4. The detector and its shield, as well as its support electronics, are enclosed in a pressure vessel which is maintained at a pressure of one atmosphere and thermostatically controlled within a 5 C° range during each flight to reduce the effects of temperature changes on the detector and electronics.

The rotating mask, described in §3.5, is rigidly supported in front of the detector by a flared aluminum cylinder and rotated about its axis at approximately one revolution per minute by a small motor.

The imaging system and its support electronics are suspended from the balloon by a platform structure, as is shown in Figure 3.3, with motors, sensors,

and electronics which allow the telescope to carry out a sequence of observations either autonomously or under ground control. This pointing system is described in more detail in §3.6.

3.3 Configurations

GRIP has flown in two configurations. A summary of these configurations is shown in Table 3.2.

Configuration I is that described in Finger (1987), and was originally designed for observations of the Galactic center region. It was flown twice, once from Palestine, Texas (Althouse *et al.* 1987), and once from Alice Springs, Australia. Configuration II was developed for observations of SN 1987A, and has flown three times from Alice Springs.

	Configuration I	Configuration II
SN 1987A Observations	D86	D268, D414, D771
Angular Resolution	0.6°	1.1°
Field Of View	20°	14°
Cells In Unit Pattern	40 open, 39 closed	16 open, 15 closed
Cell Size (flat-flat)	2.5 cm	4.8 cm
Cell Thickness	1.9 cm	2.8 cm
Lead Opacity at 1 MeV	78%	88%
Mask Diameter	1.2 m	0.96 m
Lead Blocks in Mask	951	174
Collimator	None	14° FWHM

Table 3.2 — Major differences in the GRIP imaging system for the
two configurations.

Figure 3.2 — The GRIP imaging system. The detector and shield, with its

associated electronics, are contained in a pressure vessel. The mask is

suspended in front of the detector by a tapered aluminum cylinder.

Rotating Coded
Aperture Mask

2.5 METERS

Plastic Scintillator
Shield

Lead Hexcel
Collimator

41cm Diameter NaI
Camera Plate

Rear Shield and
Spare NaI Camera
Plate

Photomultiplier
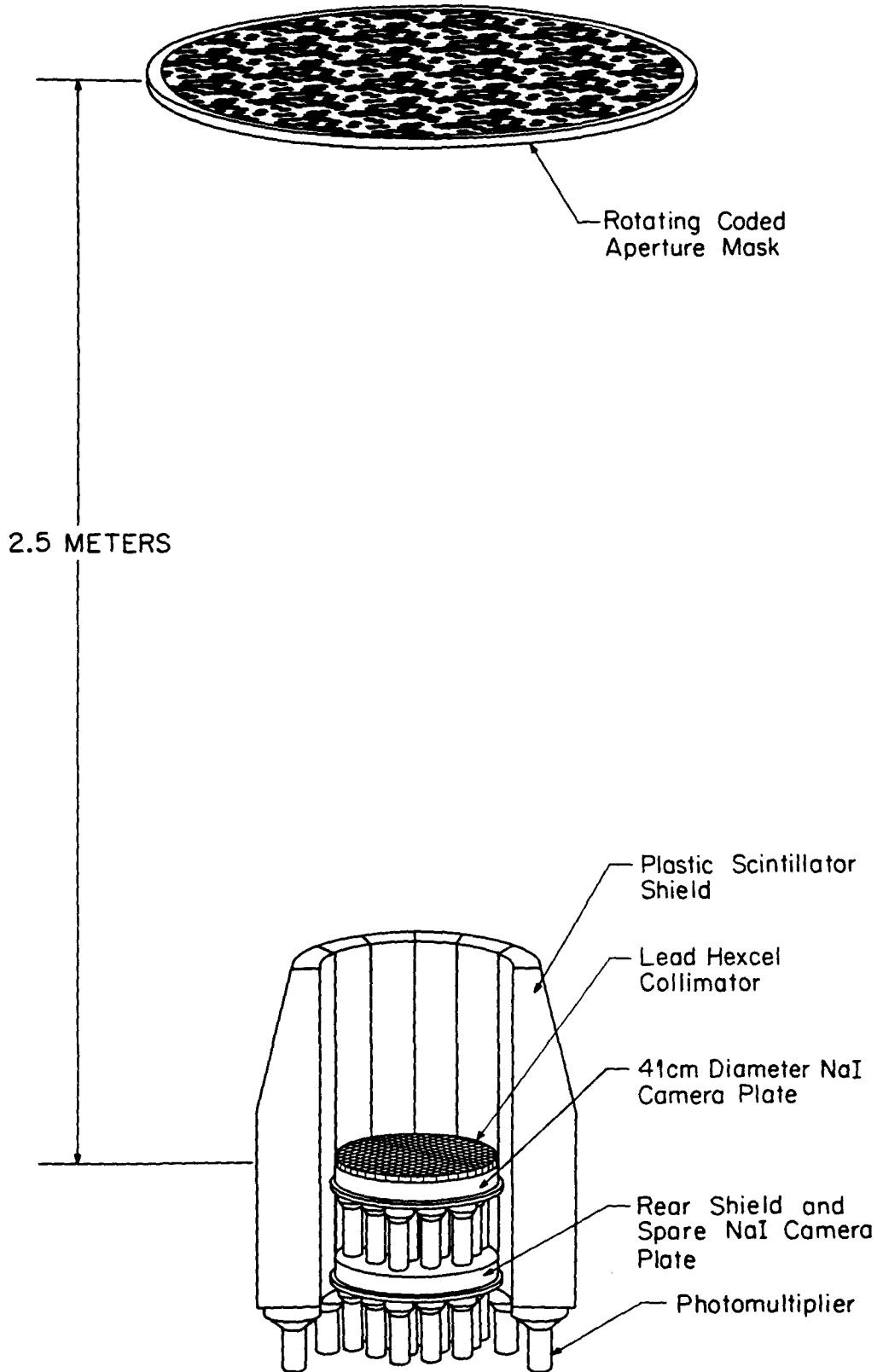
Figure 3.3 — The GRIP instrument and platform. The Sun and star camera
system, (shown by the dotted outline) was used only on the D414 and
D771 flights.

TO BALLOON

TORQUE MOTOR

SPREADER BAR

SUN/STAR
CAMERA

MAGNETOMETERS

MASK

MASK
TOWER

SHELL

BALL
SCREW

CRUSH
PAD

BALLAST
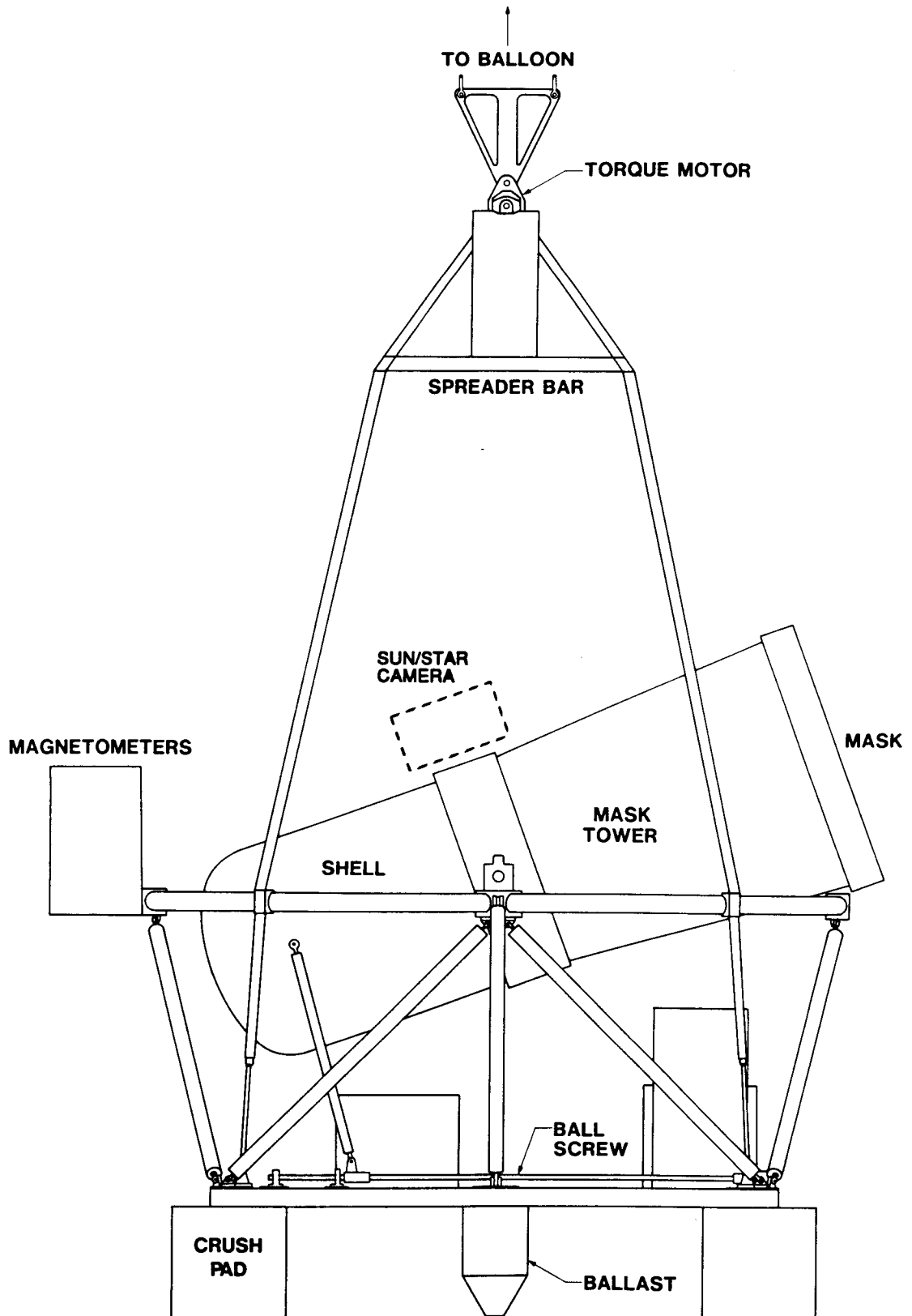
The primary difference between the configurations is the mask used. As described in §3.5.1, the configuration I mask was optimized to image with high angular resolution over a wide field of view containing many sources. The configuration II mask was optimized for sensitivity to a single source in a narrower field of view, with interesting spectral features at higher energies.

For configuration II, a lead honeycomb collimator was added to increase the sensitivity of the instrument at energies below 200 keV. As described in §3.4.3.1, this collimator preferentially blocks photons that approach the detector at an angle to the instrument axis. Although the collimator does absorb some γ-rays from sources within the field of view, the reduction in background more than compensates for this and increases the instrument's ability to detect and measure faint sources.

3.4　　The Detector

The camera plate that serves as GRIP's main detector is a 41 cm in diameter, 5 cm thick disk of Polyscin™ thallium-doped sodium iodide (NaI(Tl)), extruded by the Harshaw Chemical Company with a grain size of order 1 mm. The scintillation light produced by the interaction of γ-rays in the detector is collected by an array of nineteen 3-inch (7.5 cm) diameter Hamamatsu R1307 photomultiplier tubes (PMTs). For each detected event, the signal from each PMT is integrated over 1.5µs ($\approx$6 time constants of the scintillation light) and recorded with 12-bit precision (Cook, Finger & Prince 1985). The 19 PMT pulse-heights are analyzed as described in §3.4.2 to produce a measurement of the energy and position of the detected event.

3.4.1 Detector Calibration

The PMTs are continuously calibrated in flight by a system which electronically triggers the PMT integrating system 250 times a second. Light-emitting diodes (LEDs) inject light into the main detector in coincidence with every third trigger. The relative response of the PMTs to the LED light is used to obtain their relative gains. For the remaining two-thirds of these triggers, the LEDs are left off. This measures the PMT offsets—the PMT signal at times when no γ-rays are interacting in the detector. PMT gains are dependent (at the 5% level) on such things as the orientation of the PMTs in Earth's magnetic field and the temperature of the PMTs and electronics. The PMT offset signal is produced by dark current in the PMTs and by phosphorescent light in the detector, known as "afterglow," which is described in §3.4.4.1. These relative gain and offset measurements are used to adjust the PMT signals for each γ-ray event, resulting in a measurement of the light generated by the event and received by each PMT.

The absolute gain of the PMTs and the effect of temperature dependence of the light production of the NaI(Tl) are calibrated by measuring the response of the instrument to known γ-ray background lines.

3.4.2 Event Analysis Algorithms

The algorithm used to determine the photon position and energy from a set of 19 PMT signals was developed by Finger (1987) based on laboratory measurements of the GRIP camera plate. The position algorithm uses a maximum-likelihood analysis to derive a position based on the relative PMT signals. This produces both a two-dimensional position across the face of the camera plate, and a "depth-parameter" which corresponds to the distance of the event from the front of the scintillator. Edge effects in the detector currently limit

the validity of this algorithm to approximately the central 645 cm^2 of the camera plate, excluding a 6 cm wide annulus around the edge of the detector. This annulus falls on and outside the outer ring of PMTs, where the distribution of scintillation light is not as well sampled as it is for the central region. The results in this thesis are based on events from the central region only. Analysis efforts are currently underway to generate an algorithm for the peripheral region.

The light-collection efficiency, as a function of the derived position, is used to adjust the sum of all PMT signals to obtain the total light produced by the γ-ray in the scintillator. This is converted to a γ-ray energy using a function based at low energies ($\leq$450 keV) on the Luminosity/Energy curves from Birks (1953), and at higher energies on measurements of known lines in the background spectrum of our instrument.

3.4.3 Background Reduction

The term "background," as used here, refers to γ-ray events (or events that our detector does not distinguish from γ-rays) which are not produced by specific astrophysical point sources in the field of view. This includes radiation from weak sources in our field of view, the diffuse γ-ray background, γ-rays from sources outside of our field of view, secondary photons from cosmic ray interactions with the atmosphere and the instrument, and natural and induced radiation from the instrument and from the camera plate itself.

For γ-ray observations in our energy range, the background count rate typically exceeds the flux from specific astrophysical sources. In the case of our SN 1987A observations, the source/background ratio is less than 10^{-2} between 50 and 800 keV.

Figure 3.4 shows the background, measured by GRIP in its two different configurations, compared to the detector count rates that would be expected from specific astrophysical sources if there were no background. Even this level of background reflects a careful design which has background reduction as one of its primary goals.

3.4.3.1   Shielding

Background may be reduced by preventing unwanted γ-rays and other particles from interacting with the detector, or by discarding data from interactions in the detector associated with background events. Shielding serves both of these functions. The shielding for the GRIP detector is of three types: active shielding, passive shielding, and self-shielding.

The active shield, as shown in Figure 3.2, is a well of scintillating material which surrounds the main camera plate except in the direction of the nominal field of view of the instrument. The wall of the well is a 16 cm thick hollow cylinder consisting of 12 pieces of BC-408 plastic scintillator (chosen rather than NaI(Tl) for budgetary reasons), each viewed by an individual 5-inch (13 cm) Hamamatsu R1416 PMT. The bottom of the well is a NaI(Tl) scintillator, identical in dimensions and PMT layout to the camera plate.

Figure 3.4 — The background and signal spectra measured by GRIP. The configuration I background spectrum converges to within 10% of the configuration II background above 400 keV. The difference below that energy is due primarily to the collimator. The signal spectra are typical detector count rates (adjusted for atmospheric and instrumental attenuation, detector efficiency, and imaging efficiency) predicted for the Crab Nebula and Pulsar, and SN 1987A with the spectrum we measured 268 days after the explosion. The steps at 300 keV are due to details of the data analysis (see §3.4.3.1 on the self-shielding capabilities of the detector).
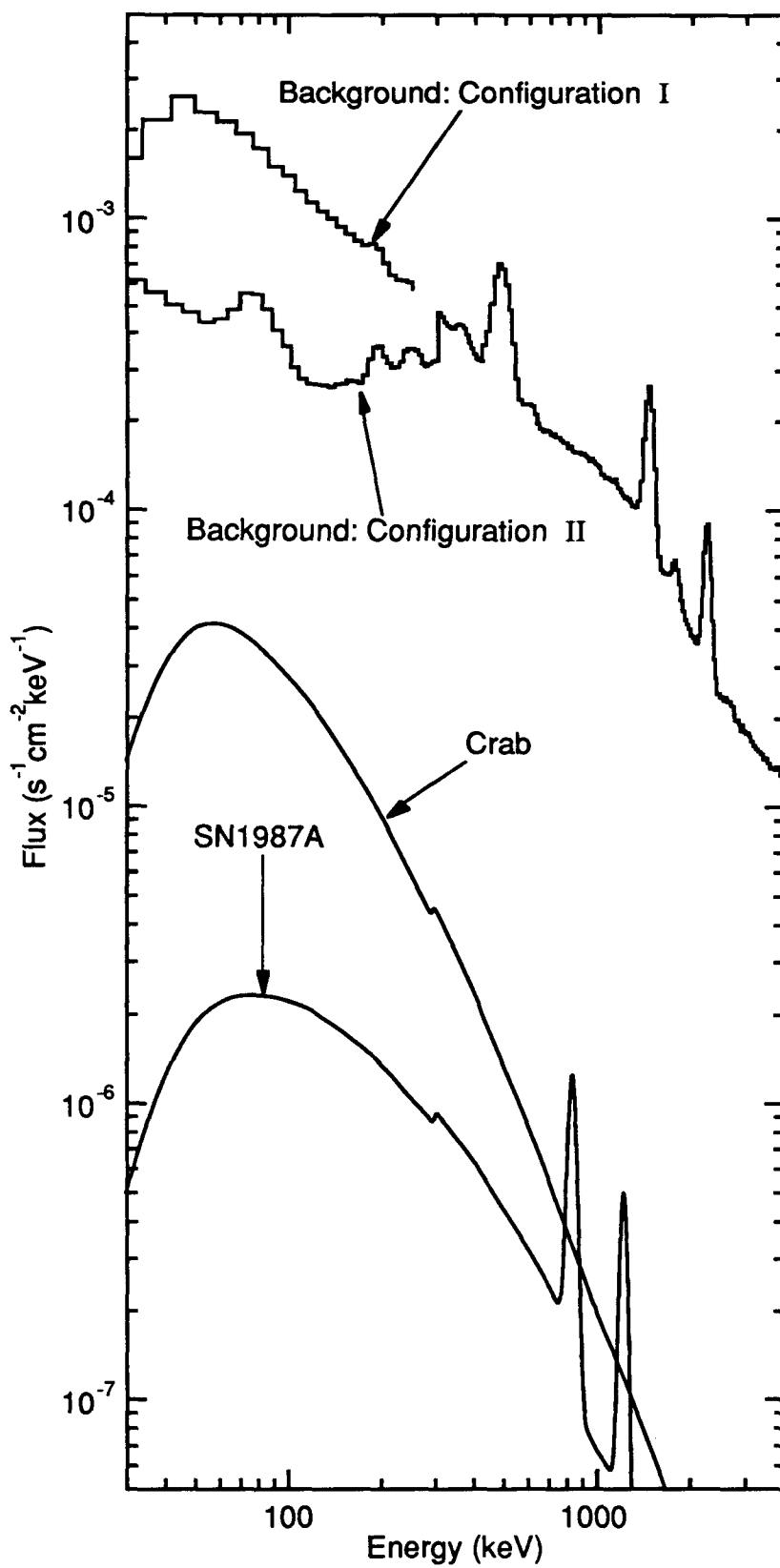
Events in the main detector are discarded, or "vetoed," if they occur in coincidence with scintillations in this active shield. The threshold for detecting shield events is 40 keV (for the rear NaI(Tl) shield) or 50 keV (for the plastic shield). This reduces the measured flux of γ-rays that enter the instrument from outside of the field of view. It also reduces "partial-energy" γ-rays, which scatter in the detector and then escape to interact with the shield, which would degrade the energy resolution of the detector (as is discussed in §3.4.4.2).

Charged cosmic ray particles, which have typical energies measured in GeV, tend to pass through both the detector and the shields without stopping, while depositing large amounts of energy (~100 MeV) in each. These are vetoed by the shields, and are redundantly vetoed by an upper-limit threshold on total light from the main NaI(Tl) detector.

The active shield can also reduce internal background due to natural and induced radioactivity in the detector and shield. As an example of induced radioactivity: ^{128}I is produced in the detector by neutron capture on ^{127}I and β-decays with a half-life of 25 minutes, producing a β particle and a 443 keV γ-ray. When a nucleus β-decays, the β particle is usually stopped very near the site of the decay (typically within a millimeter) while the γ-ray has a much longer range, and can escape to interact elsewhere. If the decay occurs in the detector, and the γ-ray reaches the shield (or vice-versa) that event is vetoed, and does not contribute to the background.

The shield also passively blocks γ-rays, absorbing them so that they cannot reach the detector. Additional passive shielding is provided by a 1.6 mm thick layer of tin which lines the inside walls between the plastic scintillators and the main detector. This high-Z material photoelectrically absorbs low-energy

photons that hit the inner wall of the well. Without the tin liner, the photons could Compton scatter from the low-Z plastic scintillator without depositing enough energy to trigger a shield veto. These scattered photons would be an unvetoed source of background.

Measurements made with the active shield disabled during GRIP's first flight, from Palestine, Texas in October 1986, indicate that the event rate for the detector passively shielded by the plastic, NaI(Tl), and tin shields is only ~30% of that predicted for an unshielded detector. This indicates that 70% of the γ-rays are absorbed by the shielding before they reach the main detector. When the shield veto was turned on, half of the remaining events were vetoed (Finger 1987).

Additional passive shielding is supplied in configuration II by the collimator. This accounts for the majority of the difference shown in Figure 3.4 for configurations I and II at low energies. The collimator is a honeycomb of lead which preferentially passes γ-rays travelling parallel to the telescope axis, while blocking those that enter at an angle. Its geometry (25 mm thick, with 6 mm (flat-flat) hexagonal cells, and 0.4 mm thick cell walls) provides a FWHM acceptance angle for low energies of 14°. Its transmission as a function of energy is shown for several energies in Figure 3.5, with a peak transmission of 87% for sources on the axis. This collimator significantly improves the instrument's sensitivity by reducing the background at low energies, as is seen by the difference between the configuration I and configuration II background curves in Figure 3.4.

A self-shielding capability is provided by our position algorithm by allowing us to veto low-energy events that occur in the rear of the main detector. At energies below 300 keV, fewer than 10% of the γ-rays incident on the front of the camera plate penetrate more than halfway (2.5 cm) into the detector. Events

at low energies are therefore excluded from the data analysis if the position algorithm places them in the rear half of the detector.

Self shielding produces a ~50% reduction in the background rate while rejecting only ~10% of the true source counts, yielding a significant improvement in the instrumental sensitivity at low energies. The background reduction at 300 keV can be seen by the step at 300 keV in the histograms of Figure 3.4, which show the spectrum of analyzed events (~99% of which are background). The false rejection rate was measured experimentally and stays in the 5-15% range over the 50-300 keV energy range over which self-shielding is used. At low energies, even though essentially all of the γ-rays interact near the front of the crystal, the decrease in position resolution resulting from the reduced photon statistics
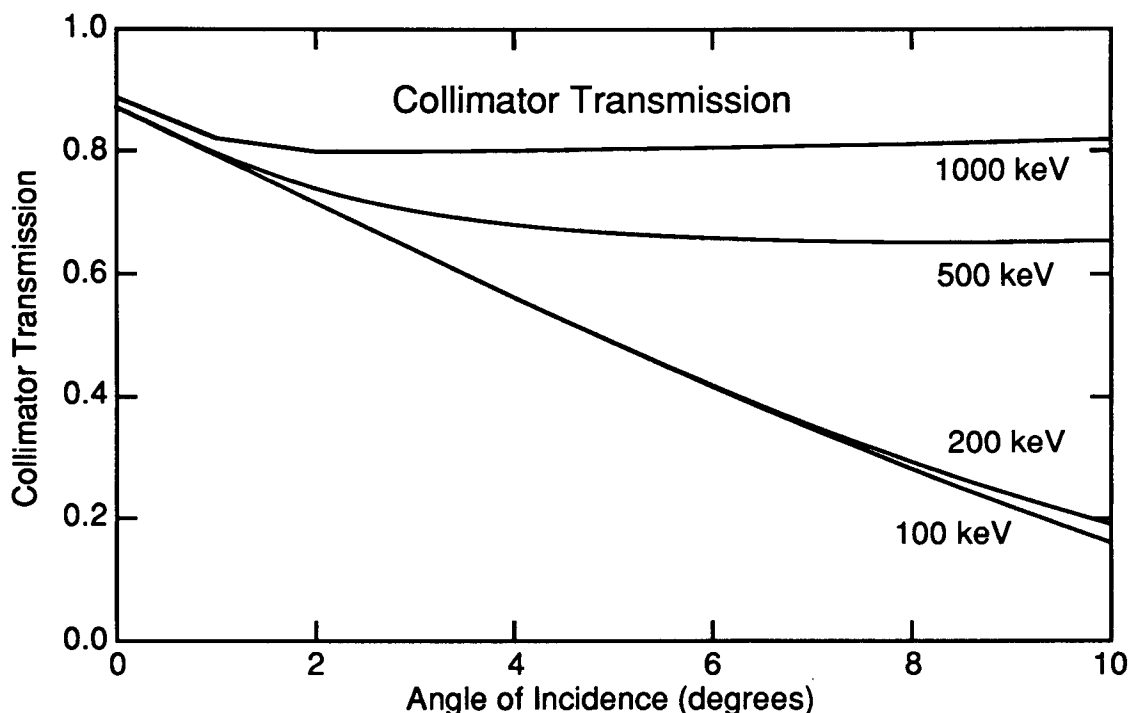
Figure 3.5 — Collimator transmission vs. angle for γ-rays at various energies.

brings the false rejection rate back up to the measured value.

3.4.4 Detector Position and Energy Resolution

The energy and position resolution of the main detector vary as a function of energy, and are shown in Figures 3.6 and 3.7. At low energies, the energy and position resolution are constrained primarily by the photon-statistics of the light production and collection, and by afterglow (§3.4.4.1). Figure 3.6 shows the measurement resolution of the energy deposited in the detector, which is not necessarily the same as the energy of the incident photons (see §3.4.4.2). At high energies ($\geq$500 keV) Compton scatter becomes important in determining the position resolution (§3.4.4.3).

3.4.4.1 Afterglow

When γ-rays and charged particles interact with a NaI(Tl) scintillator, most of the light is emitted as a short scintillation flash but some (an order of magnitude less than the scintillation light) is emitted much more slowly as phosphorescent emission. The decay time for this "afterglow" is 150 ms, orders of magnitude longer than the 230 ns primary scintillation light.
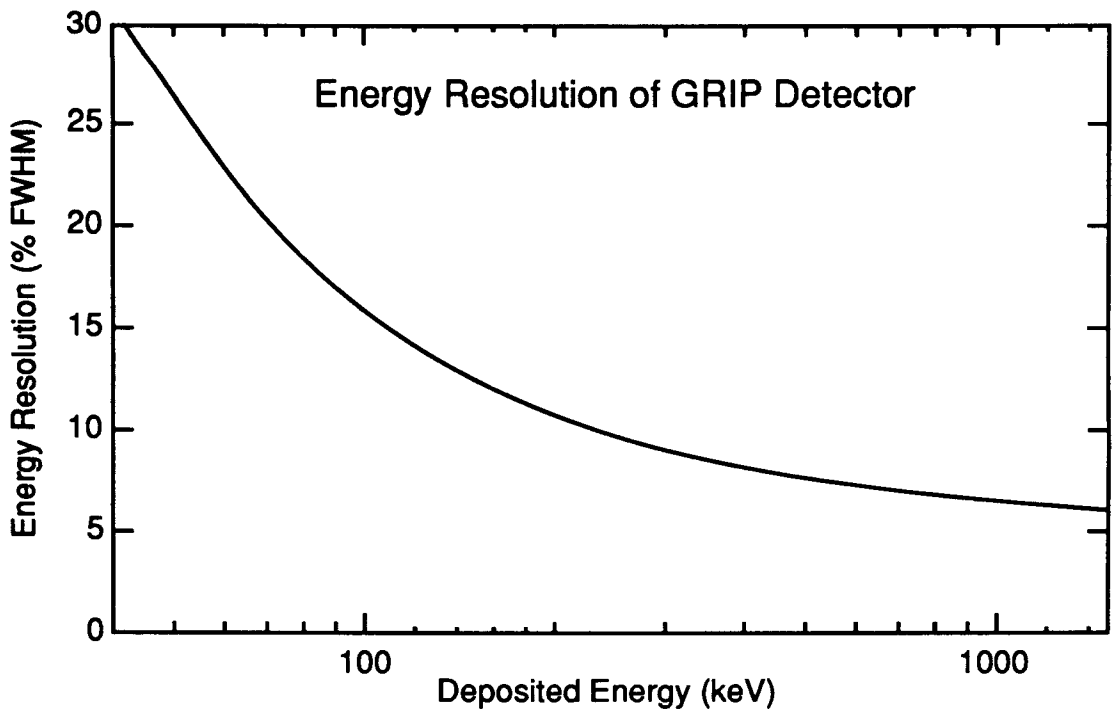
Figure 3.6 — Resolution (FWHM) of the measured energy distribution as a function

of the energy deposited in the central 645 cm² of the main NaI(Tl) detector.

Photons which have the same initial energy may deposit varying amounts of

energy in the detector (see §3.4.4.2 and Figure 3.8). This plot is based on

measurements of radioisotope γ-ray lines in the laboratory combined with

flight measurements of afterglow (see §3.4.4.1), and verified with

measurements of the widths of background lines during flight.
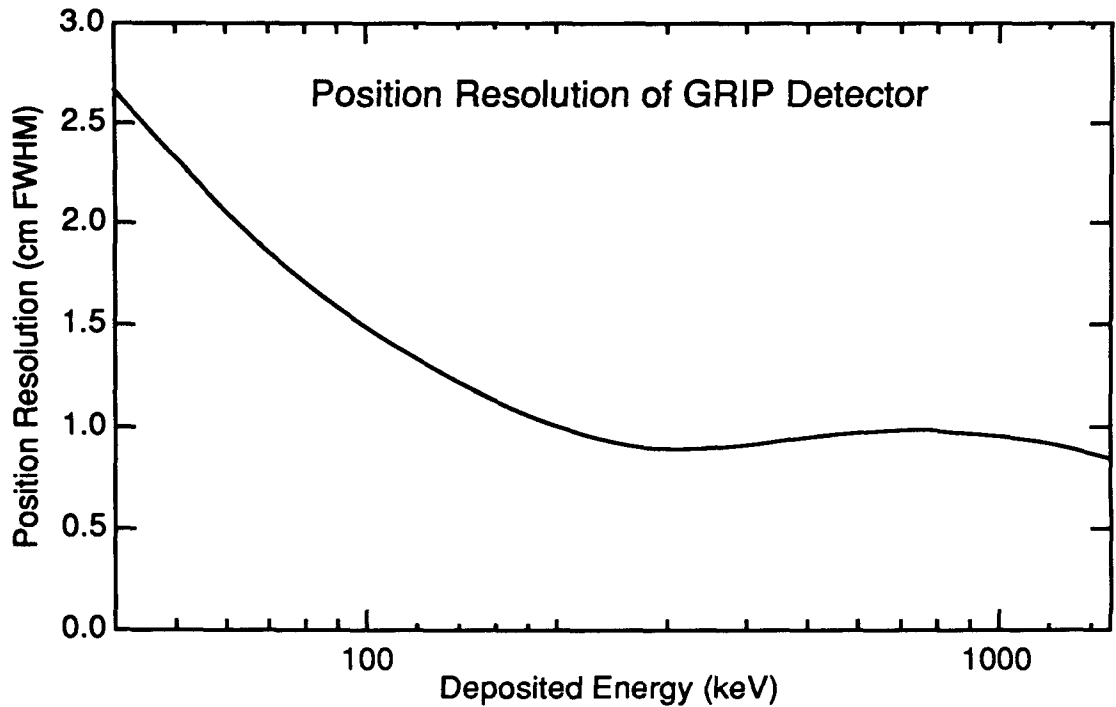
Figure 3.7 — Position resolution of the main GRIP detector. FWHM of the

1-dimensional position distribution for an interaction point in the central 645

cm^2 of the main detector. This plot is based on laboratory measurements, with

additional contributions determined from afterglow measurements (§3.4.4.1)

and Monte Carlo calculations of multiple-site interactions (§3.4.4.3).

Most of the afterglow light is produced by charged cosmic ray particles and their secondaries. Although these have a rate ($\sim$500 s^{-1} in our detector for Australian flights) an order of magnitude below the γ-ray rate, they deposit much more energy than the average γ-ray does. Protons, which make up the majority of the charged particles, deposit 70 MeV on average as they pass through the detector, while heavier elements (C - Si), with a rate of $\sim$1 s^{-1}, deposit $\sim Z^2 \approx 36$-200 times as much energy with each interaction. A few times per minute an iron nucleus passes through and deposits $\sim$50 GeV in the detector, $\sim 10^6$ times as much as the average γ-ray. Although the primary scintillation of a charged particle is ignored, due to charged particle's passage through the shield and due to its large energy deposition in the detector, the afterglow continues long after the shield veto is reset.

At any given time during an observation, the camera plate has a steady, even glow from the hundreds of γ-rays and protons that hit it in the previous few (150 ms) time constants, possibly a bright spot from a heavy element nucleus that passed through, and occasionally a very bright spot from an iron nucleus.

The afterglow interferes with the energy and position measurement of γ-ray events. The steady glow adds Poisson statistics to the light collected by the PMTs for actual events, and the localized bright flashes from heavy elements increase the measured energies and displace the measured event locations towards the location where the heavy nucleus passed.

The offset measurements described in §3.4.1 allow us to estimate these effects by measuring the signal on each PMT at times when there is no primary scintillation light. The effect on energy resolution is obtained from the distribution of the sum of all offset measurements. The effect on the position

resolution is studied by choosing a specific γ-ray event at some energy, and determining the distribution of calculated event positions when the PMT values are adjusted by the offset measurements.

In flight (for our SN 1987A observations at the geomagnetic latitude of Australia), the sum of all PMT offset measurements has a distribution with a FWHM of 9 keV, compared to 3 keV on the ground due to all other sources of noise. This spread is equivalent to the counting statistics of the scintillation photons due to a 100 keV γ-ray, and so below 100 keV the afterglow dominates the energy resolution of our detector.

Similarly, the afterglow dominates the position resolution of our detector below 25 keV, with less effect at higher energies. At 100 keV the loss of position resolution is minor; the component of the position resolution due to afterglow is 6.6 mm (FWHM), which adds in quadrature to the 13 mm from photon counting statistics of the primary scintillation to give 15 mm, a 15% effect.

3.4.4.2   Energy Escape

In the previous discussion, the term "energy resolution" was used to describe the approximately Gaussian distribution of the measured light corresponding to a given amount of energy deposited in the main detector.

When a γ-ray interacts with a detector, it sometimes deposits only a fraction of its energy in the main scintillator, and thus the distribution of measured energies for monoenergetic incident photons will not have this shape. There are several ways in which energy may escape from the detector, of which the two most important are fluorescent escape and Compton escape.

3.4.4.2.1 Fluorescent Escape

Energy from a γ-ray may escape from the main detector by fluorescence. In this process, a γ-ray is photoelectrically absorbed by an iodine atom in the NaI(Tl) detector. (The γ-ray cross section for I is ~10^3 times as large as the cross section for Na at these energies.) This photoelectric absorption removes an electron from the atom's K-shell (88% of the time), creating a vacancy which is filled by the fall of an electron from a higher shell. This transition creates a fluorescence X-ray with an energy of ~30 keV (28.3 keV (28%), 28.6 keV (53%), 32.3 keV (15%), or 33.0 keV (3%)) (Lederer & Shirley 1978). If this X-ray escapes the detector without depositing its energy, the energy measured by the detector will be ~30 keV below the original γ-ray energy. The energy spectrum of a monoenergetic γ-ray source as measured by a NaI(Tl) detector will therefore have a fluorescent escape peak 30 keV below the main peak.

The data analysis presented in this thesis ignores all events with measured energies less than 50 keV, a lower bound set by the low elevation (and correspondingly large atmospheric attenuation at low energies) of SN 1987A even at transit. Any event with an initial γ-ray energy below ~80 keV will thus be eliminated from data analysis if it results in a fluorescent escape. The probability of the escape of the fluorescence X-ray, as determined by a Monte Carlo analysis using GRIP's detector geometry, is greatly reduced at higher energies, dropping from 5.6% at 80 keV to 1.1% at 150 keV. (Higher energy γ-rays tend to penetrate deeply enough into the crystal before interacting that the low-energy fluorescence photon is unlikely to escape.) Fluorescent escape is, therefore, important in the analysis presented here only for its reduction in the instrument's low-energy detection efficiency, and not for the effect of the fluorescent escape peak on energy resolution.

3.4.4.2.2   Compton Escape

The second energy loss mechanism is Compton escape. If a γ-ray Compton scatters in the camera plate and then escapes the instrument without depositing any additional energy, it will be measured as a γ-ray of lower energy. However, as was discussed in §3.4.3.1, the GRIP detector is surrounded by thick anti-coincidence shields, shown in Figure 3.2, which veto any camera plate events that occur in coincidence with shield events. The Compton-scattered photon will trigger the veto unless it is absorbed by the passive shielding, passes through the thick active shield without depositing the threshold energy (40-50 keV), or scatters by ≥150° (for a γ-ray from within the field of view) and emerges through the open end of the shield.

Figure 3.8 shows the calculated distribution of measured energy for 1 MeV monoenergetic photons interacting in the central 645 cm^2 of the detector. The energy deposition in the main detector and the possible effects of Compton scattering and shield vetoes were calculated using a Monte Carlo model of the instrument. The resulting deposited-energy distribution was then convolved with the experimentally measured energy resolution. The main peak, the "photopeak," corresponds to incident γ-rays that deposit all or nearly all of their energy in the detector. The distribution below the photopeak is due to γ-rays that deposit only part of their energy, and then escape without triggering a veto. The secondary peak at the high end of the partial-energy distribution is due to γ-rays which Compton scatter at large angles, allowing them to be absorbed by the collimator or to escape through the open end of the shield. Not shown on this plot are the γ-rays that resulted in vetoes, or passed through the detector without interacting.

Figure 3.8 — The calculated distribution of measured-energies for

monoenergetic 1 Mev γ-rays incident on the central 645 cm^2 of the main

detector. The distribution of deposited energy and the effect of vetoes due

to shield interactions were calculated using a Monte Carlo model of the

instrument. The deposited energy distribution was then convolved with

the experimentally-determined energy resolution (Figure 3.6). The main

"photopeak" at the γ-ray energy is due to γ-rays which deposit their entire

energy in the detector. The continuum below the main peak is due to

partial energy deposition. The bump around 750 keV is due to the energy

deposition of events which Compton scatter at large angles ($\geq 150^\circ$) and

either are absorbed by the collimator, or pass through the opening at the

front of the shield.

Detector Spectrum
for 1 MeV γ-rays
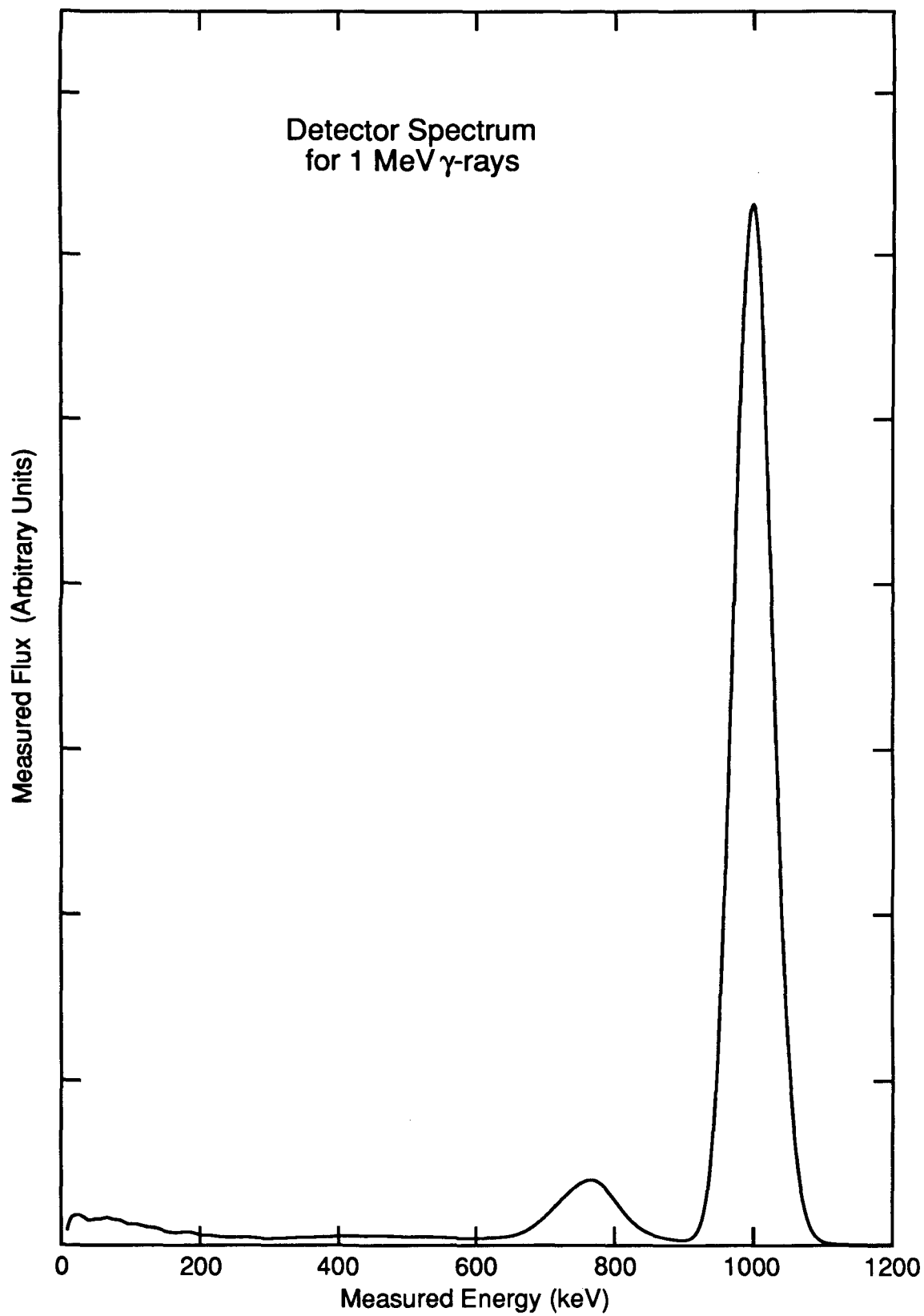
The fraction of events in the photopeak, the "photopeak efficiency," and in the partial-energy distribution, the "partial-energy efficiency", is shown as a function of energy in Figure 3.9.

The partial-energy events affect the effective sensitivity of the instrument in a way that is dependent on the spectrum of the source, as will be discussed in §3.4.5.
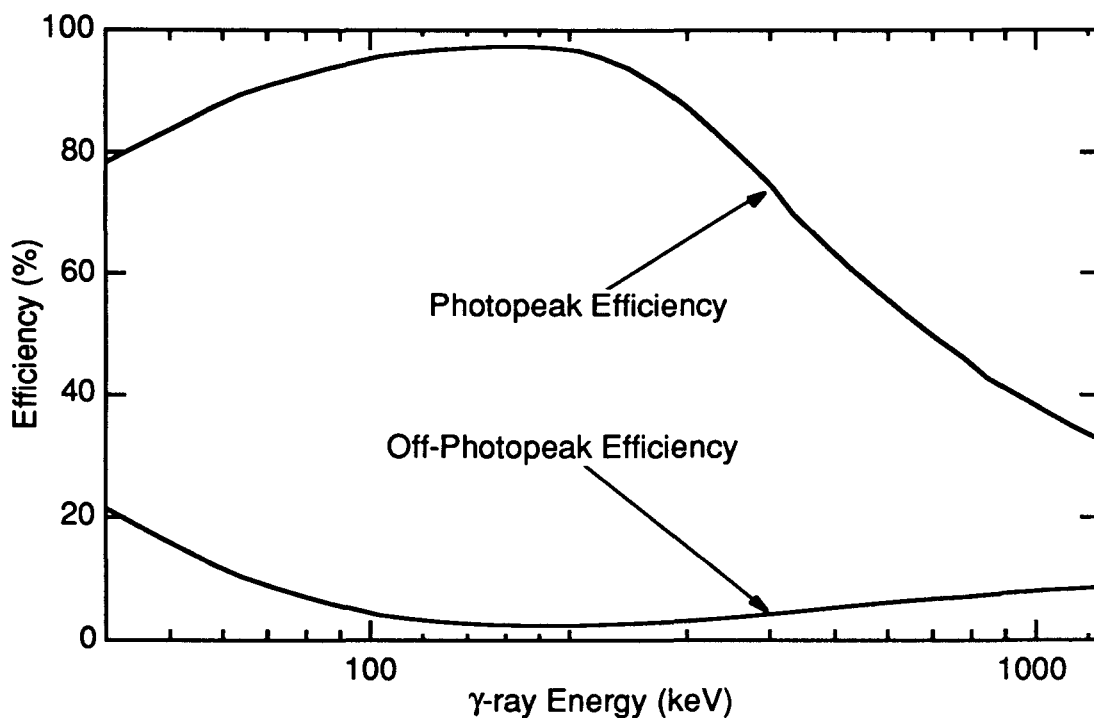
Figure 3.9 — Fraction of incident γ-rays which are detected by the main detector either with their full energy (photopeak) or partial energy (off-photopeak). The difference between the sum of these efficiencies and unity represents the γ-rays which either do not interact with the detector, or trigger a veto by depositing some of their energy in the shield. These curves are based on Monte Carlo models of γ-ray propagation in the instrument.

3.4.4.3   Multiple-Site Interactions

When a γ-ray Compton scatters in the detector, the scattered photon can travel a distance away from the scattering site before interacting again. Scintillation light is produced at the points where energy is deposited in the detector. In the GRIP detector, the measured position of an event is approximately the centroid of these flashes, weighted by the light production.

The effect of multiple-site interactions was determined by Monte Carlo calculations. The effect is largest between 500 and 1500 keV, where the RMS deviation of the centroid is ~1.0 cm away from the γ-ray's original path. The result of multiple-site interactions is a broadening of the point spread function of the detector and, thus, the image.

3.4.5   Detector Effective Area

Figure 3.10 shows the sensitivity as a function of energy for the GRIP detector system, expressed as an effective area.

The effective area is the ratio of accepted events at a measured energy to the incident flux at that energy. For an ideal detector (100% absorption, perfect energy resolution), the effective area would be the geometric area of the detector. Accepted events are those that interact in the detector without triggering a veto in the shields, and also pass all of the selection criteria in the data analysis. These criteria include a measured position in the central 645 cm^2 of the detector and, for events with measured energies below 300 keV, a measured position in the front half of the detector.
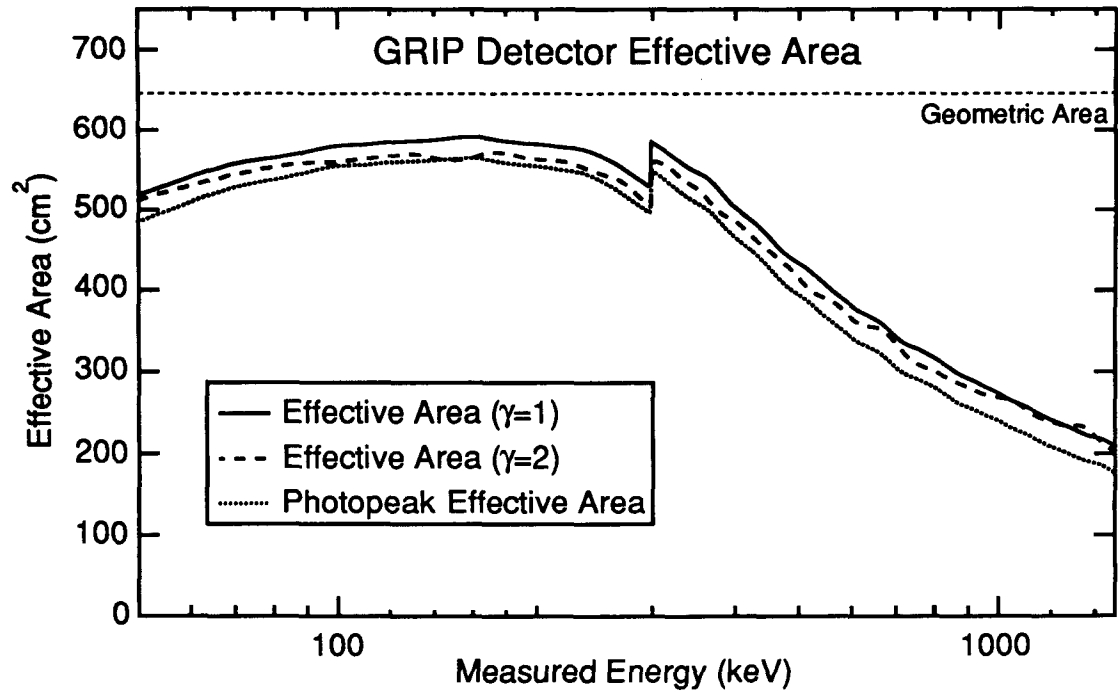
Figure 3.10 — The effective area of the detector as a function of energy, shown for two different incident spectra ($dN/dE = E^{-\gamma}$ for $\gamma=1$ and $\gamma=2$) and, for comparison, the limiting case of no off-photopeak contribution. The effective area of the detector is the ratio of the accepted count-rate at a measured energy to the incident flux at that energy.

Photons that deposit only part of their energy in the detector contribute to the effective area at a measured energy which is well below the original γ-ray energy. This makes the effective area at a given measured energy dependent on the incident spectrum. Figure 3.10 shows the difference between effective areas for two different spectra ($dN/dE \propto E^{-\gamma}$, for $\gamma = 1$ and $\gamma = 2$), as well as for the limiting case where the partial-energy events are simply ignored. The effect is small, but it is included in our analysis.

The effective area of the detector, however, is not the same as the effective area of the instrument. The effective area of the instrument depends on such things as the attenuation of γ-rays in the instrument and the efficiency of the imaging technique, in addition to the basic detector efficiency. The effective area of the instrument is discussed in §3.10.

3.4.5.1 Livetime

A factor which is not included in the effective area shown in Figure 3.10 is the livetime fraction. Most detectors, including GRIP, have two states: live and dead. Events that occur during deadtime are not detected, or are otherwise eliminated from analysis based solely on the time at which they occurred. Deadtime includes the time required for the detector system to recover from various events, such as a valid γ-ray event or the passage of a charged particle through the shield. If, for example, a γ-ray interacts with the detector at the same time as a charged particle passes through the shield (an "accidental coincidence"), the event is discarded even though the events were actually independent. The period when the shield is responding to a charged particle event is, therefore, detector deadtime.

The livetime fraction for most detectors, including ours, thus depends on the event rates in the detector and in the veto sources. Since these depend on the detector environment, the sensitivity shown is for the hypothetical case where there is no deadtime, corresponding to the limiting ratio of count rate to flux as flux→0. GRIP has special hardware to measure the livetime of the instrument. During our observations, the livetime fraction for GRIP was 90±1% (with an additional 6.6% decrease in livetime due to the calibration source (see §3.7) for energies below 110 keV for the D86, D268, and D414 observations).

3.5 The Mask

The mask is the second basic element of a coded aperture imaging system.

GRIP uses different masks in its two configurations. Each mask is composed of hexagonal lead blocks attached to a 1.2 m diameter sheet of aluminum hexcell (a lightweight construction of a 2.5 cm thick aluminum honeycomb bonded between two 0.5 mm thick aluminum sheets). Each lead block is backed by an 0.8 mm thick tin sheet, which absorbs 98% of the fluorescence X-rays produced near 75 keV by the lead. The size of the blocks at the distance between the mask and the detector defines the nominal angular resolution of the instrument.

The blocks are arranged in the HURA patterns shown in Figure 3.1a-b. Each mask pattern is composed of repetitions of a unit pattern consisting of 79 (configuration I) or 31 (configuration II) cells. Approximately half of these cells (39 or 15, respectively) are filled with lead blocks, with the remainder open to allow γ-rays to pass through.

The size of a unit pattern is approximately the same in each configuration, and is comparable to the detector area for which the event positions may be accurately determined (645 cm^2). The repetition ensures that the shadow pattern cast by a source anywhere in a large region of the sky contains a complete copy of the unit pattern (*e.g.*, the left half of one unit pattern and the right half of the adjacent one). This allows a large area of the sky to be simultaneously imaged, although sky locations corresponding to the same location on different unit patterns are indistinguishable for a given mask orientation. The ambiguity generated by the repetition of the unit pattern is resolved by rotating the mask at one revolution per minute, allowing each point on the sky to be imaged independently. As mentioned in Appendix A, the imaging artifacts that this produces are well-behaved, can be easily removed from the resulting image, and do not affect the region near the true source location.

The fully-coded field of view, (the sky region that is covered by the mask as seen from all of the detector's analyzed area) depends on the area of the mask covered with unit patterns. This mask area is limited by design considerations which, in the case of GRIP, constrain the weight of the mask to ≤140 kg.

3.5.1   Mask Configurations

The two masks shown in Figure 3.1a-b have different characteristics based on the astrophysical sources for which they were optimized. The original primary science target for GRIP was the Galactic center region, and this guided the original design of configuration I. When SN 1987A appeared, priorities were changed, and it became the new primary target. After the D86 flight, the GRIP experiment was optimized to observe this source, resulting in configuration II. The design of the mask is the main difference between the configurations.

The configuration I mask was optimized for observations of the Galactic center region. This region was known to contain numerous hard X-ray and γ-ray sources but, because of the limitations of earlier instruments, their locations and specific identities were not known. Traditional instruments did not have the angular resolution to isolate measurements of individual sources from other sources a few degrees away, which made it unclear which sources were being measured. Candidate sources were spread over a large area in the Galactic bulge, and so a wide field of view was one of the design objectives.

Configuration I has an angular resolution of 0.6° (the angular size of a 2.5 cm mask cell at the mask–detector distance of 2.5 m), allowing sources with this separation to be independently measured. For an isolated source detected with a significance of 10σ, the position may be determined to within 0.03° (see Appendix A), assuming that the telescope pointing direction can be determined to that accuracy. This degree of localization ability allows individual sources to be identified with counterparts observed in other spectral regions.

The fully-coded FOV of GRIP in configuration I is 20° in diameter, with a sensitivity independent of position. Sources up to 5° outside of this FOV are partially modulated by the edge of the mask, and may be imaged and measured with reduced sensitivity. This wide FOV allows the many objects in the Galactic center to be measured simultaneously. Other regions of the sky containing multiple sources have also been observed in this configuration, including Cygnus (with Cyg X-1 and Cyg X-3) and the region containing the Crab Nebula and Pulsar, Geminga, and A0535+26.

Configuration II was optimized for observations of SN 1987A. This supernova occurred in the Large Magellanic cloud, at a known location which is

well-isolated from other sources that were likely to be visible to our instrument. The flux from this source was predicted to be weak, despite its high intrinsic luminosity, due to the supernova's large distance (50 kpc) compared to sources in our Galaxy (typical distances ≲10 kpc). Flux from this object was also expected to be harder (more concentrated towards high energies) than the Galactic sources for which configuration I was designed, with interesting line emission near 1 MeV.

The goal of the configuration II optimization was high sensitivity at both high and low energies, at the expense of angular resolution and FOV. This optimization was implemented by replacing the original coded-aperture mask with a coarser one. The lead blocks used in the configuration II mask are both wider (4.8 cm vs. 2.5 cm) and thicker (2.8 cm vs. 1.9 cm) than those of the configuration I mask.

The increased block width was a better match to the detector's position resolution at low energies (shown in 3.7). Although the larger blocks decreased the angular resolution of the instrument to 1.1°, the expected lack of strong hard X-ray sources near SN 1987A reduced the importance of high angular resolution. The corresponding decrease in the ability to locate sources, to 0.045°, was deemed unimportant because the location of SN 1987A was already known, and because, in practice, source localization is limited by the accuracy to which the telescope pointing direction is known.

The increased thickness made the mask more effective at modulating the higher energy γ-rays. The increased mask thickness required that the coded area be decreased (reducing the fully-coded FOV) to keep the mask weight constant as

required by design constraints. The lead collimator, which was added as part of configuration II, has an angular response matched to this FOV (see §3.4.3.1).

The narrower FOV of configuration II still permits multiple simultaneous measurements of other sources. The Crab Nebula and Pulsar and A0535+26 were observed simultaneously with high significance using this configuration, as were multiple sources (1E1740.7-2942 and GX1+4) in the Galactic center region (Cook *et al.* 1991).

3.6 The Pointing System

The GRIP pointing system employed during the SN 1987A observations is almost unchanged from the original system described in Finger (1987). Most of the major elements of the pointing system can be seen in Figure 3.3.

The telescope is supported by the platform through bearings which allow it to rotate in elevation. The elevation motion is driven by stepping motors through a ball-screw arrangement, allowing the telescope to point at any elevation between vertical and 25° from the horizon (which allows imaging at the edge of the FOV, 7-10° lower than that). The platform is suspended from the balloon through a torque motor assembly, which drives the telescope to any desired azimuth.

The elevation and azimuth pointing direction are controlled by an onboard computer, the pointing microprocessor ($p\mu p$), which permits the telescope to function independently of ground control if desired, tracking astrophysical sources in a predefined pointing plan.

Telescope elevation is measured relative to the platform by shaft encoders (digital angle transducers). The orientation of the platform with respect to the

horizontal plane is measured by inclinometers. The azimuth relative to Earth's magnetic field is measured by redundant sets of magnetometers, one of which (software selectable) is used by the pμp for feedback to control the azimuth torque motor. The latitude and longitude of the telescope are measured continuously by an Omega radio location system, with updates transmitted to the pμp from the ground station as required to maintain pointing accuracy.

This active control system keeps the telescope pointed to within ~1° of its target direction during flight. After the flight, the data analysis software adjusts the position of each detected photon to compensate for the deviation between the measured telescope orientation and its target direction. This measured orientation is derived from data generated by the onboard sensors, which are included in the recorded data stream with a precision of the order of 10^{-2}°.

Although these sensors are of high precision, the pointing direction derived from the sensors may have an absolute error as large as 1°, as measured using reference observations of strong known astrophysical sources such as the Crab Nebula and Pulsar. To adjust for this pointing error, a Sun and star camera system was installed on the telescope for the D414 and D771 flights (see §3.6.1). As is discussed in the Data Analysis chapter (Chapter 5), this error is predominantly in the azimuthal direction.

3.6.1   Star and Sun Cameras

The Sun/star camera system is shown in Figure 3.11.

The Sun camera views the sky through two diagonal mirrors mounted on a rotation stage. These mirrors point in opposite directions as viewed by the camera, with the bottom mirror viewed through the top mirror. The top mirror,

called the star mirror, is partially silvered glass (75% reflection, 25% transmission). The bottom mirror, the Sun mirror, is unsilvered glass (~4% reflecting) and views the Sun through a neutral density #2 (10^{-2} transmission) filter. The image in the Sun mirror is thus attenuated a factor of ~10^{-4} with respect to the image in the star mirror, and can be ignored unless the Sun mirror is pointed towards the Sun, in which case it dominates. The Sun mirror is used only to observe the Sun. The star mirror can be used to observe bright stars (brighter than magnitude ~2) and planets. Although this was not necessary during our observations, the CCD camera and lens system has enough dynamic range to allow Sun observations to be made using the star mirror.

The field of view of the CCD camera is 9.3°×7.2°, so that each mirror can view a band of the sky ~8° wide on average (varying with the rotation of the field of view in the mirror). The Sun and star mirrors view bands of sky centered 90° and 95° away from the pointing direction of the telescope, respectively. These angles were chosen to allow the Sun and (on D414) Venus to be viewed during the SN 1987A observations. (SN 1987A is near the ecliptic pole, and so the separation between it and the Sun remains near 90° throughout the year. A similar system to view the Sun during an observation of the Crab would require the Sun mirror angle to be adjusted every few days to compensate for the annual motion of the Sun.)

The video signal from this camera was transmitted directly to the ground station on a 1 MHz bandwidth analog radio channel and, for the D771 flight, was also digitized and integrated on-board and included in the data stream. The 1 MHz video signal was recorded on ground-based VCRs and, for the D414 flight, these tapes were digitized and analyzed on a Megavision video analysis system.

The D771 pointing data was analyzed from the digitized images in the data stream.

The second camera in the system, the star camera, is an image intensified CCD camera, sensitive to stars as dim as magnitude 9 over a $5.8°×4.5°$ FOV. This camera is rigidly mounted on the telescope, pointing $50°$ to the left of the telescope pointing direction. This offset allows it to view the sky without being blocked by the balloon, even while the telescope is pointing vertically. It would be damaged by daytime and twilight skylight, even at balloon altitudes, and so it was unpowered during the daytime periods of the observations. Because the D414 and D771 observations of SN 1987A took place during the day, this camera was not used to determine pointing corrections for the SN 1987A observations. It was used, however, during our Galactic center observations during the night. These observations showed that the dominant γ-ray source in the Galactic center region was not the radio source at the dynamical center of the Galaxy, but a different source, 1E1740.7-2942, less than a degree away (Cook *et al.* 1991).

Figure 3.11 — The Sun camera system.

Axis of camera aligned with
telescope pointing direction

CCD camera

Lens

Rotating mirror assembly

75% reflecting / 25% transmitting
mirror for viewing stars

4% reflecting mirror (unsilvered glass)
for viewing sun

Neutral density #2 filter (1% transmission)
for viewing sun

To Sun

Rotation stage for turning
rotating mirror assembly
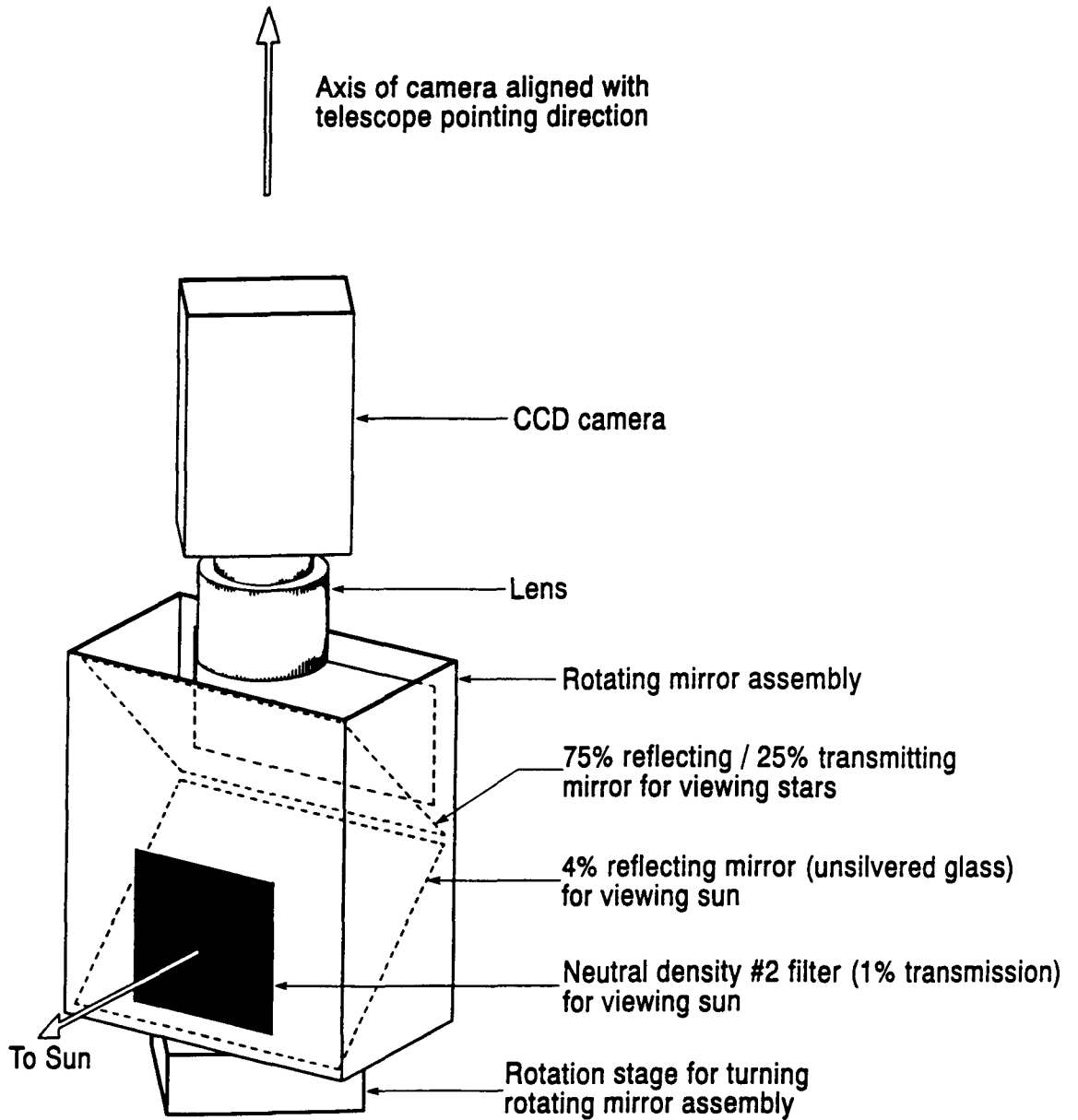
3.7   The Calibration Source

To provide a continuous measurement of instrument performance, a tagged γ-ray source was mounted on a tower above the mask. This source consists of a small amount (5 μCi) of ^{241}Am, embedded in a plastic scintillator. When this source decays, it produces a 60 keV γ-ray in coincidence with a 5.4 MeV α-particle (Lederer & Shirley 1978). The α-particle is absorbed by the scintillator, producing a flash which is detected by a small photomultiplier tube.

Events in the main camera plate that are "tagged" by coincidence with a scintillator flash from the calibration source are considered to be candidate calibration source events (CCSEs) if they have measured energies below 110 keV. These CCSEs are removed from the analyzed data to avoid contamination of astrophysical source data. The detector livetime for these energies is correspondingly reduced by 6.6% to compensate for the astrophysical γ-rays removed due to accidental coincidences with the calibration source tag.

The CCSEs are imaged with the same software as is used for imaging astrophysical sources. When used in this mode, the software compensates for the finite distance from the source to the mask, and uses a telescope-fixed rather than a sky-fixed reference frame, but otherwise executes exactly the same code.

As a result of the reduction in background provided by the tagging scheme, and the proximity and intensity of the source, the location and intensity of the calibration source can be measured on time scales of a minute to a higher precision than most astrophysical sources can be measured over their entire observation period. This provides a continuous check of most elements of

instrument function involved in imaging, such as detector efficiency and resolution, mask rotation, and data integrity.

3.8 Instrumental Attenuation

Materials in the instrument attenuate the γ-rays from sources in the field of view before they reach the detector. These materials include insulation, the mask support structure , and the pressure vessel containing the detector. Between the detector and the field of view (on a line passing through one of the holes in the collimator and an open cell in the mask) there is 1.6 g/cm^2 of instrumental material, of which 1.1 g/cm^2 is aluminum alloys.

An effect which is equivalent (in terms of data analysis) to attenuation in the instrument, is transparency of the 'opaque' mask cells (see Table 3.2 for the opacity of the lead in the mask at 1 MeV). γ-rays that pass through the lead blocks in the coded aperture without being scattered or absorbed are equivalent to γ-rays that are absorbed as they pass through open cells—the signal that is used in the image construction is produced by the contrast in attenuation. Above 500 keV, this results in a decrease in the effective instrument transmission with increasing energy.

The attenuation of γ-rays due to the materials in the telescope between the detector and a source was calculated using a combination of laboratory measurements and a standard software package, XCOM, (Berger & Hubbell 1987) for calculating the energy-dependent cross-sections of materials. The laboratory measurements determined the γ-ray attenuation of samples of the instrument materials at specific energies, confirming and refining the instrument model. The software was used with this model to calculate the instrumental attenuation of GRIP at all energies.

The results of this model are shown in Figure 3.12.

3.9   Imaging Factor

As discussed in §A.5, the finite position resolution of the detector reduces the detection efficiency of a coded aperture instrument. The "imaging factor," ε, is the amount by which both the peak height and the effective number of background counts are reduced. This results in a statistical significance for a detected source which is $\sqrt{\varepsilon}$ of what it would be for a detector with perfect
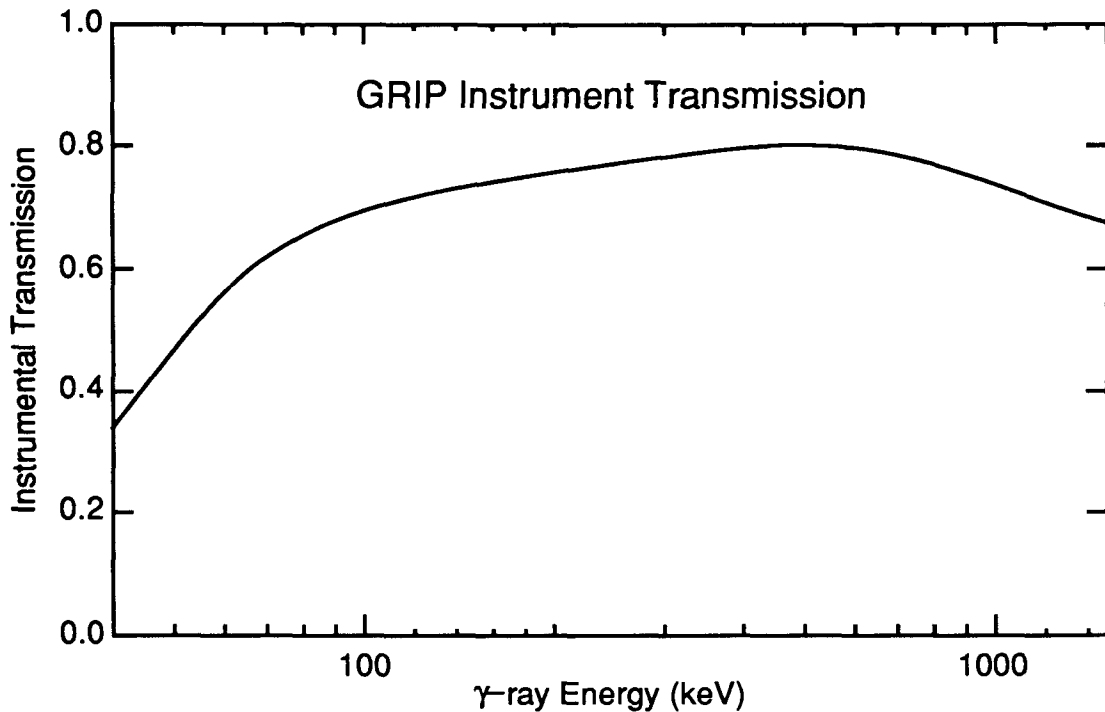
Figure 3.12 — The γ-ray transmission of the material in the instrument between the detector and a point in its field of view, adjusted for the transparency of the lead blocks used in configuration II. The effect of the collimator depends on the instrument configuration and the incidence angle of the γ-rays, and is omitted for clarity (see Figure 3.5).

position resolution. The value of ε depends on the relative sizes of the detector point spread function and the mask cells. Figure 3.13 shows ε as a function of energy for the two configurations.

3.10 Instrument Effective Area

The response of an instrument to a source may be described as an effective area. This is the detector area of an idealized instrument which would have equal sensitivity under the same observing conditions (livetime, atmospheric attenuation, and background). Figure 3.14 shows this effective area for GRIP in
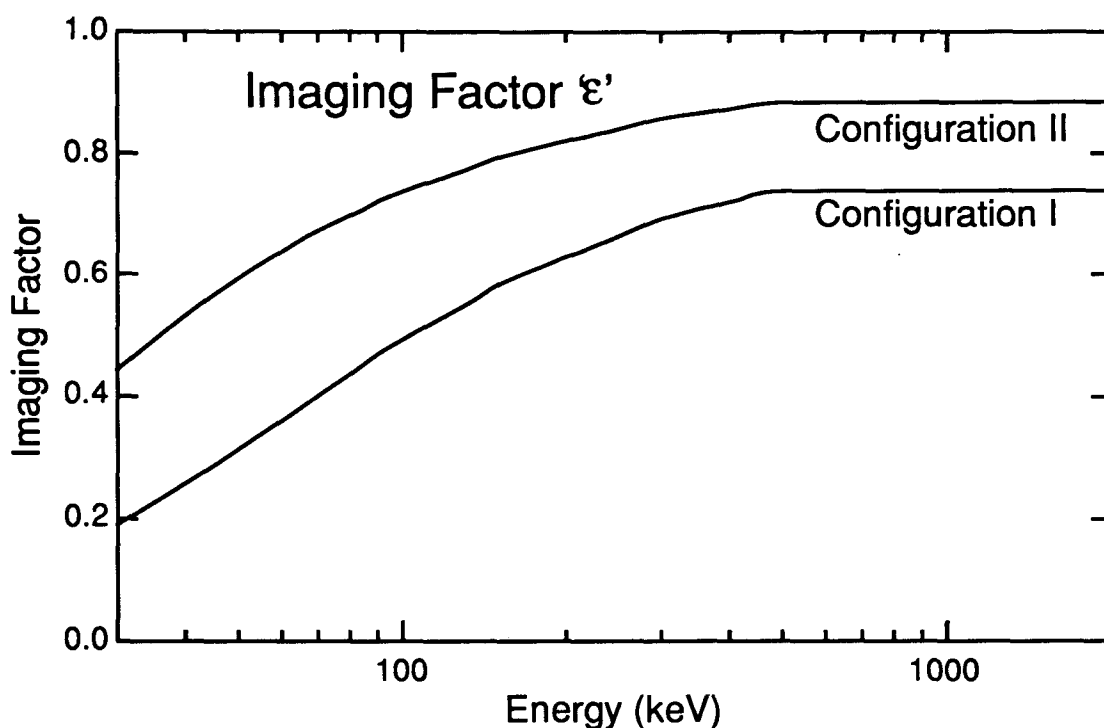
Figure 3.13 — The imaging factor "ε" as a function of energy for the two GRIP configurations (see §A.5).

its two configurations.

The idealized instrument is taken to be an ideal detector (which detects all incident photons) with no instrumental attenuation, used in the traditional on-source/off-source mode. In this mode, a detector spends half of its livetime observing a region of the sky containing the source, and the other half observing a source-free region of the sky.

The effective area of GRIP is equal to the product of the detector effective area (§3.4.5), the instrumental transmission (§3.8), and the square root of the imaging factor $\sqrt{\varepsilon}$ (§3.9).

GRIP Instrument Effective Area

Configuration I
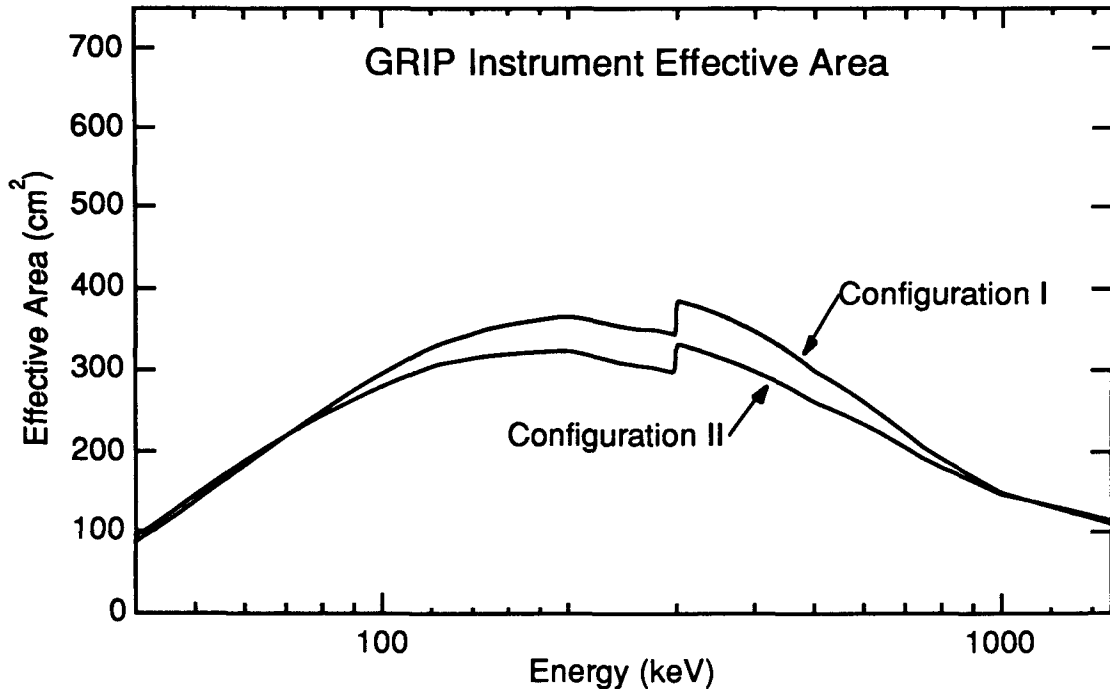
Configuration II

Figure 3.14 — The instrument effective area of GRIP in its two configurations for a

γ=1 spectrum, assuming that the source being observed is 1° from the

telescope axis. This is the detector area of an idealized instrument equivalent

to GRIP, as described in §3.9. The effects of the collimator (which increases the

attenuation in configuration II) and different mask cell sizes (which improves

the imaging factor, ε, in configuration II) partially offset each other. Although

configuration II has a smaller effective area, its lower background rate (see

Figure 3.4) at low energies makes it more sensitive than configuration I.

Chapter 4
Observations

4.1   Flights

GRIP has made four flights from Alice Springs, Australia, to observe SN 1987A. Before the explosion of SN 1987A GRIP had flown once, from Palestine, Texas, U.S.A. on 1986 October 15-16 (Althouse *et al.* 1987). All five flights were highly successful. The Alice Springs flights are summarized in Table 4.1. The names of the observations are based on the number of days since the explosion of SN 1987A, as measured from the observation of the neutrino burst on 1987 February 23.316 UT.

4.2   Pointings

The continuum sensitivity listed in Table 4.1 is the flux of a source at 100 keV, f_{100}, that would be detected at the 3σ level, assuming a γ=1 power-law spectrum ($dN/dE = f_{100}(E/100 \text{ keV})^{-\gamma}$) between 50 and 800 keV. The sensitivity of our instrument depends primarily on the source spectrum, the length of the observation, the attenuation of the atmosphere, the intensity of the background, and the configuration of the instrument.

Although the configuration of the instrument and the intensity of the background stay approximately constant during each observation, the attenuation of the atmosphere causes wide variations in instrumental sensitivity over a period of a few hours. Our observations of SN 1987A typically start when it rises above ~25° elevation, follow it as it reaches its highest point, which is at ~45° of elevation, and then follow it down as it sets below ~25° again. At our nominal float altitude of 120,000 feet ($\approx$ 36 km) this corresponds to a typical range of "grammages" (amount of atmosphere along the line-of-sight from the instrument to the source) over an observation of 6 - 11 g/cm^2. This range results in a factor of 2 difference in attenuation for 100 keV photons and a 40% difference at the line energies. For SN 1987A, one hour of observation through 6 g/cm^2 of air gives approximately the same sensitivity as three hours of observation

Observation (Day number)	Date[a]	Config.[b]	Livetime (hours)	Continuum Sensitivity[c] (10^{-5} cm^{-2} s^{-1} keV^{-1})
D86	1987 May 20	I	5.4	1.8
D268	1987 Nov 18	II	2.3[d]	2.1
D414	1988 Apr 12	II	11.1	1.2
D771	1989 Apr 4	II	3.3	1.9

[a]A detailed list of observations times is included in Appendix C

[b]The Configuration, as described in Chapter 3, specifies the mask and whether a collimator was used.

[c]Continuum sensitivity is the flux at 100 keV that would result in a 3σ detection of SN 1987A, assuming an E^{-1} power law spectrum between 50 and 800 keV.

[d]Includes only the period of time when the mask was rotating.

Table 4.1 — Summary of GRIP observations of SN 1987A.

through 11 g/cm^2 of air.

To compensate for these variations in sensitivity, each observation was divided into "pointings" of approximately 1 hour each (listed in the tables in Appendix C). These pointings were individually analyzed, and the results later combined. This permitted the pointings with greater sensitivity to be weighted more heavily than those with less sensitivity.

4.3   The Crab and Other Sources Studied

During the flights from Alice Springs, GRIP was used to observe other γ-ray sources in addition to SN 1987A. In particular, the SN 1987A observations were interspersed with observations of the Crab Nebula and Pulsar. These Crab pointings were typically 20-30 minutes long and were designed to provide diagnostic information about the instrument, although they are also scientifically useful observations of the Crab.

The Crab observations demonstrated that our instrumental pointing was usually accurate in elevation at the 0.1° level, but accurate in azimuth only at the 0.5° level (See §5.2.2 and the tables in Appendix C). The azimuthal errors tended to be systematic, showing definite trends over the course of each observation. These errors were interpolated and applied to the analysis of SN 1987A, as is described in Chapter 5.

The Crab Nebula and Pulsar complex, the remnant of the supernova of 1054 AD, is one of the brightest sources in the sky at hard X-ray and γ-ray energies. It also seems to be relatively constant in brightness over a time period of years (e.g., Jung 1989), and so it is provisionally used as a "standard candle" for calibration of hard X-ray and γ-ray instruments. Our analysis of the Crab data,

discussed in Chapter 5, yields a spectrum similar to those produced by other groups using other instruments. This suggests that our calibration is accurate, assuming that the Crab spectrum has not changed significantly over a time period of a decade.

During the D771 flight the source A0535+26, in the same field of view as the Crab, was in a giant outburst state, which occurs when the normal star of this binary system transfers mass to its neutron star companion as their orbit reaches periapsis. This resulted in two strong sources in our field of view, and demonstrated our ability to make simultaneous, independent measurements of each source (Cook et al. 1991).

In addition to the Crab and A0535+26, we observed the Galactic center region, and demonstrated that the brightest source of flux near the Galactic Center at energies of 30-200 keV is the source 1E1740.7-2942 (Cook et al. 1991), which is displaced from the dynamical center of the Galaxy by 0.8° (at least 100 parsecs). This result extended the measurements made by Skinner et al. (1987) which showed that 1E1740.7-2942 dominated the Galactic center flux at 20-30 keV. The source GX 354+0 also appears in our images of the Galactic center. We also observed Cygnus X-1, and used it to calibrate our pointing for the Galactic center observations. This data and data from the Cygnus region obtained during the 1986 flight from Palestine, is currently being analyzed.

4.4   Anomalies

Reliability of the GRIP instrument was provided by a combination of design, quality control, testing, and hardware redundancy. As a result, all five flights returned high-quality scientific data. In an instrument as complicated as GRIP, however, some problems are inevitable. Instrument malfunctions partially

impaired data collection during the D268 and D771 flights, although not enough to seriously affect our results. Minor problems during the other flights were corrected for with the redundant systems.

4.4.1   D268 Anomalies

During the D268 flight, data were lost as a result of two anomalies, one electronic and one mechanical.

The microprocessor that controls the telescope pointing had periods during which it continually reset itself, requiring manual reinitialization of the instrument before observations could be continued. Although this caused periods (85 minutes total, including 38 minutes scheduled for SN 1987A observations) during which no usable data were obtained, the remainder of the data are unaffected.

A more serious anomaly during the D268 observation is that the mask stopped rotating near the end of the flight, affecting 7 minutes of Crab observation and 68 minutes of SN 1987A observation. The data obtained during the period with the mask stopped are not included in the results presented in this thesis. Although imaging with a stationary mask is possible, and is the normal operational mode for many coded-aperture instruments (*e.g.*, Sigma (Paul *et al.* 1991), EXITE (Garcia *et al.* 1986)), it fails to provide some important advantages of a rotating mask system in eliminating systematic effects. The elimination of this subset of data from our analysis produces a ~25% reduction in nominal statistical sensitivity, but provides freedom from these sources of systematic errors. The utility of the data during the period when the mask is stopped is unaffected for analyses that do not require imaging, such as searches for pulsars and γ-ray bursts.

4.4.2 D414 and D771 Anomalies

During the entire D771 flight, and during short periods (totalling 39 minutes during the SN 1987A observations) of the D414 flight, the PMT viewing the calibration source scintillator failed. The calibration source could still be imaged for diagnostic purposes during these periods, although it required a longer exposure to achieve the same significance. However, without the tagging, individual calibration source γ-rays could not be distinguished from γ-rays from astrophysical sources.

A source at a finite distance from the mask, when imaged using software for infinitely distant sources, produces a complicated pattern in the resulting image. For a source as strong and as near as the calibration source, this 'out of focus' pattern covers the entire image with artifacts that can have significantly greater amplitudes than the image peaks produced by weak sources such as SN 1987A.

This pattern may be calculated numerically or analytically, or it may be measured with high statistical significance from data obtained while the tagging system was functional. The pattern can then be subtracted from the images obtained during the tagging system failure to remove the calibration source artifacts.

Alternatively, and more conservatively, the calibration source artifacts may be removed using an energy cut, eliminating all events with a measured energy consistent with the calibration source energy. This method provides freedom from systematic effects of the calibration source, at the expense of some sensitivity in the measurement. The tradeoffs between the increased complexity of the analysis for the first method and the reduction in sensitivity for the second

method depend on the details of the observation. For the SN 1987A observations, I have chosen the second method. To eliminate events produced by the calibration source, I discarded all data with measured energies below 77 keV during the time periods when the tagging system was not functioning. Imaging measurements show that this eliminates >95% (statistically consistent with 100%) of the calibration source events. Because of the low elevation angle of SN 1987A, few γ-rays at those energies would penetrate the atmosphere and reach our instrument (27% at 60 keV for 7 g cm^{-2} of air, line-of-sight). Assuming that the spectrum of SN 1987A is as predicted by a wide range of models, data at those energies would contribute only 3% to the sensitivity of our instrument for the detection of SN 1987A during the D771 observation.

Chapter 5
Analysis

Conventional and coded aperture γ-ray instruments have both similarities and differences in the way their data are analyzed. A detector count spectrum is produced, by methods that differ between the two classes of instruments, giving the distribution of photons as a function of measured energy. From this detector count spectrum and the known instrument response function, the spectrum of the source is estimated by standard techniques that are applicable to both classes of instrument.

In a conventional instrument, a collimated detector is alternately pointed towards and away from the source of interest to make source+background and background measurements. The difference in count rates between these pointings, with corrections made for sources of systematic error, gives a detector count spectrum which is assumed to be due to the source of interest. The sources of systematic error include other known and unknown sources in the field of view (FOV) of either the source+background or background measurements, and direction-dependent and time-varying backgrounds. Sources of time-varying background include induced radioactivity in the instrument, variations in the instrument environment resulting from altitude or geographic location changes, and changes in the detector response.

A well-designed coded aperture instrument provides an independent detector count spectrum of each resolution element (a region the size of the instrument resolution) in the FOV, allowing multiple sources in the FOV to be measured without cross-contamination of the data. Because both source and background rates are measured simultaneously, the data are immune to time-dependent background variations. The use of a rotating coded aperture, as on GRIP, provides immunity to the effects of spatial non-uniformity in the background over the area of the detector.

The analysis techniques employed to convert a detector count spectrum into a source spectrum are dependent only on the instrument response function, and not on whether the instrument used to obtain the detector count spectrum is conventional or coded aperture. These techniques are described in §5.3.

5.1   Image Production

Analysis of data from a coded aperture instrument produces an image of the sources in its field of view (Dicke 1968; Ables 1968). Both the analysis procedure and algorithm used to generate the image are described in detail in Cook *et al.* (1984) and Finger (1987). A description of coded aperture imaging, including additional references, is given in Appendix A.

The image construction procedure assigns each point, $\vec{x}$, on the image a value (the "image value," $I(\vec{x})$). Each $\vec{x}$ on the image corresponds to a point on the sky determined by the telescope pointing direction and the details of the construction. The image is a map of the number of photons coming from each point in the field of view in excess of the average "background" level, convolved with the telescope angular response function. The expectation value, $\langle I(\vec{x}) \rangle$, at a point on the image corresponding to a point source on the sky is proportional to

the number of photons received by the telescope from that source. The variance of the image value at each point on the image is proportional to the total number of photons used in the image reconstruction, including those from instrumental and atmospheric background and from other astrophysical sources in the field of view.

To analyze the spectrum of a source, the data are divided into bins with different ranges of measured energies and over different time periods, and a set of images is made. The image value is obtained for each image in the set at a "measurement location," $\vec{x}_{meas}$, corresponding to the direction of the source. Each image value provides an estimate of the detector count rate from a given direction for the image's measured-energy range and time period. Values from images made from disjoint datasets (*e.g.*, non-overlapping measured-energy ranges or time periods) provide statistically independent measurements. Taken together, the image values form a detector count spectrum (or a series of detector count spectra over time) that can be converted into a source spectrum by standard techniques (§5.3).

5.2   Determining the Measurement Location

An imaging instrument, by definition, produces a separate measurement for each resolution element in the sky. The location of the source of interest on the image must therefore be determined before its spectrum can be obtained. The image values at that location form a detector count spectrum. To reduce systematic errors, this measurement location should be determined as accurately as possible.

5.2.1   Source Location

In an image containing a peak due to a source at a known location in the sky, there are several important locations:

$\vec{x}_{nom}$ ≡ nominal location : a priori predicted location of the source peak, based on the best estimate of the telescope pointing direction.

$\vec{x}_{actual}$ ≡ actual location : the theoretical expected location of the peak based on the actual (perhaps unknown) telescope pointing direction.

$\vec{x}_{obs}$ ≡ observed location : location of the maximum of the peak.

$\vec{x}_{meas}$ ≡ measurement location : location where the measurement is made.

The difference between $\vec{x}_{nom}$ and $\vec{x}_{actual}$ is due to errors in the measurement of the telescope pointing direction, while the difference between $\vec{x}_{obs}$ and $\vec{x}_{actual}$ is due to statistical effects in the image reconstruction. These locations are used to choose $\vec{x}_{meas}$.

The telescope pointing direction is continuously derived during data analysis from the aspect sensors described in §3.6. This derived direction is compared to the telescope's desired pointing direction, and the deviation is used to individually adjust the position of each photon to the position on the detector it would have had for the case of no deviation. These adjusted photon positions are then used in the image reconstruction. If the derived pointing direction has

systematic errors, then the $\vec{x}_{actual}$ of a peak in the reconstructed image will be correspondingly displaced from $\vec{x}_{nom}$. As discussed in §5.2.2, these systematic errors in pointing do exist, and are of the order of 0.5°, primarily in the azimuth direction.

While systematic errors displace $\vec{x}_{actual}$ from $\vec{x}_{nom}$, statistical errors displace

$\vec{x}_{obs}$ from $\vec{x}_{actual}$. The $\vec{x}_{obs}$ for a source strong enough to produce a significant peak is displaced from $\vec{x}_{actual}$ with a standard deviation that is inversely proportional to the significance of the peak. This uncertainty is described in Appendix A. For a weak source the observed peak, chosen as the highest peak near to $\vec{x}_{nom}$, may be purely a statistical fluctuation, totally unrelated to the low-significance theoretical peak.

The image values obtained at $\vec{x}_{meas}$ form a detector count spectrum which may, depending on the choice of $\vec{x}_{meas}$, be biased. If $\vec{x}_{meas} = \vec{x}_{actual}$, then the detector count spectrum will be unbiased (Finger 1987). If $\vec{x}_{meas} = \vec{x}_{nom}$ and $\vec{x}_{nom} \neq \vec{x}_{actual}$, the detector count spectrum will be negatively biased—because those image values are 'downhill', away from the actual location of the expected peak. Use of $\vec{x}_{meas} = \vec{x}_{obs}$ provides a positive bias—the local maximum image value is, by definition, greater than or equal to the image value at $\vec{x}_{actual}$. This bias is inversely proportional to the significance of the detection.

5.2.2 Pointing Offsets Derived From Crab Observations

Since $\vec{x}_{actual}$ is not available from the data, the choice of $\vec{x}_{meas}$ must be based on $\vec{x}_{obs}$ and $\vec{x}_{nom}$. $\vec{x}_{obs}$ is available for sources intense enough to produce a significant peak, while $\vec{x}_{nom}$ is available for sources at known sky positions. The statistical position error,

$$\vec{\Delta}_{stat} = \vec{x}_{obs} - \vec{x}_{actual} ,$$

has a variance, σ_{stat}^2, that can be calculated from the significance of the peak

(Appendix A), while the systematic error,

$$\vec{\Delta}_{sys} = \vec{x}_{actual} - \vec{x}_{nom} ,$$

must be estimated from the total observed peak displacement from the nominal

position:

$$\vec{\Delta}_{tot} = \vec{\Delta}_{stat} + \vec{\Delta}_{sys}$$

$$= \vec{x}_{obs} - \vec{x}_{nom} ,$$

which can be measured from the image. A comparison of the magnitudes of

these distances is used to determine whether the statistical or systematic position

error dominates.

During the SN 1987A observations, this comparison was done for data

from the Crab Nebula and Pulsar pointings that were interspersed among the

SN 1987A pointings, as described in Chapter 4. This provided pointing offsets,

Δ_{az} and Δ_{el} : adjustments to the sensor-derived azimuth and elevation of the

telescope which reduced the $\vec{\Delta}_{tot}$ values to zero for the adjusted images. These

pointing offsets are given in Tables C.1a-d in Appendix C.

The azimuthal error tends to dominate the pointing error (azimuthal

errors are at the ~0.5° level and elevation errors are at the ~0.1° level), and the

azimuthal error tends to vary systematically with time. The elevation errors tend

to be smaller and more static.

5.2.3   Pointing Offsets Used For The SN 1987A Observations

Because SN 1987A is a much less intense γ-ray source than the Crab, the

pointing error cannot be measured for each individual pointing. The pointing

error was therefore estimated by other means. The assumption was made that, when no additional data were available, the best estimate of the required Δ_{az} and Δ_{el} values would be obtained from the Δ_{az} and Δ_{el} values measured during the closest Crab observations.

During the D414 and D771 observations, the Sun camera system provided additional information on the telescope pointing direction. This camera, described in §3.6.1, views the Sun and bright stars and planets using a mirror mounted on a rotation stage. During these flights, the camera had either the Sun or Venus in its view throughout the SN 1987A observations, but no bright targets were available during the Crab observations.

The Sun camera observations constrain one degree of freedom of the telescope pointing direction, the distance between the telescope pointing direction and the Sun camera pointing direction.

To constrain a second degree of freedom during these flights, the Δ_{el} values from adjacent Crab pointings were used to choose Δ_{el} for each SN 1987A pointing. A Δ_{az} value was then calculated for each pointing that satisfied both the Sun-telescope angle and Δ_{el} constraints. These Δ_{az} and Δ_{el} values were used to image SN 1987A. The result of applying these offsets to the image reconstruction was, for the significant peak that was found for the D414 observation, a peak displacement for SN 1987A of $\vec{\Delta}_{tot} = 0.2°$. This displacement is larger than is compatible with the expected statistical deviation ($\sigma_{stat} = 0.05°$ in each axis) and is due to residual systematic pointing errors.

The Sun camera system was not implemented at the time of the D86 and D268 observations. For these flights, Δ_{az} and Δ_{el} values were interpolated or extrapolated from the values for the Crab measurements and used to image the

SN 1987A pointings. This resulted, in the case of the significant peak that was found for the D268 observation, in an observed location that is 0.3° away from the nominal location. This displacement is also inconsistent with the σ_{stat}=0.09° per axis statistical deviation for this observation, and so it too must be ascribed to residual systematic pointing errors.

The Δ_{az} and Δ_{el} values used for each SN 1987A pointing in the spectrum analysis, along with the Crab pointing values, are shown in Tables C.1a-d in Appendix C.

For the D268 and D414 observations, $\vec{x}_{meas}=\vec{x}_{obs}$ was used in the data analysis of SN 1987A. For the D86 and D771 observations, which had no significant image peaks, $\vec{x}_{meas}=\vec{x}_{nom}$ was chosen for the data analysis.

These selections cause bias, and in the case of the D86 and D771 the bias is negative. However, this bias can be constrained by repeating the analysis with $\vec{x}_{meas}=\vec{x}_{obs}$, choosing the highest peak within 1° of $\vec{x}_{nom}$ as the measurement point. (In both observations, this peak was consistent with, and assumed to be, a statistical fluctuation.) When this was done, it raised the resulting upper limits by less than 15%.

5.3   Converting From Images to a Spectrum

The conversion of a detector count spectrum to a source spectrum is an "inverse problem," one of a class of problems known to be difficult (see Craig & Brown 1986, which provides a review of this problem in astronomy). The telescope sensitivity is highly energy-dependent and the source is attenuated by varying amounts of atmosphere. The low significance of many measurements requires that the analysis have good statistical efficiency. The finite energy

resolution of the detector makes the detector count spectrum at each measured energy dependent on the source spectrum over a wide energy range, and the source flux can be highly energy-dependent, so that a single derived flux may not be valid across all of a wide energy range required for a statistically significant measurement.

Inverse problems such as this are well known and are not restricted to the coded aperture imaging technique used in GRIP, nor are they unique to γ-ray astronomy. The Backus-Gilbert method of solving inverse problems, for example, was developed for the analysis of geophysical data (Loredo & Epstein 1989).

5.3.1   Direct Deconvolution

A naïve solution to the inverse problem is to directly deconvolve the data with the instrument response, *e.g.*, by multiplying the measurements by the inverse of the instrument response matrix.

Unfortunately, this method does not yield good results. The spectra resulting from such a straightforward approach tend to be unstable with respect to small, statistically insignificant variations in the measurements, and can show features that are not justified by the data (Craig & Brown 1986).

One reason for this is that there are an infinite number of possible spectra consistent with any dataset. To make the analysis problem well-posed, *a priori* constraints must be applied. These constraints may be based on prior knowledge, or they may be chosen merely to select a well-behaved solution.

5.3.2 Other Methods

A survey of some of the methods suggested to solve the inverse problem is given in Jeffrey & Rosner, (1986). For example, in the Phillips-Twomey method and in the maximum-entropy method (MEM), the constraint is that the derived result is the "smoothest" consistent with the measurements, where smoothness is defined in terms of the value of some order of derivative (Phillips-Twomey) or in terms of the integral of a non-linear function of the result (MEM).

5.3.3 The Trial Spectrum Method

I have chosen a modification of the trial spectrum method (Fenimore, Klebesadel & Laros 1983) to analyze the SN 1987A data. In this traditional model-fitting method, the constraint takes the form of a model spectrum or set of model spectra with one or more adjustable parameters (*e.g.*, spectral index, effective temperature, the overall intensity of the spectrum). The choice of models may be based on previous measurements of the source or similar sources, convenient representations (*e.g.*, power-law spectra), or physical models (*e.g.*, spectra predicted for thermal plasmas).

Selection of models and variation of parameters produces a set of trial spectra. A trial spectrum is convolved with the known instrumental response function to predict a detector count spectrum, which is compared to the measured detector count spectrum using a least-squares method. (If the instrument had non-Gaussian errors or if the detector spectrum were not linear with flux, some other variant of the maximum likelihood function would be required. However, the statistics of GRIP are sufficiently well-behaved that the least-squares method is appropriate.) The best fit trial spectra, and the goodness

of their fits, are used to choose a model and a set of parameters and their statistical uncertainties (Lampton, Margon & Bowyer 1976).

Once a trial spectrum has been chosen which provides a good fit, all parameters are frozen except the overall intensity. This spectrum defines a "template," $T(E)$, with a specific shape and a flux normalized for convenience. The template is not unique; it is merely the best template among the set of models tested and not necessarily the best of all possible models. A unique solution is precluded by the nature of the inverse problem.

For a chosen measurement $I_i(\vec{x}_{meas})$, where i specifies a selected time and measured-energy range, a spectrum may be estimated:

$$f_i(E) = \kappa_i T(E)$$

where κ_i is chosen by least-squares minimization and, in the case of data derived from GRIP images, is linearly proportional to the measurement. Independent measurements produce independent values of κ_i. (This ignores the slight dependence produced by the use of the data to choose the template. This point will be discussed in §5.3.5.) If the values of κ_i are statistically consistent, then that indicates a valid template.

Consistent values of κ_i may be combined to give a value, κ, with optimal statistical significance. Combining κ_i from a subset of the measurements (*e.g.*, the measurements over a range of times and measured energies) gives a combined spectral measurement which is independent of those made with other subsets from non-overlapping time or measured energy ranges. If the measurements are normally distributed and linear (as they are with GRIP) this analysis is equivalent to a χ^2 fit of the dataset to the template, with the normalization κ as the only free parameter.

5.3.4 Application To GRIP

A template spectrum $T(E)$ is convolved through an image-specific instrument response function: $R_i(E, \vec{x})$. The subscript i indicates the particular image, specifying its livetime, measured-energy range, total number of image counts, line-of-sight atmospheric depth, and any other factors that may affect the instrumental sensitivity. E represents a true photon energy (as opposed to the measured energy) and $\vec{x}=\vec{x}_{meas}$ signifies the point on the image corresponding to the location of the source. For a source with a flux given by $T(E)$, the image value is expected to be

$$\langle I_i(\vec{x}) \rangle_T = \int R_i(E, \vec{x}) T(E) dE \ .$$

The variance of the image is independent of the flux of the source (in the background-dominated case of our measurements):

$$\sigma_i^2 = \langle I_i^2(\vec{x}) \rangle_{T=0}$$
$$= \varepsilon N_i$$

where N_i is the number of photons used in the image reconstruction and ε is a number (the imaging factor) less than but of order unity, which indicates the effect of the finite position resolution of the detector (Finger 1987). The imaging factor ε as a function of energy for the two GRIP configurations is shown in Figure 3.13.

The calculated instrument response to the template spectrum, when compared to the actual image response $I_i(\vec{x})$, is used to find the flux normalization,

$$\kappa_i = I_i(\vec{x}) / \langle I_i(\vec{x}) \rangle_T$$

which gives the best estimator of the flux of the source at $\vec{x}$:

$$f(E, \vec{x}) = \kappa T(E).$$

The usual linear regression method of parameter estimation is employed to combine the normally-distributed, linear measurements:

$$\kappa = \sigma_\kappa^2 \sum_i \frac{I_i(\vec{x})\langle I_i(\vec{x})\rangle_T}{\sigma_i^2}$$

$$\sigma_\kappa^2 = \frac{1}{\displaystyle\sum_i \frac{\langle I_i(\vec{x})\rangle_T^2}{\sigma_i^2}} .$$

These summations are typically over restricted subsets of images, such as those in a particular range of measured energies. In that case, the calculated spectrum $f(E, \vec{x}) = \kappa T(E)$ will tend to be most accurate in the corresponding true energy range and less trustworthy outside that range. (Although this is true for the results presented in this thesis, there can be exceptions to this: *e.g.*, for a line spectrum, a measured energy bin that does not nominally contain the line energy may still be dominated by line photons unless the energy ranges are chosen to avoid this.)

5.3.5   Template-Dependence and How It Is Handled

The results of this type of analysis, however, are template-dependent. In particular, the data used in the trial spectrum method tend to be "obliging" (Fenimore, Klebesadel & Laros 1983)—the measurements obtained tend to move in a direction that better approximates the template used. The spectrum derived from a dataset using a hard template tends to be harder than the spectrum derived from the same dataset using a soft template. In addition, when the template is chosen based on a set of data, this makes all measurements derived from that template dependent on that set of data, reducing the statistical independence of the measurements.

This template dependency may be compensated for, either explicitly or implicitly. As an example, consider the case of a power-law template:

$$T_\gamma(E) = E^{-\gamma}$$

$$f(E) = \kappa_{E_0,\gamma} T_\gamma(E)$$

$$= f_\gamma(E_0)\left(\frac{E}{E_0}\right)^{-\gamma},$$

where E_0 is an energy chosen for convenience and $\kappa_{E_0,\gamma} = f_\gamma(E_0)/T_\gamma(E_0)$ is the normalization to be calculated. If the analysis of the data with measured energies in the 50-200 keV range gives

$$f_{\gamma=1}(100 \text{ keV}) = 1.0 \times 10^{-3}$$

$$f_{\gamma=2}(100 \text{ keV}) = 1.2 \times 10^{-3},$$

(omitting the units and standard errors for clarity), then that dependence may be made explicit by quoting the flux at E_0 as a linearized function of γ:

$$f(100 \text{ keV}) \approx (0.80 + 0.20\gamma) \times 10^{-3}.$$

It is, however, more convenient to note that:

$$f_{\gamma=1}(120 \text{ keV}) = f_{\gamma=2}(120 \text{ keV}) = 0.83 \times 10^{-3}$$

and quote $f(120 \text{ keV}) = 0.83 \times 10^{-3}$ without explicit reference to the template γ. Other γs in a range around 1 and 2 will give fluxes that are close enough to the $\gamma=1$ and $\gamma=2$ cases that the flux at 120 keV can be considered model independent. This is the "bow tie" method, named after the shape of the graph used to determine the energy at which the flux should be quoted (Van Allen 1974). Although different observations have different bow tie energies, a compromise energy can be chosen to allow the comparison of the results of different observations while retaining some measure of template-independence. For the continuum results described in Chapter 6, the bow tie energies are chosen so that the measured fluxes vary by less than 25% of one standard deviation, and the upper limits vary by less than 25% of their value, when the γ of the template is

varied by unity. The typical variation is approximately 10% of one standard deviation or upper limit.

5.3.6 The Template Used For SN 1987A

For this analysis of SN 1987A, the choice of a template was based on the results of a wide variety of Monte Carlo models (*e.g.*, 10HMM, S90, and other models referenced in chapter 2), and on our data.

These models, at the times of our D268 and D414 flights, are well-approximated between 50 and 800 keV by a power-law template with γ in the range 1.0-1.4. The γ used in the template is obtained from a χ^2 model fit to the data in the 50-800 keV measured-energy range for the D268 and D414 flights.

For the D86 and D771 flights, our measurements detect no significant flux from the location of SN 1987A, so a fit to the data is not useful in choosing a template. The models predict no significant flux at D86, but if there were flux, caused by ^{56}Co mixed into the outermost fringes of the envelope, it would probably have a spectrum similar to that of D268 and D414. The D771 model spectrum above 137 keV is similar (but lower in intensity) to the earlier spectra, but dominated by flux from ^{57}Co at and below that energy. Using a template based on the D771 model spectrum does not result in a detection of flux from SN 1987A. (This was expected, and places a loose constraint on the amount of ^{57}Co produced, as discussed in §7.4.1.) Since the D86 and most of the D771 spectra are expected to be similar to the D268 and D414 models, I have chosen a power-law template for the analysis of the data between 50 and 800 keV for these flights. I have arbitrarily set γ to unity for simplicity and for ease of comparison with the D268 and D414 flights. A change in γ by ±1 results in a change in the quoted upper limits in Table 6.2 by less than 25% (at the bow-tie–selected

nominal energies), and a search over a wide range of γ (0-5) does not result in a detection of the source.

Above 800 keV, the spectrum is more complicated and more dependent on the Monte Carlo model. Because the energy-dependence of the instrument response is reduced at these energies, the results are less sensitive to the template. I have chosen the minimal-assumption approach, using a flat template with a constant $T(E)$ to derive the continuum flux in these high-energy bins.

Most of the measured-energy bins used in the SN 1987A analysis are wide compared to the energy resolution of the detector. This restricts the flux contribution to each of these bins from photons with a true energy outside of the nominal bin boundaries to $\leq 10\%$ of the calculated flux. The dominance of photons from within the nominal bin enhances the independence of the flux measurement from the analysis technique.

The exceptions are the narrow bins at the 847 and 1238 keV line energies. The flux in these bins is expected to be a combination of line and continuum flux, with the continuum contribution approximately proportional to the bin width and the line contribution asymptotically approaching a constant for a bin wide enough to contain essentially all of the line flux. To measure the physically interesting parameters of the flux in this region, the data were fit to a model containing both line and continuum flux.

5.3.7 Using the Template For Optimal Source Detection

A template can be used to determine the optimal weighting factors for combining many images into one. Using the set of images analyzed to obtain a spectrum, a composite image can be obtained which is approximately calibrated

by the template normalization and its variance at each point:

$$I_K(\vec{x}) = \sum_i w_i \, I_i(\vec{x})$$

$$\sigma_K^2 = \frac{1}{\displaystyle\sum_i \frac{\langle I_i(\vec{x_0})\rangle_T^2}{\sigma_i^2}}$$

where the weights, w_i, are given by

$$w_i = \sigma_K^2 \frac{\langle I_i(\vec{x_0})\rangle_T}{\sigma_i^2}$$

The image has optimal statistical sensitivity near the chosen $\vec{x_0}$ for detecting sources with spectra that match the template, and tends to have good sensitivity elsewhere. The variation with position is due to such factors as the collimator response function and variation in atmospheric attenuation with a source's elevation angle. The technique may be extended using weights that vary with position, although this results in variation of σ_K^2 with position.

5.4 Upper Limit Confidence Levels

I have chosen to use a 95% confidence level for upper limits in this thesis, incorporating the physical constraint of non-negativity of source flux. This is an alternative to the method of quoting an upper limit that is n standard deviations above the measurement, where n is typically 3 (*e.g.*, Sandie *et al.* 1988b) or 2 (*e.g.*, Matteson *et al.* 1990). Due to statistical fluctuations, the initial measurement of a source that is not producing significant flux may be negative or positive and, approximately one time in 40, may be negative by more than 2σ. There is thus a non-negligible chance that a 2σ upper limit will be below the physical lower limit of zero flux. Incorporating the physical constraint eliminates this problem and gives a more meaningful result.

Given a Gaussian distribution based on the measured $f \pm \sigma_f$, some fraction $F = \frac{1}{2}\mathrm{erfc}\left(\frac{-f}{\sqrt{2}\sigma_f}\right)$ of the distribution is positive, where $\mathrm{erfc}(x) = 1 - \mathrm{erf}(x)$ is the complementary error function. If f_{ul} is the 95% confidence level, then 95%×F of the distribution is between 0 and f_{ul}, while 5%×F of the distribution is above f_{ul} (see Figure 5.1). For a (1-α) confidence level:

$$\mathrm{erfc}\left(\frac{f_{ul} - f}{\sqrt{2}\sigma_f}\right) = \alpha\,\mathrm{erfc}\left(\frac{-f}{\sqrt{2}\sigma_f}\right).$$

The definition of this upper limit is well understood: If the parent distribution of source strengths f_0 sampled by the measurement is uniformly distributed between 0 and ∞, 95% of those measurements that yield the value f will be measurements of sources with true fluxes $f_0 < f_{ul}$.

The use of a uniform source strength distribution may be philosophically troubling, since strengths of astrophysical sources in the real world are not uniformly distributed, but such assumptions are hidden in many statistical measures, including $f + n\sigma$ upper limits. The search for the *meaning* of these upper limits, as opposed to the definition given above, leads to the Bayesian controversy, which is beyond the scope of this thesis.

5.5   Analysis Procedure Verification

To verify the analysis technique and the calibration of the instrument response, I analyzed the data from each observation of the Crab Nebula and Pulsar using the same imaging and analysis techniques as were applied to the SN 1987A observations. The results are in good agreement with spectra obtained by other instruments (*e.g.*, Jung 1989).

As an example of this, I present the spectrum obtained from the D414 Crab data. During this flight, seven Crab pointings were made, with a total instrument livetime of 2.0 hours. Images were created employing the pointing offsets given in Table C.1c in Appendix C. Image values were measured at $\vec{x}_{meas}=\vec{x}_{obs}$. These data were fit to a power-law trial spectrum of the form $dN/dE = \kappa_{100}(E/100$ keV$)^{-\gamma}$ between 50 and 800 keV, resulting in a best fit (reduced $\chi^2 = 0.84$ with 579 d.o.f.) with $\gamma=2.23\pm0.06$, and a flux at 100 keV of $\kappa_{100}=(55.2\pm1.3)\times10^{-5}$ (cm^2 s keV)$^{-1}$. Fluxes were then calculated in narrower energy bins, employing this spectrum as a template.

The results of the analysis of the D414 Crab observations are shown in Figure 5.2. For comparison, the solid curve shows the results of the HEAO A-4 observations of the Crab made during the years 1977 and 1978 (Jung 1989). This measurement covers the same energy range as our measurement, provides high
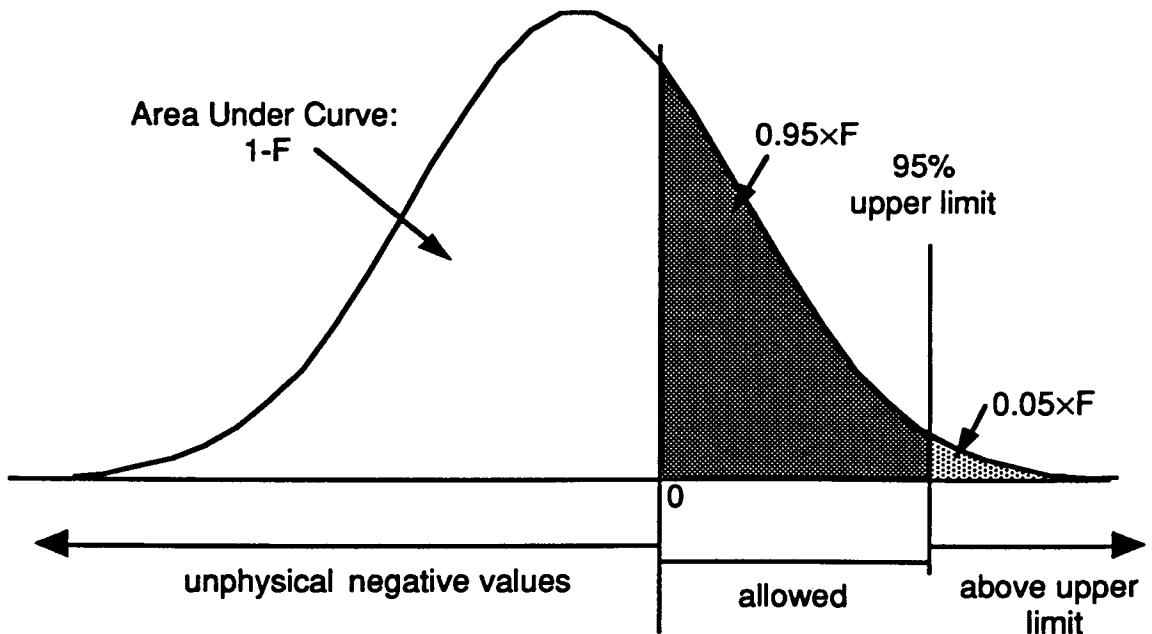
Figure 5.1 — The definition of 95% confidence level used in this thesis.

statistical precision, and is consistent with other measurements. Our measurements and those from HEAO A-4 are consistent in overall normalization and slope at the 10% level. The good agreement found between the measurements strengthens our confidence in both our instrument calibration and our analysis technique.

Figure 5.2 — The spectrum of the Crab Nebula and Pulsar complex. Data points
   are our measurements from the D414 observation (1988 April 12). The
   horizontal error bar of a point represents the measured-energy range of
   the measurement. The horizontal location of the vertical error bar is the
   bow tie energy. The line is a spectrum obtained from the HEAO A-4
   instrument in 1977-1978 (Jung 1989).
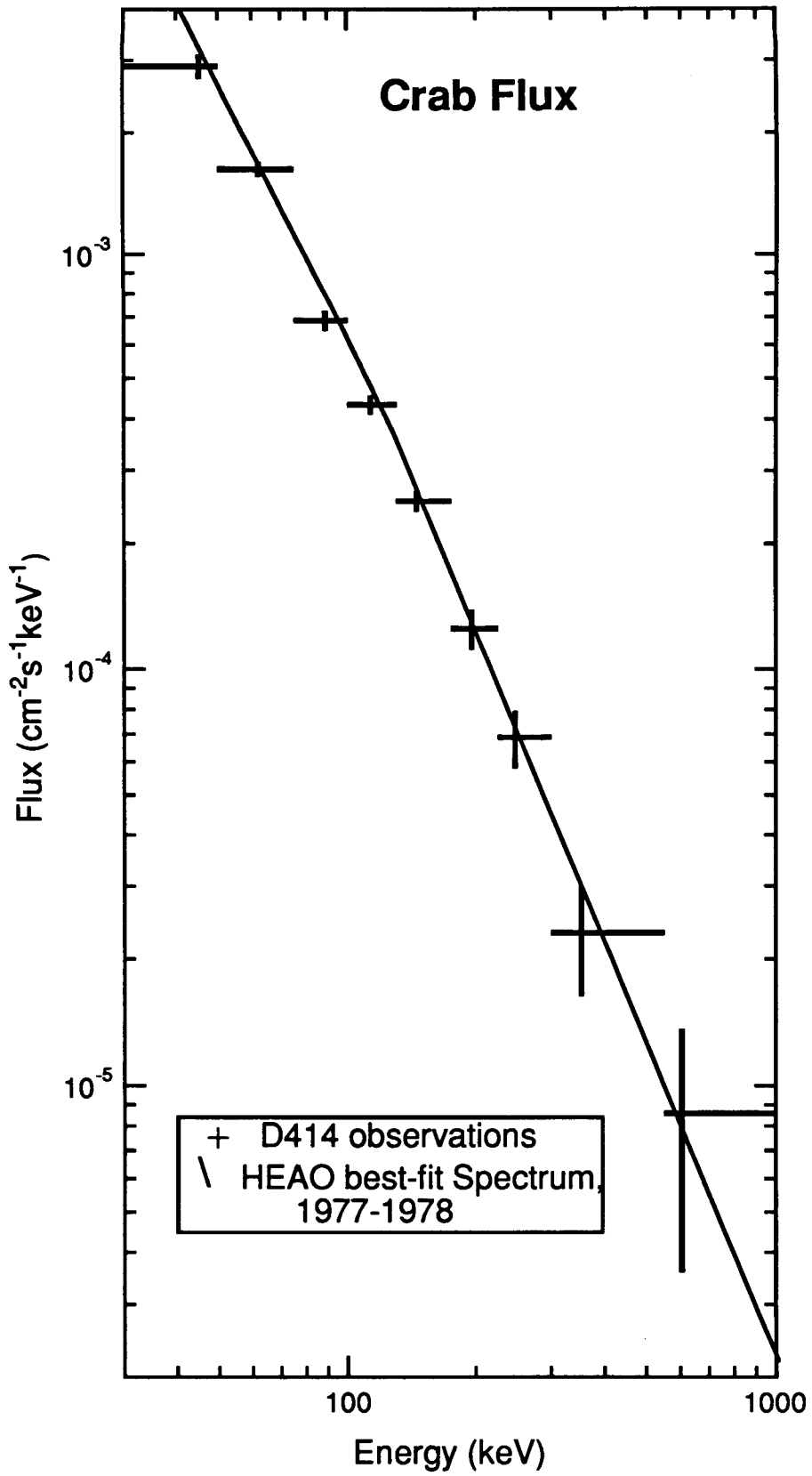
Chapter 6
Results

6.1   SN 1987A Images

Figures 6.1a-d are the images of the sky region containing SN 1987A
obtained from the four GRIP observations. These are composite images,
produced using a power-law continuum template with $\gamma=1$ between 50 and 1600
keV. This simple template over this energy range was found to produce high-
significance peaks for the D268 and D414 observations (4.9σ and 8.8σ,
respectively). Physically reasonable templates for the D86 and D771 observations
did not reveal any significant ($\geq 3\sigma$) peaks near $\vec{x}_{nom}$ for SN 1987A. These test
templates included power-laws with γ in the range 0 through 5, thermal
bremsstrahlung for energies from 10 keV to 1 MeV, and, for the D771
observation, templates based on Monte Carlo calculations (*e.g.*, Grebenev &
Sunyaev 1989) that are dominated by the line and continuum flux from [57]Co at
and below 122 keV.

Figures 6.1a-d — Images of the SN 1987A region obtained during our four

observations. These images include all data in the 50-1600 keV range (77-

1600 keV range during the D771 flight) combined optimally using a $\gamma=1$

power law template (see Chapter 5). These images are calibrated in units

of statistical significance, with the lowest contour at 2σ and subsequent

contours at 1σ intervals.

The scale of the images is the same in all cases. The frame is marked in

degrees of arc, meridians are every 10° of right ascension, parallels every

5° of declination. All coordinates are precessed to the epoch of the

observation. The larger size of the image in Figure 6.1a is due to the larger

size of the fully-coded field of view (shown by the circle) of Configuration

I.
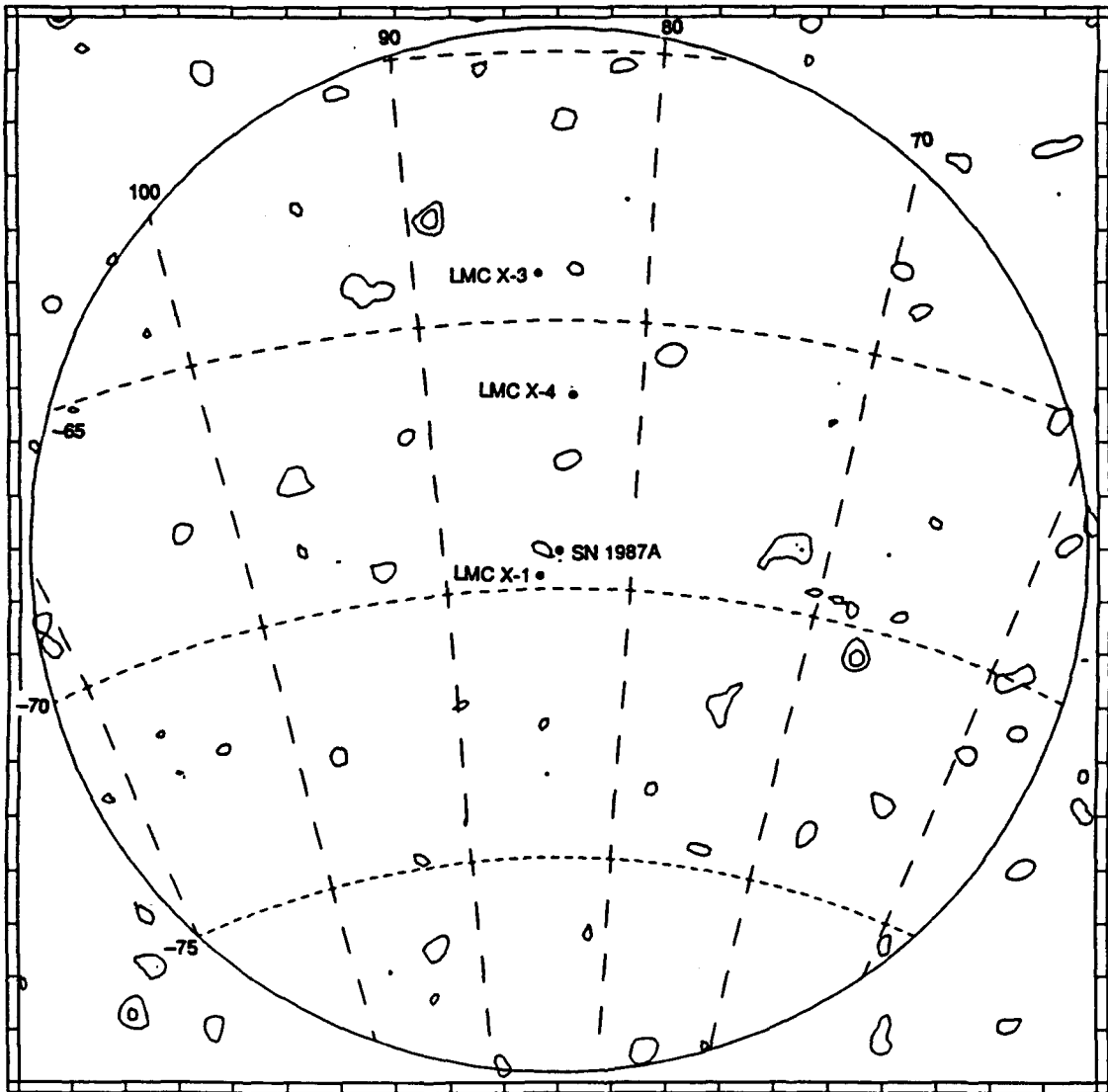
Figure 6.1a — Image from D86
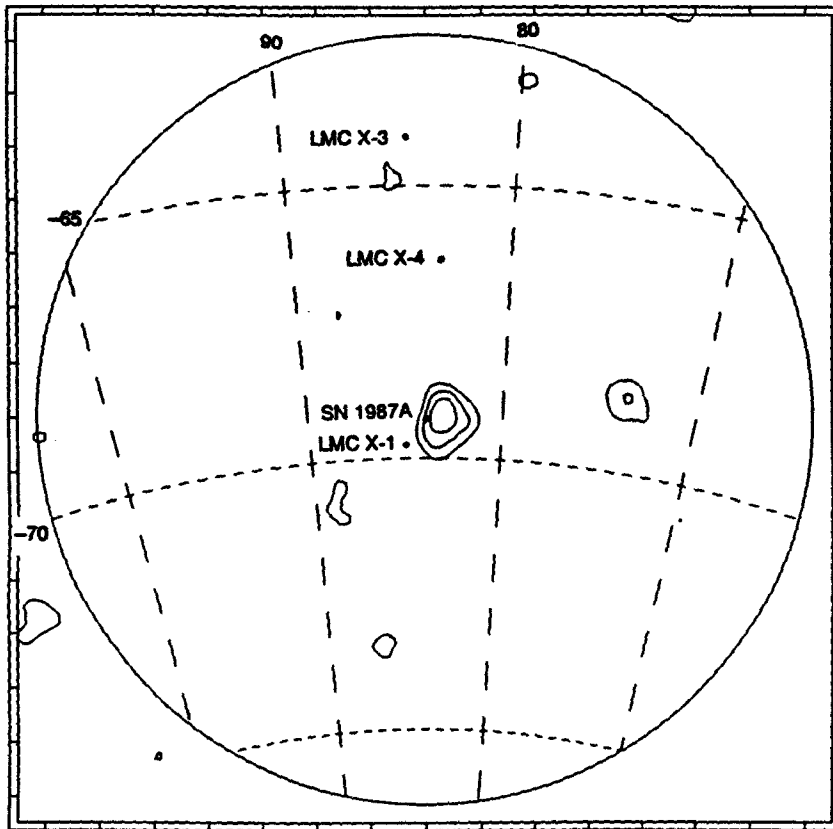
Figure 6.1b — Image from D268
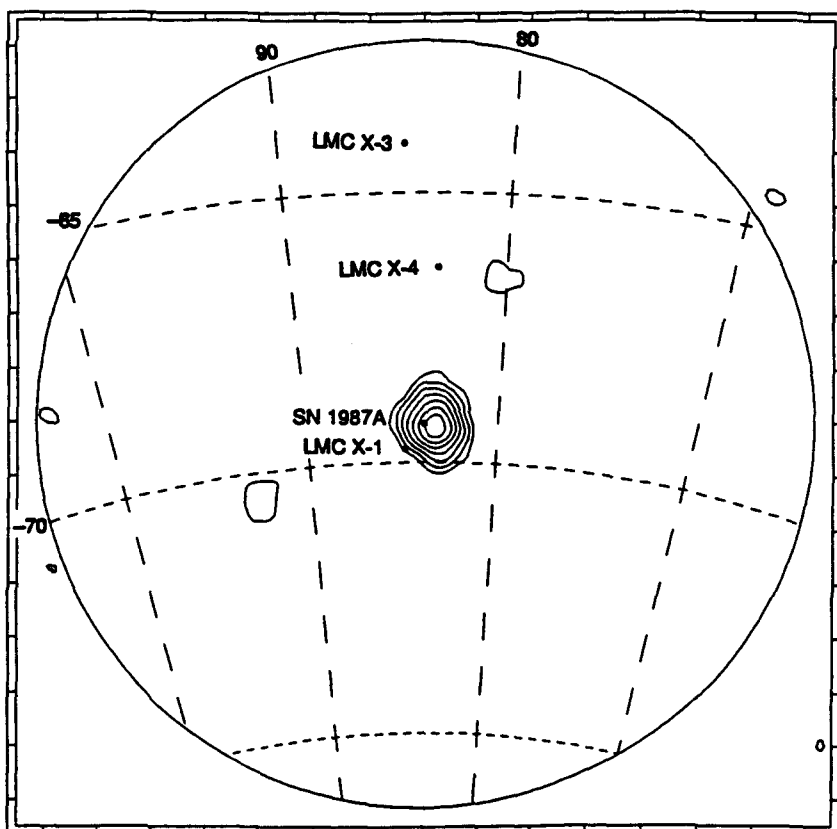
Figure 6.1c — Image from D414
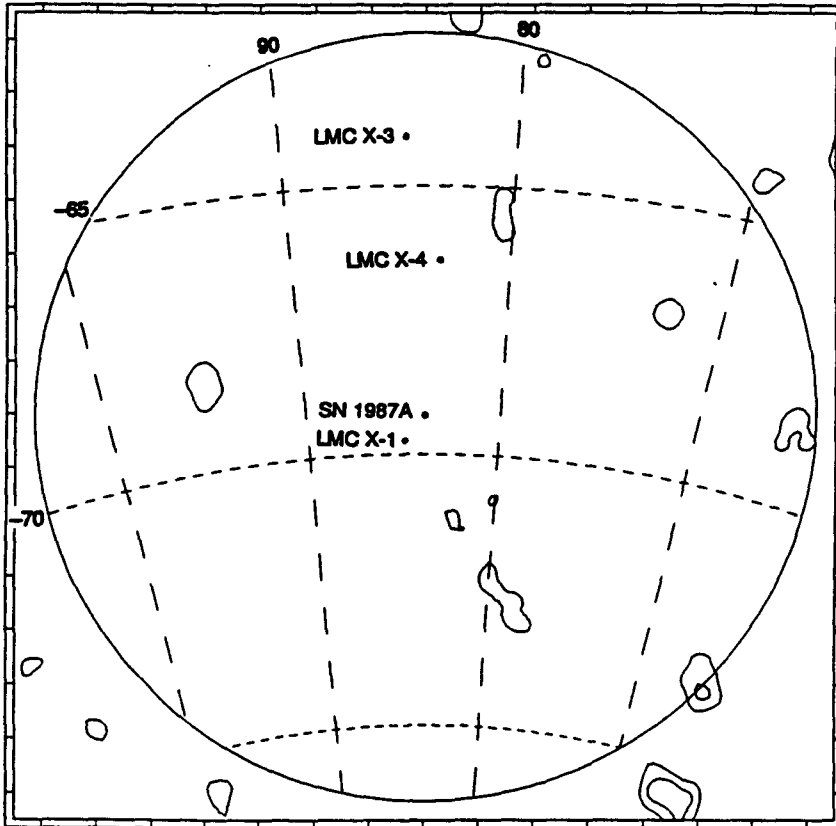
Figure 6.1d — Image from D771

The $\vec{\Delta}_{tot}$ displacements for the D268 and D414 observations are (0.3°, 0.0°) and (0.2°, -0.1°) respectively. (The coordinate system is right-handed and orthonormal, using degrees of arc in the negative right ascension and positive declination directions, corresponding to rightwards and upwards on the images.) Variation of the template γ in the range of 0 to 3 causes the peak to move by less than the 0.1° pixel size of the image reconstruction. The measured peak positions, $\vec{x}_{obs}$ are used in our flux determination.

6.2   Pointing Error Effects

The lengths of these displacements, Δ_{tot} (0.3° for D268 and 0.2° for D414) are inconsistent with the expected statistical error (σ_{stat}=0.09° and 0.05°) at the 99% confidence level. This implies a pointing error and requires additional analysis to bound the results of this, both in the flux determination and in source identification. As shown below and in Appendix B, the pointing error does not significantly affect the flux determination, and the source of the flux is SN 1987A rather than any other known source.

6.2.1   Sensitivity Reduction

Pointing errors may reduce the estimated flux, due to the resulting differences in $\vec{x}_{actual,i}$ for each pointing, i, during the observation. The summation of data from time periods with different pointing errors may smear out the combined peak, producing a reduction in sensitivity for each pointing proportional to $(\vec{\Delta}_{actual,i} - \vec{\Delta}_{tot})^2$. This is discussed in Appendix B, and is found not to be a significant source of error, with an upper limit of 4% for the D414 observation.

6.2.2   Source Confusion

The effects of the pointing error must also be examined to verify that the source being measured is, in fact, SN 1987A. To do this, other sources near SN 1987A must be eliminated as candidates. Once the peak is identified with a specific source, the effect of other sources nearby may be limited by the shape of the point spread function.

In August 1987, TTM (a coded-aperture telescope on the *Mir* space station with 1.8 arc min resolution and a 2-32 keV energy range) imaged the region of the sky containing SN 1987A (Sunyaev *et al.* 1987). In a 2° square centered on the position of SN 1987A there were only two visible sources: LMC X-1 and SNR0540-693. I will assume that these are the only two sources with potential for causing source confusion problems in our observations.

The source LMC X-1 is 0.6° away from SN 1987A and is known to have time-variable hard X-ray emission (Dotani *et al.* 1987). This source provides the most potential for contamination, and special care must be taken to bound its effect on the SN 1987A data (Dotani *et al.* 1987; Sunyaev *et al.*1987). In Appendix B I find that LMC X-1 is not the dominant source contributing to the image peak, with extremely conservative upper limits of 36% and 27% for D268 and D414, respectively.

Another potential source of contamination, the supernova remnant and 50 ms pulsar SNR 0540-693, is much less likely to affect our data. Although it is only 0.4° from SN 1987A, its spectrum of 6×10^{-3} (E/1 keV)$^{-1.8}$ photons cm^{-2} keV^{-1} (Sunyaev *et al.* 1987) is inconsistent with the source we measure. This spectrum was measured by the *Einstein Observatory* over the energy range of 0.6-4.5 keV (Clark *et al.* 1982), and was later found to be consistent with the measured optical

and infrared luminosities, (Chahan, Helfand & Reynolds 1984). The TTM
measurements in the energy range 2-32 keV in August 1987 (Sunyaev *et al.* 1987)
agree with this spectrum. By analogy with the Crab Nebula and Pulsar, which
this source closely resembles (*e.g.*, Seward, Harnden & Helfand 1984), the power-
law spectrum is expected to continue through the hard X-ray band encompassing
our measurements and to be reasonably constant with time.

In contrast, the measured flux of the source we detect is an order of
magnitude above the extrapolated SNR0540-693 spectrum at 50 keV during our
D268 and D414 observations, has a much harder spectrum, and is variable. For
these reasons, it is unlikely that the source we observe is SNR0540-693.

With LMC X-1 and SNR0540-693 excluded for the reasons given above,
and with no other candidate sources detected by the TTM measurements, it is
reasonable to conclude that the source we have detected and measured is
SN 1987A.

6.2.3   Pointing Error Effects: Conclusions

I developed a procedure to bound the effects of pointing errors, assuming
that the uncorrected pointing error for each pointing period was a constant
azimuthal offset. A description of this procedure as applied to the SN 1987A
observations is given in Appendix B. The conclusions are as follows:

a) The pointing errors do not smear out the image peaks enough to
significantly reduce the sensitivity of the measurements.

b) For the two observations that yielded positive detections of a source in
the field of view, LMC X-1 was certainly (D414), or probably (D268),
eliminated as the primary source of flux.

c) The data is consistent with SN 1987A being the only significant point source of flux near to its location.

d) If there is any flux from LMC X-1 its contribution to the image at the location of the image peak is minor.

Therefore, for this thesis, the results presented will be based on images made using the nominal pointing offsets (given in Tables C.1a-d in Appendix C). The image values from which the fluxes are derived are those measured at the peak locations of the γ=1 composite images shown in Figure 6.1b,c for the observations that yield significant detections ($\vec{x}_{meas} = \vec{x}_{obs}$ for the D268 and D414 observations), and at the nominal positions for the other observations ($\vec{x}_{meas} = \vec{x}_{nom}$(SN 1987A) for the D86 and D771 observations).

6.3 Continuum Fluxes

To derived continuum fluxes from our data in both wide and narrow energy ranges, I first (χ^2) fit a power-law spectrum to the data over a wide energy range (50-800 keV), then used the power-law as a template to calculate the flux in narrower energy bins within this range.

The images that supplied the values used in these analyses were finely binned in both time and energy. The time bins were the ~1 hour "pointings" listed in Tables C.1a-d in Appendix C. The energy bins for the images were narrower (<10 keV at energies below a few hundred keV) than the energy resolution of the detector, and much narrower than the energy bins for which the results are reported.

6.3.1   Continuum Power-law Fit

For each observation, the image values at $\mathcal{I}_{meas}$ for measured energies in the range 50 to 800 keV were fit to a power-law spectrum of the form $dN/dE = \kappa(E/100 \text{ keV})^{-\gamma}$. As mentioned in Chapter 5, this form was chosen because it approximates the results of a wide variety of Monte Carlo models, at the times (the D268 and D414 observations) when those models predict that the SN 1987A flux would be visible.

For the D268 and D414 observations, both the spectral index (γ) and the normalization (κ) were allowed to vary, with κ and γ chosen to minimize χ^2. The stated uncertainties were obtained from the variation in each parameter that results in a unity increase in χ^2, as minimized with respect to the other parameter. This method does not result in a joint probability of 68% ('1σ') that both parameters are within the stated ranges (see Lampton, Margon & Bowyer 1976 for a description of how such a region may be generated). Rather, it gives a confidence interval for each parameter individually. This single-parameter confidence interval for γ is appropriate for choosing a template, as the

Observation	Spectral Index γ	κ_{100} Flux at 100 keV (10^{-5} cm^{-2} s^{-1} keV^{-1})
D86	1	<2.0
D268	1.3±0.4	3.4±1.1
D414	0.97±0.17	3.3±0.6
D771	1	<1.6

Table 6.1 — Measured spectral parameters for SN 1987A continuum flux from 50-800 keV, including upper limits at the 95% confidence level (calculated by the method of §5.4).

normalization parameter is determined independently for each energy bin.

For the D86 and D771 observations, the spectral index was fixed at $\gamma=1$ so that upper limits could be calculated.

The results of these power-law fits are shown in Table 6.1 for the four supernova observations.

As described earlier, the upper limits for the D86 and D771 observations are based on $\vec{x}_{meas} = \vec{x}_{nom}$. More conservative upper limits may be obtained from the peak local to $\vec{x}_{nom}$. Such a procedure, however, has no significant effect on the results, increasing the upper limits for D86 and D771 by only 15% and 3%, respectively.

6.3.2   Continuum Fluxes Over Narrow Energy Bins

These power-law fits provide templates for further measurement of the continuum flux in narrower energy bins. As described in §5.3.6, the template used for this is the fitted power-law ($\gamma=1.0$ for D86, D414 and D771, $\gamma=1.3$ for D268) from 50 to 800 keV, and a flat, $\gamma=0$, spectrum above 800 keV. The results of this analysis are shown in Table 6.2.

The D268 and D414 fluxes are not corrected for the bias resulting from the selection of $\vec{x}_{meas} = \vec{x}_{obs}$. As mentioned in Appendix A, the fractional positive bias is η^{-2}, where η is the statistical significance of the peak from which $\vec{x}_{obs}$ is obtained, (4.9 for D268 and 8.9 for D414). The resulting biases, +4.2% and +1.3% respectively, are well below the statistical errors of the measurements.

Energy Bin (keV)			Flux At Nominal Energy (10^{-5} cm^{-2} s^{-1} keV^{-1})			
Min.	Nom.	Max.	D86	D268	D414	D771
50	75	100	<9.11	6.04±2.47	3.02±1.48	<6.05[a]
100	135	175	<2.99	2.23±0.86	2.78±0.48	<1.89
175	225	300	<1.29	1.04±0.61	1.64±0.35	<0.69
300	425	550	<0.61	0.35±0.40	0.74±0.23	<0.84
550	650	811	<0.49	0.55±0.38	0.40±0.20	<1.05
811	847	883	<0.89	1.53±0.75	1.24±0.38	<1.43
883	1050	1190	<0.40	0.60±0.37	0.06±0.19	<0.76
1190	1238	1286	<0.71	1.15±0.65	0.08±0.32	<0.64
1286	1450	1600	<0.70	0.34±0.42	0.13±0.21	<0.71
1600	2500	3500	<0.09	0.03±0.10	0.06±0.05	<0.20
3500	5000	10000	<0.02	-0.05±0.05[b]	0.00±0.02	<0.08

[a]Low energy range for D771 is 77-100 keV. See §2.

[b]Physically unreasonable negative flux is included for consistency. The corresponding 95% upper limit is 0.07 ($\times 10^{-5}$ cm^{-2} s^{-1} keV^{-1})

Table 6.2 — Continuum fluxes for SN 1987A. Upper limits are at the 95% confidence level.

The measured-energy bins chosen, with the exception of the narrow bins at 847 and 1238 keV, are wide ($\geq 8\sigma$) compared to the energy resolution of the detector. This limits the contribution from photons with energies outside the bin to $\leq 10\%$ of the flux, as calculated from the template.

The nominal energies for the bins are chosen by the "bow tie" method described in Chapter 5 to reduce the sensitivity of the result to the template. In all cases, a unity change in the template's γ results in a change in the measured flux at the nominal energy of $<0.25\sigma$, and in the upper limits of $<25\%$. The typical (rms) sensitivity to a unity change in γ is 11% for the bins below 800 keV and 5% above 800 keV. The magnitude and sign of the sensitivity varies among observations and energy bins, primarily due to the statistics-dominated distribution of counts within the bin.

The fluxes from Table 6.2 for the D268 and D414 observations are shown in Figures 6.2a and 6.2b. They are plotted as differential energy flux (differential photon number flux times energy) to compress the vertical scale for greater clarity. A $\gamma=1$ spectrum would appear on these plots as a horizontal line.

Also shown in these figures are the fitted power-law spectra from Table 6.1, and fluxes predicted by the 10HMM (provided by Pinto, 1990, private communication) and S90 models.

6.4 Line Fluxes

Although high-resolution detectors tend to be more sensitive to narrow lines than scintillators for a given effective area and background level, GRIP's large area and immunity from many sources of systematic errors results in useful line flux measurements.

Figures 6.2a-b — Our measurements of the continuum flux of SN 1987A from the

> D268 and D414 observations (diamonds). The vertical scale is differential
>
> energy flux (differential number flux multiplied by energy); a $\gamma=1$ power-
>
> law spectrum would result in a horizontal line on the plot.

> The solid curve is our best power-law fit to the data from 50-800 keV,
>
> given in Table 6.1. The upper (dotted) and lower (dashed) stepped lines
>
> are the fluxes predicted by Models 10HMM (Pinto & Woosley 1988; Pinto,
>
> *private communication*) and S90 (Sunyaev *et al.* 1990) respectively,
>
> convolved with our instrument resolution and averaged over the energy
>
> bins.

SN 1987A Flux on Day 268

GRIP Measurements
Best-fit Power Law
10HMM model
S90 Model

Flux x Energy (x10^{-3} keV cm^{-2} s^{-1} keV^{-1})

Energy (keV)

SN 1987A Flux on Day 414

Flux x Energy ($\times 10^{-3}$ keV cm^{-2} s^{-1} keV^{-1})

Energy (keV)

- ● GRIP Measurements
- —— Best-fit Power Law
- ········ 10HMM model
- ----- S90 Model

25

20

15

10

5

0

100

1000
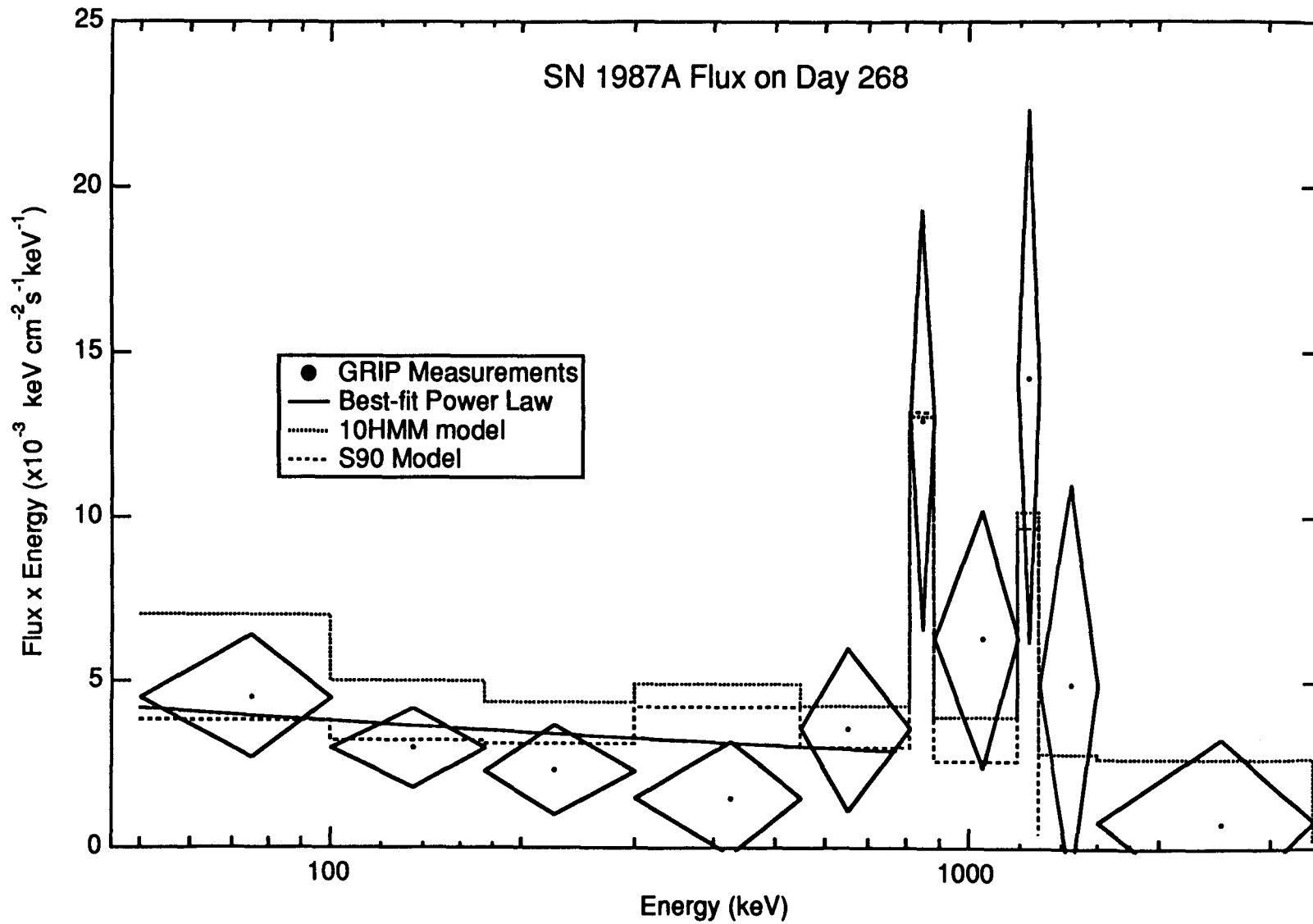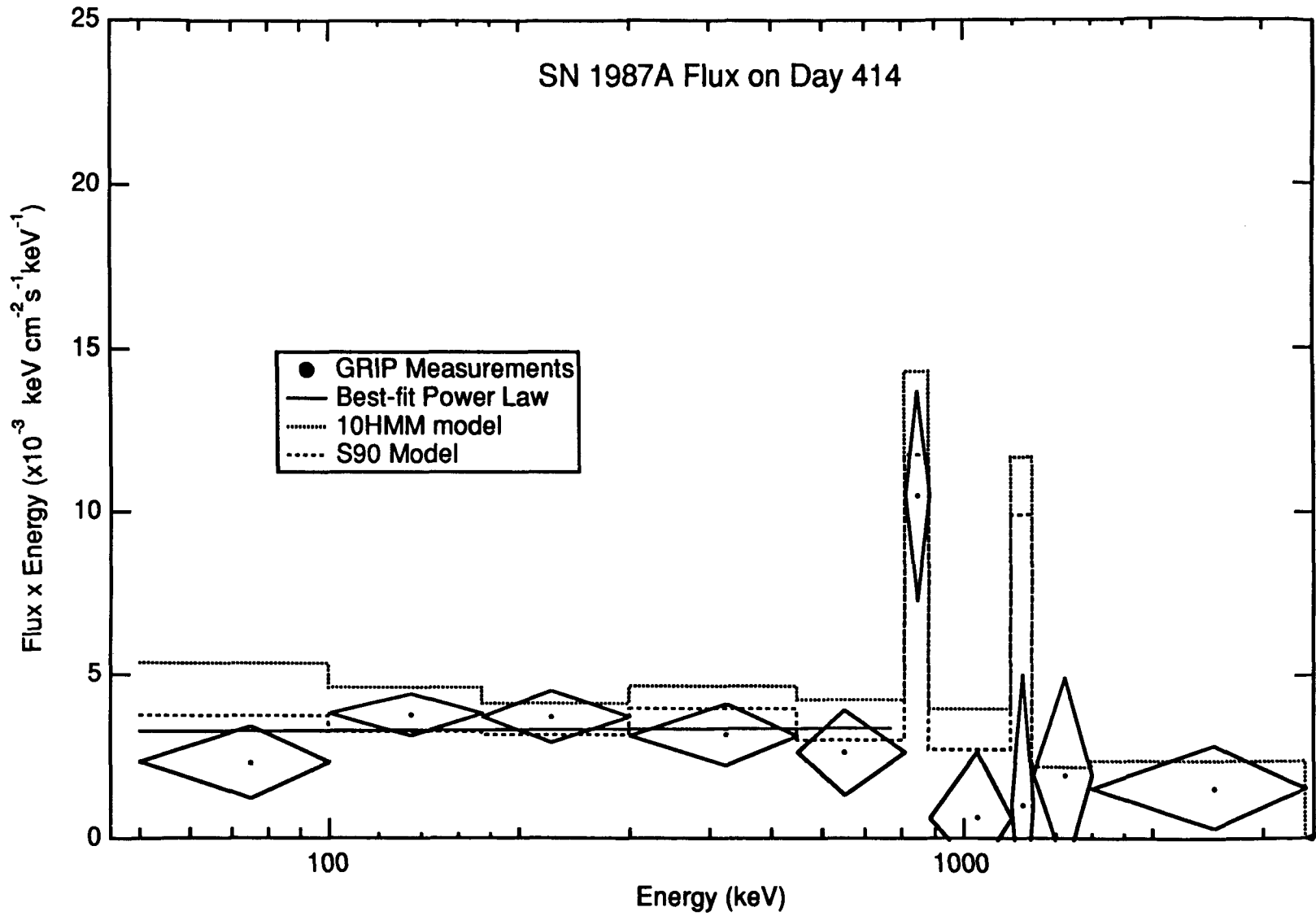
For the results shown in Table 6.2 and Figures 6.2a and 6.2b, the bins containing the 847 and 1238 keV lines were chosen to maximize the significance of excess flux due to line emission, based on our measured instrumental energy resolution of 6.7% and 6.2% FWHM, respectively. However, in addition to the line flux, these measurements include a contribution from the continuum flux within the bin. Furthermore, measuring the line flux by measuring the flux in a bin containing the line (boxcar integration) does not yield optimal sensitivity. Model fitting provides a more accurate estimate of the actual line flux.

6.4.1   The Line Flux Model

The data with measured energy between 600 and 1750 keV were analyzed in narrow bins having widths less than 35% of the FWHM instrument energy resolution. χ^2 fitting then found the values of the parameters for a model which includes two lines (at 847 and 1238 keV) and, if required, a stepped power-law continuum.

The lines were represented by Gaussian profiles with widths based on the measured energy resolution of our instrument, corresponding to the assumption that the line width is narrow compared to the energy resolution of GRIP (*i.e.*, the spread in line-of-sight velocity for the ^{56}Co is $\leq 10^7$ m s^{-1}). This assumption has been verified by high-resolution γ-ray measurements (*e.g.*, Tueller *et al.* 1990) and by infrared measurements (*e.g.*, Spyromilio, Meikle & Allen 1990) which show maximum velocities for the iron-group elements of 3.9×10^6 m s^{-1}.

The continuum is represented by a $\gamma=1$ power-law, stepped at each line so that the continuum flux $f(E)$ is:

$$f(E) = \kappa_{800}\phi(E)(E/800 \text{ keV})^{-1}$$

$$\phi(E) = \begin{cases} 1 & E < 847 \\ 0.57 & 847 < E < 1238 \\ 0.28 & 1238 < E \end{cases}$$

where $\phi(E)$ is proportional to the sum of all theoretical line strengths above E (given in Table 2.1 in Chapter 2). For simplicity, lines between the 847 and 1238 keV lines are ignored, while lines above 1238 keV are grouped into a single line above 1750 keV. This representation of the continuum flux adequately approximates the continuum spectrum found in the Monte Carlo models discussed in Chapter 6 while requiring only one parameter—the normalization κ_{800}.

6.4.2   Line Flux Ratios

Two different models were used for the line strengths. Model A allowed the line strengths to vary independently, while Model B constrained the lines to be in the ^{56}Co natural branching ratio of 0.68 photons at 1238 keV for each 847 keV photon (Lederer & Shirley 1978). The results for Model A give our best estimate for the individual line strengths from SN 1987A. If the ^{56}Co lines escape from SN 1987A while retaining the natural branching ratio, Model B gives the best estimate of the strength of the line complex.

The ratio of the 1238 keV to 847 keV lines emitted by SN 1987A has been measured using the Gamma-Ray Spectrometer (GRS) aboard the *Solar Maximum Mission* (*SMM*) satellite (Leising & Share 1990). They obtain a ratio of $f(1238)/f(847) = 0.68\pm0.12$ for the line fluxes, averaged over the period 1987

August to 1988 May, in excellent agreement with the natural branching ratio of 0.68.

The degree to which the line ratio of the flux from SN 1987A differs from the natural branching ratio of ^{56}Co depends on the optical depth at which the emerging line flux is originally produced. The mean free path (MFP) for 1238 keV photons is 20% longer than it is for 847 keV photons, so one (1238 keV) attenuation length of material would attenuate the 847 keV photons by $e^{-1.2}$, while attenuating the 1238 keV photons by e^{-1}. This would shift the line ratio of ^{56}Co from the natural branching ratio of 0.68 to a value of 0.83. The sensitivity of our measurements is insufficient to distinguish between these two values.

6.4.3   The Fits

χ^2 fits were made to the data for Models A and B, both with and without the continuum. If the inclusion of the continuum in the model produces a reduction of χ^2 sufficient to satisfy the F-test (Bevington 1969), that is an indication that the continuum should be included in the fit. A similar test comparing the χ^2 values between Model A and Model B indicates whether the hypothesis that the lines are in the natural branching ratio must be rejected.

For the D86 and D771 observations, no significant flux was found in either line, nor was any found in the continuum. For the D268 and D414 observations, the χ^2 of the model drops significantly ($P_F < 5\%$ by the F-test) when the continuum is included in fits of the data to Model A or Model B, indicating that the data from these observations require the presence of a continuum flux. (More accurately, the F-test rejects the hypothesis that all of the measured flux between

energies of 600 and 1750 keV is in the form of lines at 847 and 1238 keV. However, the conclusion that the additional flux takes the form of a continuum is physically reasonable.)

The reduction in χ^2 between Model A and Model B is not significant ($P_F > 10\%$), which indicates that our data is consistent with the lines being in their natural branching ratio.

The results for both models are shown in Table 6.3. Standard errors are obtained through the $\chi^2 + 1$ method, and upper limits are at the 95% level.

Observation	Model	847 keV line flux (10^{-4} cm^{-2} s^{-1})	1238 keV line flux (10^{-4} cm^{-2} s^{-1})	κ_{800} Continuum at 800 keV (10^{-6} cm^{-2} s^{-1} keV^{-1})
D86	A	<7.8	<7.9	...
	B	<6.4	...	...
D268	A	5.3±6.1	13.2±7.0	7.3±3.2
	B	8.8±5.4	...	7.1±3.2
D414	A	6.8±3.2	-0.2±3.5 (<6.7)	3.9±1.7
	B	5.0±2.8	...	4.0±1.7
D771	A	<11.1	<7.3	...
	B	<7.5	...	...

Table 6.3 — Measured flux for the 847 and 1238 keV lines from SN 1987A. Upper limits are at the 95% confidence level. Model A allows independent line strengths, Model B constrains the $f(1238):f(847)$ ratio to the natural branching ratio of 0.68:1.

Chapter 7
Discussion

Our observations, and those of other groups, showed that Supernova 1987A began producing detectable γ-ray emission long before the time predicted by early, simple models.

This radiation is produced by the decay of ^{56}Co in the ejecta of the supernova, and emerges both directly and after scattering. This radioisotope is formed near the core during the explosion, and the early emission indicates that the central material had propagated outwards in the ejecta to shallower optical depths.

Our imaging observations also show that, at least at our observation times, SN 1987A was the dominant source of flux above 50 keV in its vicinity. This result, by eliminating a potential source of systematic error, increases the confidence which may be placed in measurements made using conventional, non-imaging, γ-ray instruments. In particular, we showed that the X-ray source LMC X-1, which is 0.6° away from SN 1987A, was not emitting significant hard X-ray flux at the time of our observations. This decreases the likelihood that the SN 1987A measurements made with low angular resolution instruments were significantly contaminated by this source.

While the sensitivity of our measurements is sufficient to draw some conclusions about SN 1987A, a more complete understanding is obtained from measurements made in all energy bands.

7.1   Simple Modelling

A fairly simple calculation can use our data to eliminate at least one model for the ^{56}Co distribution—the distribution that places all ^{56}Co at the same optical depth. More detailed models would require Monte Carlo simulations, a propagation model for photons in the ejecta, modelling of the composition of the envelope, detailed treatment of the expansion and geometry of the envelope, and other analysis beyond the scope of this thesis.

I present the single-depth model because it provides a simple example of the calculations required in more complicated models, not because it is physically likely. A single optical depth would result from a ^{56}Co distribution that is much more compact than the surrounding envelope. This distribution is ruled out by other observations, such as the infrared spectroscopy measurements, which show a broad (2700 km s^{-1} FWHM (Haas *et al.* 1990)) velocity distribution for cobalt and iron, implying a broad spatial distribution, and an equivalent calculation made using the SMM data (see Model 1 of Leising & Share 1990).

The calculation computes only the line fluxes, since they have the simplest behavior and may be treated analytically. Assuming unaccelerated homologous expansion of the ejecta, the column density between a sample of material and a point outside of the ejecta at a time t is proportional to t^{-2} (the density of the material decreases as t^{-3} as the geometric path length increases linearly with t).

For the case where all of the material is at a column density depth of x_0 at time t_0, the strength of line i is therefore equal to:

$$f(E_i, t) = f_0(E_i, t)e^{-\frac{x_0}{\lambda(E_i)}\left(\frac{t_0}{t}\right)^2},$$

where $f_0(E_i, t)$, as described in §2.3.4, is the strength that the line at energy E_i would have if the ejecta were perfectly transparent to γ-rays, based on the ^{56}Co quantity derived from SN 1987A's bolometric flux. $\lambda(E_i)$ is the MFP of the γ-ray in the material, as described in §2.3.1.

A constant of the model may be determined from the measured values:

$$\frac{x_0}{\lambda(E_i)}t_0^2 = -ln\left(\frac{f(E_i, t)}{f_0(E_i, t)}\right)t^2. \qquad 7.1.a$$

Using the results for model B from Table 6.3 and comparing to Equation 2.3.4.a:

$$f(847 \text{ keV}, 268 \text{ days}) = 8.8\pm5.4 \times10^{-4} \text{ cm}^{-2} \text{ s}^{-1}$$

$$= 1.6\pm1.0 \times10^{-2} f_0(847 \text{ keV}, 268 \text{ days})$$

$$f(847 \text{ keV}, 414 \text{ days}) = 5.0\pm2.8 \times10^{-4} \text{ cm}^{-2} \text{ s}^{-1}$$

$$= 3.4\pm1.9 \times10^{-2} f_0(847 \text{ keV}, 414 \text{ days})$$

we can obtain values for the right-hand-side of Equation 7.1.a, which would be consistent with each other if the data were in agreement with the single-depth model. With t expressed in days, the values are $3.0^{+0.6}_{-0.4}\times10^5$ for D268, and $5.8^{+1.4}_{-}$

0.8)$\times10^5$ for D414. The D86 and D771 upper limits do not supply significant additional constraints. A comparison of the D268 and D414 values rejects the single-depth model at the 99% confidence level.

This confirms the results of Leising & Share (1990), who rejected this model based on a similar calculation using long-term continuous observations with the instruments on *SMM*.

7.2 Comparison to Other Measurements and Models

As shown in §7.1, models more complicated than the single-depth model are required to explain the measurements made by our group and by others. A comparison of our measurements to the results of other observations, and to the models developed from them, allows a better understanding of the evolution and energetics of SN 1987A. A list of the experiments that have detected (or obtained interesting upper limits on) γ-ray flux from SN 1987A is given in Tables 7.1a-c. For completeness, X-ray instruments are included in Table 7.1d.

As described in Chapter 2, the first constraints on models for SN 1987A were the observational properties of the progenitor star, Sk -69 202, and the early UVOIR light curve of SN 1987A. Simple models based on these constraints predicted that there would be no γ-ray flux for almost a year. The early detections of X-ray and γ-ray flux from the supernova, including those from our D268 observations, triggered the development of new models. The second-generation models, such as 10HMM, predict the behavior of the supernova quite well, but the limited data available at the time of their creation made the distribution of ^{56}Co in the models somewhat arbitrary.

Third generation models were developed in response to the availability of γ-ray flux measurements from single instruments over the complete evolution period of the ^{56}Co flux emission. These models, specifically the Sunyaev *et al.* (1990) model I call S90, and the Leising & Share (1990) models LS2 and LS3, fit the γ-ray observations to the radial distribution of ^{56}Co, using a small number (5 for S90, 3 for LS2, and 2 for LS3) of adjustable parameters.

Instrument	Instrument type	Continuum (keV)	Lines (keV)	Observation Days	Reference
Caltech GRIP	Imaging NaI(Tl)	50–800	847, 1238	86, 268, 414, 771	This thesis
CfA EXITE	Imaging NaI(Tl)	(*ul predicted*)	—	806	Not yet analyzed
Cosmos 1870	NaI(Tl), Earth Occultation	—	847, 1238	152–310	Efremov *et al.* 1990
GRO/OSSE	Collimated NaI(Tl)	50-150 (*ul*)	122 (*ul*)	1613–1627	Leising, private communication
GRO/Comptel	Compton NaI(Tl)	1-30 MeV (*ul predicted*)	—	1613–1627	Not yet analyzed
MSFC	Collimated NaI(Tl)	20–700	—	249, 411	Fishman *et al.* 1990
Mir/HEXE	Collimated Phoswich NaI(Tl)/CsI(Na)	15–200	—	144–843	Sunyaev *et al.* 1990
Mir/Pulsar	Collimated Phoswich NaI(Tl)/CsI(Na)	50–600	—	170, 340	Sunyaev *et al.* 1990
SMM/GRS	NaI(Tl), Earth Occultation	—	847, 1238, 2599, 3250	<0–830 (continuous)	Leising *et al.* 1990
UCR	Compton NaI(Tl)	1–5 MeV	1238	416	Ait-Ouamer *et al.* 1990

Table 7.1a — Scintillator γ-ray instruments which have detected SN 1987A or obtained interesting upper limits. *ul* indicates that the measurements provided upper limits only.

Instrument	Instrument type	Continuum (keV)	Lines (keV)	Observation Days	Reference
GRAD	Collimated Ge	—	847, 1238, 2599	320	Rester *et al.* 1989
GRIS	Collimated Ge	—	847, 1238, 2599	433, 613	Tueller *et al.* 1990
JPL	Collimated Ge	250–600	847, 1238	286	Mahoney *et al.* 1988
Lockheed/ MSFC	Collimated Ge	—	847, 1238	95, 249	Sandie *et al.* 1988a, 1988b
UCSD	Collimated Ge	—	847, 1238, 122 *(ul)*	819	Matteson et al 1990

Table 7.1b — Germanium γ-ray instruments which have detected SN 1987A or obtained interesting upper limits. *ul* indicates that the measurements provided upper limits only.

Instrument	Instrument type	Continuum (keV)	Lines (keV)	Observation Days	Reference
ADFA/Case	Spark Chamber	50–500 MeV (*ul*)	—	55	Sood *et al.* 1988
Frascatti	Collimated MWPC	15–180	—	55, 407	Sood *et al.* 1988; Ubertini *et al.* 1989
GRO/EGRET	Spark Chamber	20 MeV-30 GeV (*predicted ul*)	—	1613–1627	none reported

Table 7.1c — Gas phase γ-ray instruments which have detected SN 1987A or obtained interesting upper limits. *ul* indicates that the measurements provided upper limits only.

Instrument	Instrument type	Continuum (keV)	Lines (keV)	Observation Days	Reference
Art-P	Coded aperture MWPC	4–15 (ul)	—	1185–1308	Grebenev et al. 1991
Aschenbach et al.	Grazing Mirror	0.2–2.1 (ul)	—	182	Aschenbach et al. 1987
Burrows et al.	Grazing Mirror	0.75–2 (ul)	—	264	Burrows et al. 1987
Ginga/LAC	Collimated MWPC	0.1–30	—	100–1500	Dotani et al. 1987; Inoue et al. 1991
Rosat	Grazing Mirror	0.3–2.4	—	1209–1351	Trümper et al. 1991
TTM	Coded aperture MWPC	1–30 (ul)	—	175	Sunyaev et al. 1987

Table 7.1d — X-ray instruments which have detected SN 1987A or obtained interesting upper limits. ul indicates

that the measurements provided upper limits only.

7.2.1 Continuum

Figures 6.2a and 6.2b show a comparison of our data to the results of the 10HMM and S90 Monte Carlo analyses. As these figures show, our measured continuum is a better fit to the predictions of the S90 model than to the predictions of the 10HMM model. A detailed comparison shows that, for these two flights, our continuum measurements are consistent with S90 at the 10% level, and approximately 30% below the predictions of 10HMM. Given that the 10HMM model was based on observations made before approximately day 300, the fit to our D414 observations is remarkably good. The close agreement between our measurements and S90 (which is based on observations made with the HEXE instrument through day 800) is less surprising, but confirms the utility of this model.

To compare the GRIP measurements with other observations and the models, the data was divided into three continuum bins. For each bin, I used the same methods as for Table 6.2 to calculate the flux at the nominal energy. For the other measurements, I converted the data published in the references in Tables 7.1 to the nominal energies using a $\gamma = 1$ power-law. These fluxes are shown in Figure 7.1.

Figure 7.1 — Measured and modelled continuum flux of SN 1987A as a function

of time in three energy bands.

Experimental data from other instruments are taken from the references in

Table 7.1 and adjusted to the nominal energies (100, 300 and 600 keV)

using a $\gamma=1$ power-law spectrum.

Upper limits are at the 95% confidence level for the D86 and D771 GRIP

measurements, and at the 3σ level for the day 55 Frascatti measurements.

Also shown are the predictions of Model 10HMM (dotted curve) and

Model S90 (dashed curve).
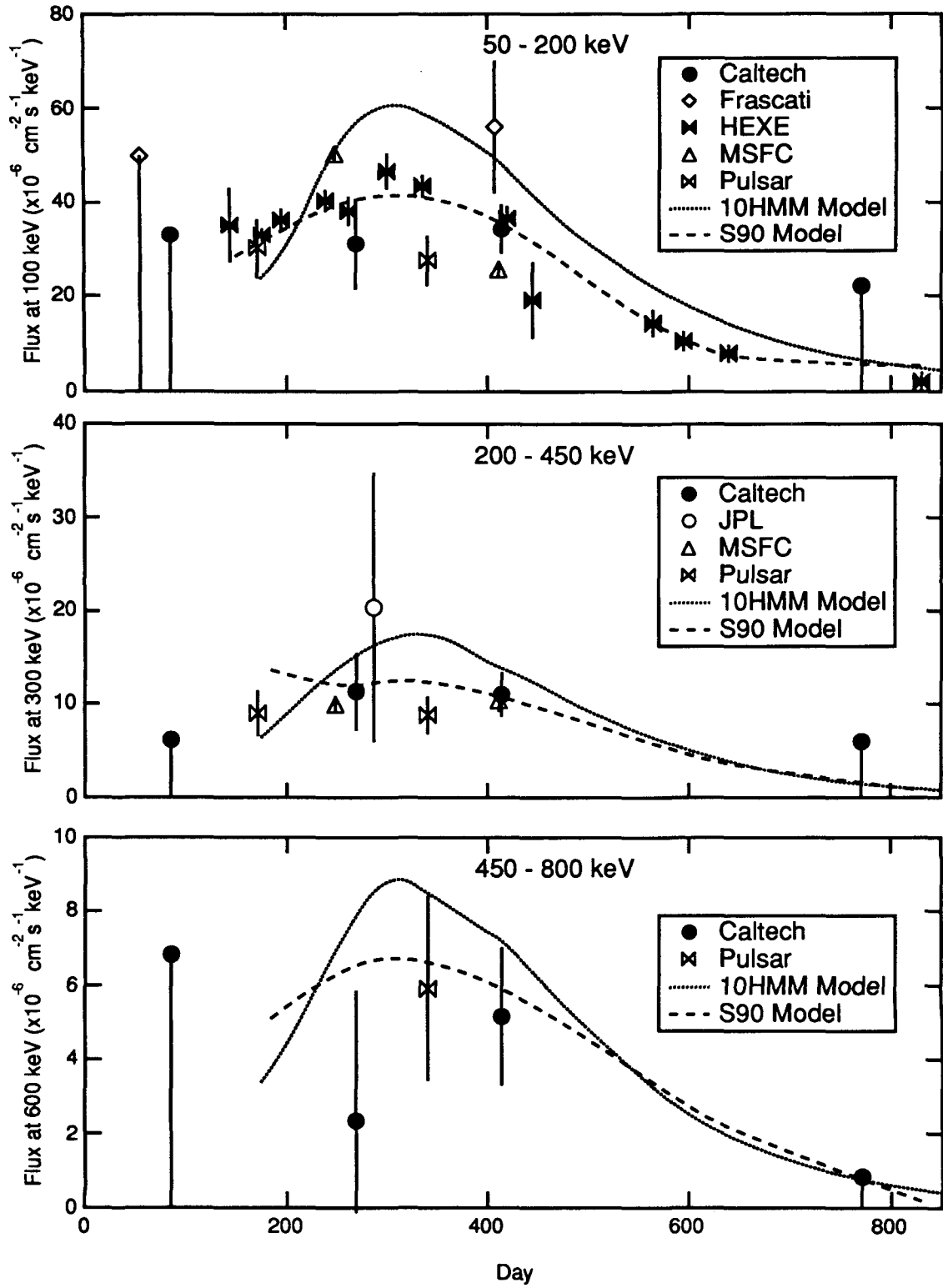
The HEXE measurements between 50 and 200 keV follow the S90 model curve very well, which is not surprising since they are the basis for the model. The other independent observations, including ours, also seem to prefer the S90 model to the predictions of the 10HMM model, although not overwhelmingly. There is no difference in the physics between these two models, merely a difference in the adjustable parameters that specify the ^{56}Co distribution and the extent to which they have been adjusted.

7.2.2   Lines

Our line fluxes are compared with model results and other measurements in Figures 7.2a-c, which show the 847 keV, 1238 keV, and combined (Model B) line flux values.

Figure 7.2a-c — 847 keV, 1238 keV and combined (Model B) line fluxes for

SN 1987A as a function of time. The predictions of models 10HMM

(dotted line) and LS3 (dashed line) are shown for comparison.

GRIP values are from Table 6.3, other values are from the references given

in Table 7.1. Upper limits are at the 95% confidence level (GRIP, SMM), 2σ

level (UCSD), or 3σ level (Lockheed/MSFC).

1238 keV Flux

Combined 847 and 1238 keV Flux

847 keV Equivalent Flux (cm^{-2} s^{-1})

Day

Legend:
- ● Caltech (GRIP)
- ⊞ Cosmos 1870
- ⋈ JPL
- ✕ GRAD
- ✖ GRIS
- ✗ Lockheed/MSFC
- ◇ SMM
- ▫ UCR
- ╱ UCSD
- ⋯ 10HMM model
- - - LS3 model
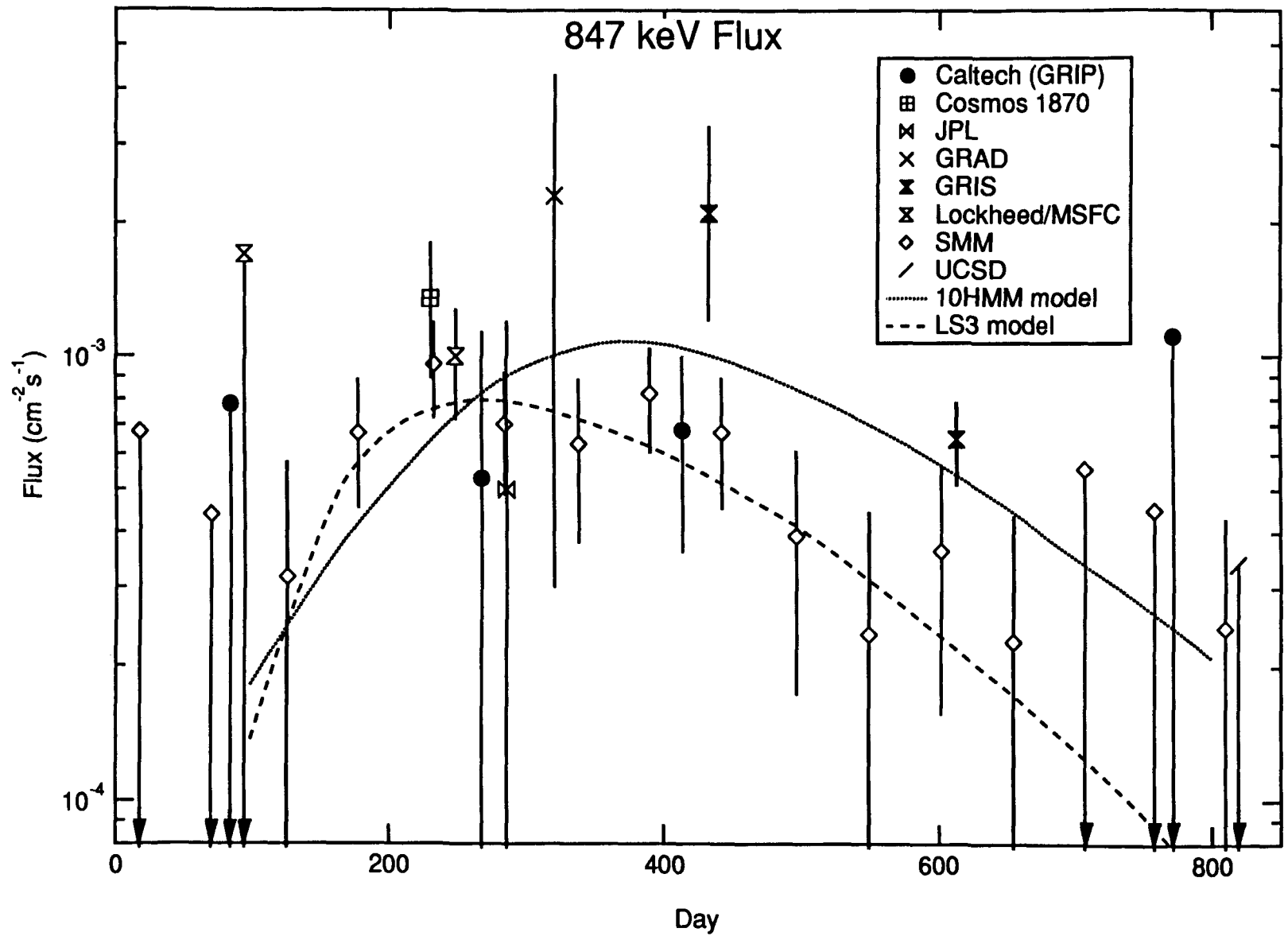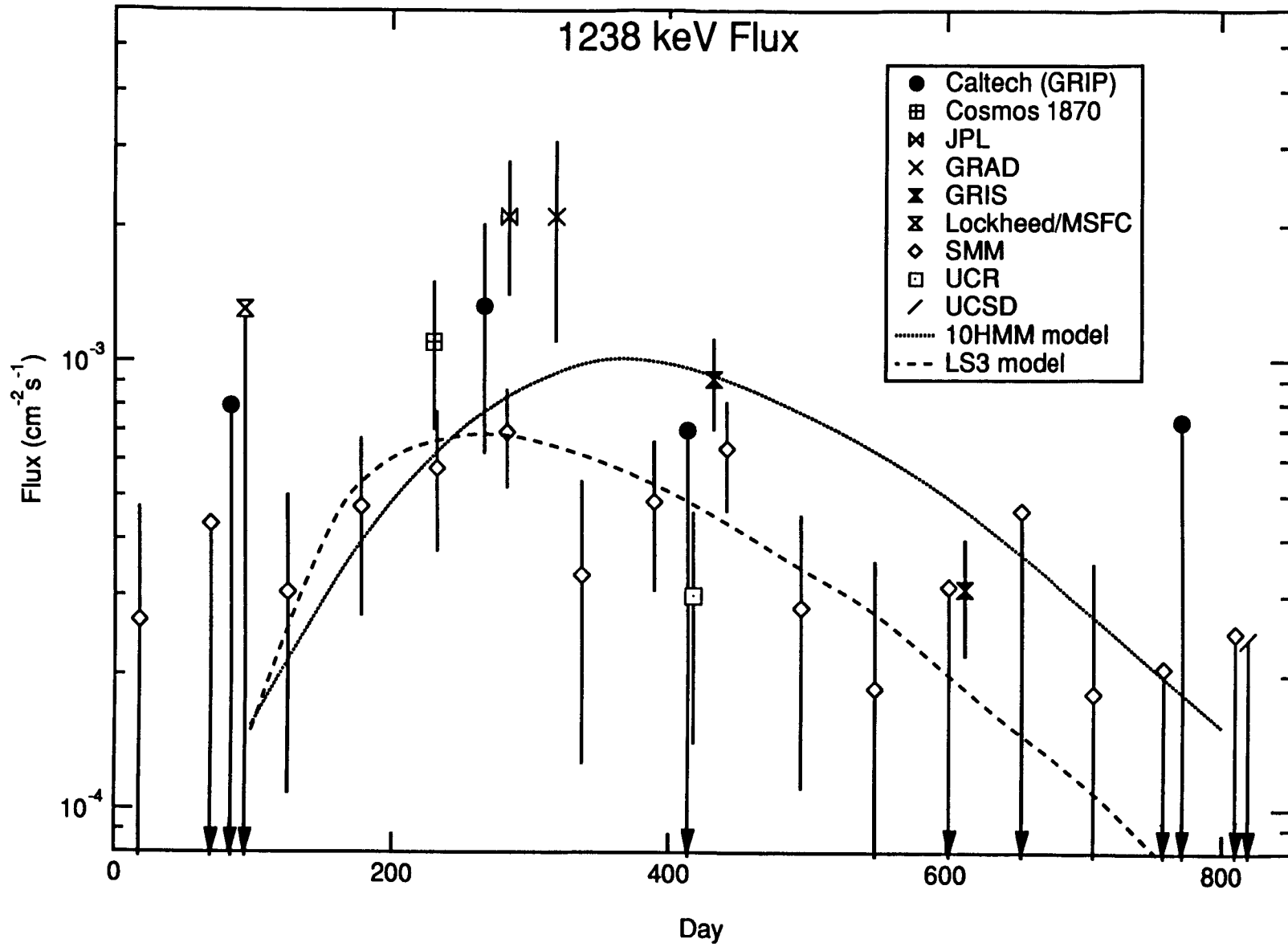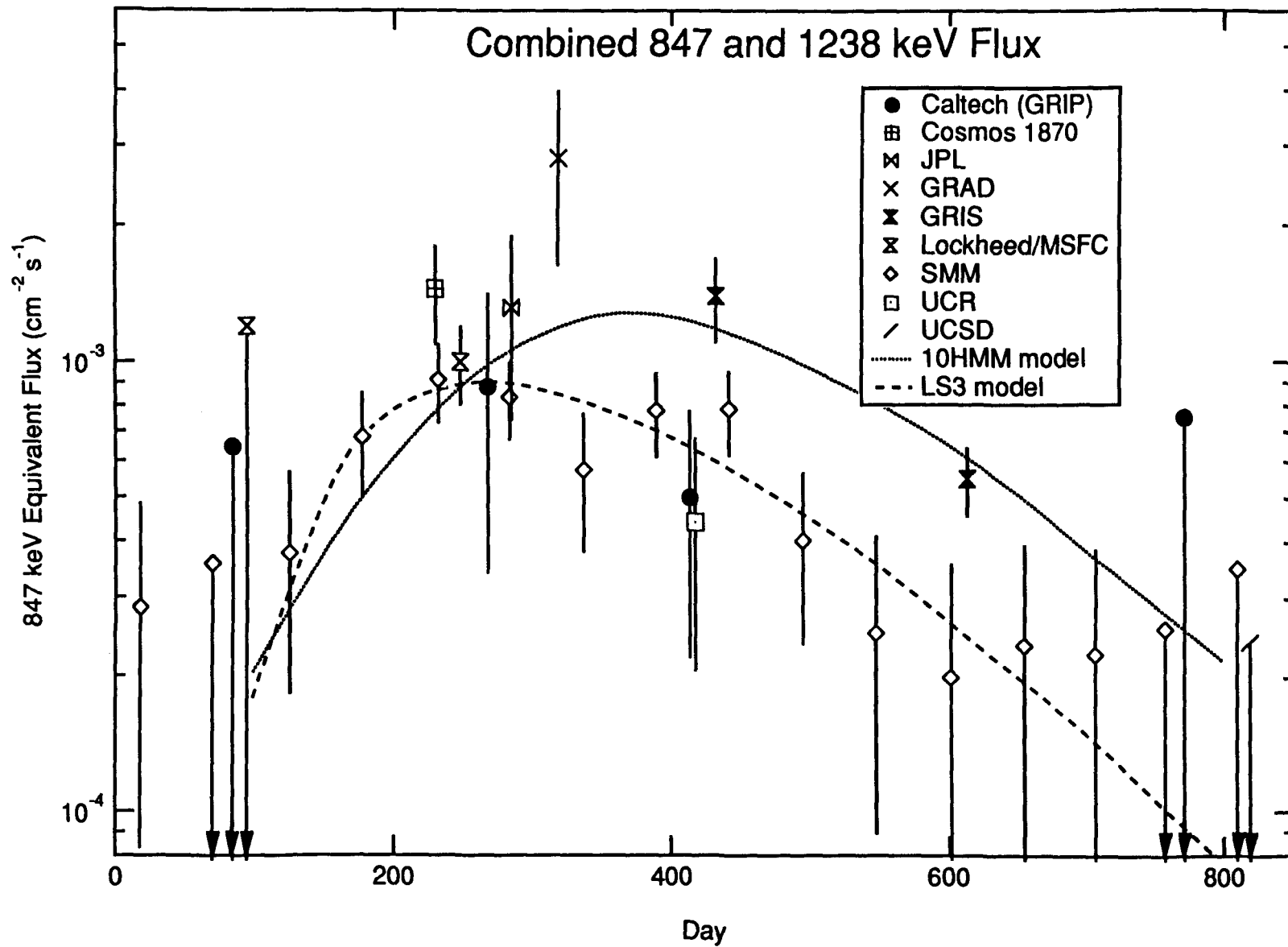
The data for other instruments are from the references in Table 7.1. In each observation that measured both 847 and 1238 keV lines, these measurements were consistent with the natural branching ratio (b_{1238}/b_{847}=0.68), allowing them to be plotted as combined fluxes on Figure 7.2c. The 10HMM and LS3 models are included on these plots. The S90 result (Sunyaev *et al.* 1990) falls between or near the 10HMM and LS3 models, and is omitted here for clarity.

A comparison of these measurements shows that our results are in agreement with those made by other instruments at similar times, including the high-resolution germanium detectors (GRIS, GRAD, UCSD, Lockheed/MSFC and JPL). It is also seen that, excluding the SMM data (the basis for the LS3 model), these line flux measurements do not strongly select either model to the exclusion of the other.

The models do make predictions about the widths and displacements of the γ-ray lines that can be tested using the data from high-resolution spectrometers. The GRIS measurements are inconsistent with the 10HMM model in both line width (at the 2.9σ level) and centroid energy (at the 4.9σ level) (Tueller *et al.* 1990). This does not mean, however, that the line widths and centroids would be more accurately fit by the LS3 model—the line shapes measured by GRIS require a velocity distribution that is inconsistent with any spherically symmetric model.

7.3 Photon and Energy Budgets

Our measurements can be used to estimate the fraction of γ-ray photons and the fraction of energy that escape from the supernova ejecta.

We have measured the line emission of SN 1987A at 847 and 1238 keV. Other lines, although they make up 30% and 40% of the original photon number and energy, respectively, are individually too weak for our instrument to detect. The fraction of photons that escape as continuum emission is harder to determine, since most instruments are not sensitive to the full range of continuum energies. Our continuum measurements are statistically significant only between 50 and 800 keV.

Measurements made of only the strong lines, and of continuum emission over a wide but incomplete energy range, may be extrapolated using models such as 10HMM. These models are used to predict the fraction of continuum flux that is emitted in the measured energy range, and this fraction is used to scale the measured flux. This procedure is then repeated for the lines, giving an estimate of the integrated γ-ray flux over all energies.

7.3.1 Results

Table 7.2 gives the continuum and line flux we measured from SN 1987A during each of our observations, and extrapolates these values to estimate the line and continuum flux over the entire energy spectrum. These are expressed both as photon and energy flux.

For example, on Day 414 we measured a flux of $9.3\pm2.0 \times10^{-3}$ photons cm^{-2} integrated over the energy range of 50-800 keV. According to Model 10HMM, 67% of the continuum photons emitted by SN 1987A at that time were in the 50-800 keV energy range, and so the extrapolated continuum flux is

$$\frac{1}{0.67}\times(9.3\pm2.0) = 14.0\pm2.9 \times10^{-3} \text{ photons cm}^{-2} \text{ s}^{-1}.$$

Measured And Extrapolated Fluxes								
	Measured Fluxes $(10^{-3}$ photons cm^{-2} s$^{-1})$ (keV cm^{-2} s^{-1})			**10HMM Corrections** (% of photons in measured range) (% of energy in measured range)		**Extrapolated Fluxes** $(10^{-3}$ photons cm^{-2} s$^{-1})$ (keV cm^{-2} s^{-1})		
Observation	Continuum	Line	Total	Continuum	Line	Continuum	Line	Total
D86	<5.5	<1.1	<6.6	46%[a]	31%[a]	<11.9	<3.5	<15.4
	<1.5	<1.1	<2.6	52%[a]	40%[a]	<2.9	<2.8	<5.7
D268	7.9±3.4	1.5±0.9	9.4±3.5	52%	34%	15.1±6.5	4.4±2.7	19.4±7.0
	1.8±1.3	1.5±0.9	3.3±1.6	44%	30%	4.0±2.8	5.0±3.1	9.0±4.2
D414	9.3±2.0	0.8±0.5	10.2±2.0	67%	49%	14.0±2.9	1.7±1.0	15.7±3.1
	2.6±0.7	0.8±0.5	3.4±0.8	51%	36%	5.1±1.3	2.4±1.3	7.4±1.9
D771	<4.3	<1.3	<5.6	78%	38%	<5.6	<3.3	<8.9
	<1.2	<1.3	<2.4	54%	42%	<2.2	<3.0	<5.2

[a]No fluxes are available for Model 10HMM for day 86. Corrections are based on values for Day 175

Table 7.2 — Photon and Energy fluxes from SN 1987A. Measured continuum and line fluxes are extrapolated using the results of Model 10HMM to approximate the total γ-ray flux from the supernova. Measured continuum is the integrated continuum between 50 and 800 keV, based on the numbers in Table 6.1. Measured line flux is the sum of the 847 and 1238 keV lines, based on the "Model B" numbers in Table 6.3.

These measured fluxes are extrapolated to the total γ-ray flux using the results of Model 10HMM. The "10HMM Corrections" columns list the fraction of the X-ray and γ-ray continuum flux contained in the 50-800 keV band, and the fraction of the line flux in the 847 and 1238 keV lines.

	Measured And Extrapolated γ-ray Fluxes							
	As a Percentage of ^{56}Co Production							
	Measured Fluxes (% of ^{56}Co photons) (% of ^{56}Co energy)			10HMM Corrections (% of photons in measured range) (% of energy in measured range)		Extrapolated Fluxes (% of ^{56}Co photons) (% of ^{56}Co energy)		
Observation	Continuum	Line	Total	Continuum	Line	Continuum	Line	Total
D86	<0.7 <0.1	<0.1 <0.1	<0.8 <0.2	46%[a] 52%[a]	31%[a] 40%[a]	<1.5 <0.3	<0.4 <0.3	<1.9 <0.6
D268	4.9±2.1 0.9±0.6	0.9±0.6 0.7±0.5	5.9±2.2 1.7±0.8	52% 44%	34% 30%	9.4±4.1 2.0±1.4	2.7±1.7 2.5±1.5	12.1±4.4 4.5±2.1
D414	21.7±4.6 4.8±1.3	2.0±1.1 1.6±0.9	23.7±4.7 6.4±1.5	67% 51%	49% 36%	32.5±6.8 9.5±2.5	4.0±2.2 4.4±2.5	36.5±7.2 13.9±3.5
D771	<248 <54	<72 <59	<320 <113	78% 54%	38% 42%	<321 <101	<192 <139	<513 <240

[a]No fluxes are available for Model 10HMM for day 86. Corrections are based on values for Day 175

Table 7.3 — Fluxes as in Table 7.2 expressed as a percentage of the number of photons and energy which would be produced by an initial mass of 0.075 M$_\odot$ of ^{56}Ni at a distance of 50 kpc.

Due to the possible existence of other sources in addition to the ^{56}Co, these percentages are not physically constrained to be less than 100%.

These photon and energy fluxes can be compared to the total produced by ^{56}Co to determine the fraction of energy and photons absorbed by the ejecta. Table 7.3 expresses the numbers in Table 7.2 as percentages of the values that would result if all γ-rays were to escape without interacting with the ejecta.

Assuming that all of the energy produced is emitted in the X-ray, γ-ray and UVOIR bands, the sum of UVOIR, X-ray, and γ-ray flux should follow an exponential decay law with a time constant of 111.26 days while the supernova is powered by ^{56}Co. The deficit of the UVOIR flux from this decay curve thus provides an indirect measure of the high energy flux. Figure 7.3 shows our measured and extrapolated γ-ray fluxes, the predicted γ-ray flux of model 10HMM, and the UVOIR flux deficit.

Most of these UVOIR measurements were made at Cerro Tololo Inter-American Observatory, (CTIO), European Southern Observatory (ESO), La Silla, and South African Astronomical Observatory (SAAO). UV observations were made with the *International Ultraviolet Explorer (IUE)*. IR observations in bands inaccessible to ground-based observatories were made using the *Kuiper Airborne Observatory (KAO)*.

The two techniques commonly used to measure the UVOIR flux from a source are called spectrophotometry and broadband photometry. In spectrophotometry, a spectrum is obtained using a quantitative detector, corrected for interstellar extinction and instrument response as a function of wavelength, and integrated. This gives the total energy flux over the measured range of wavelengths, which is then extrapolated to cover the wavelengths that

were not measured (*e.g.*, at wavelengths above and below the range of the instrument, and in absorption bands in Earth's atmosphere). In broadband photometry, the light from the source is measured over a series of broad (typically ~1000 Å) wavelength bands, selected using glass filters. From a set of broadband measurements over a large energy range, and from the wavelength responses of the filters and the photodetectors, a spectrum is estimated, extrapolated, and integrated.

Spectrophotometry produces a more reliable luminosity measurement than broadband photometry, however, it also requires either a brighter source or a longer observation time. For this reason, most luminosity measurements of SN 1987A were made using broadband techniques with relatively few spectrophotometric measurements. Unfortunately, broadband photometry is most appropriate for stellar spectra, which tend to be thermal with narrow absorption lines. The spectrum of SN 1987A during the exponential tail is a non-thermal continuum with strong emission lines, making the broadband results sensitive to the extrapolation techniques used and the details of the filter and photodetector responses. For example, the "I" (near infrared, roughly 7500-9000 Å) filters for CTIO and SAAO are of different widths, so that the SAAO "I" filter passes strong calcium lines in SN 1987A's spectrum which are blocked by the CTIO filter, causing a discrepancy of 0.4 magnitudes (~40%) in the I measurements (Hamuy *et al.* 1990). This is responsible for at least some of the discrepancies among the UVOIR deficit datasets shown in Figure 7.3.
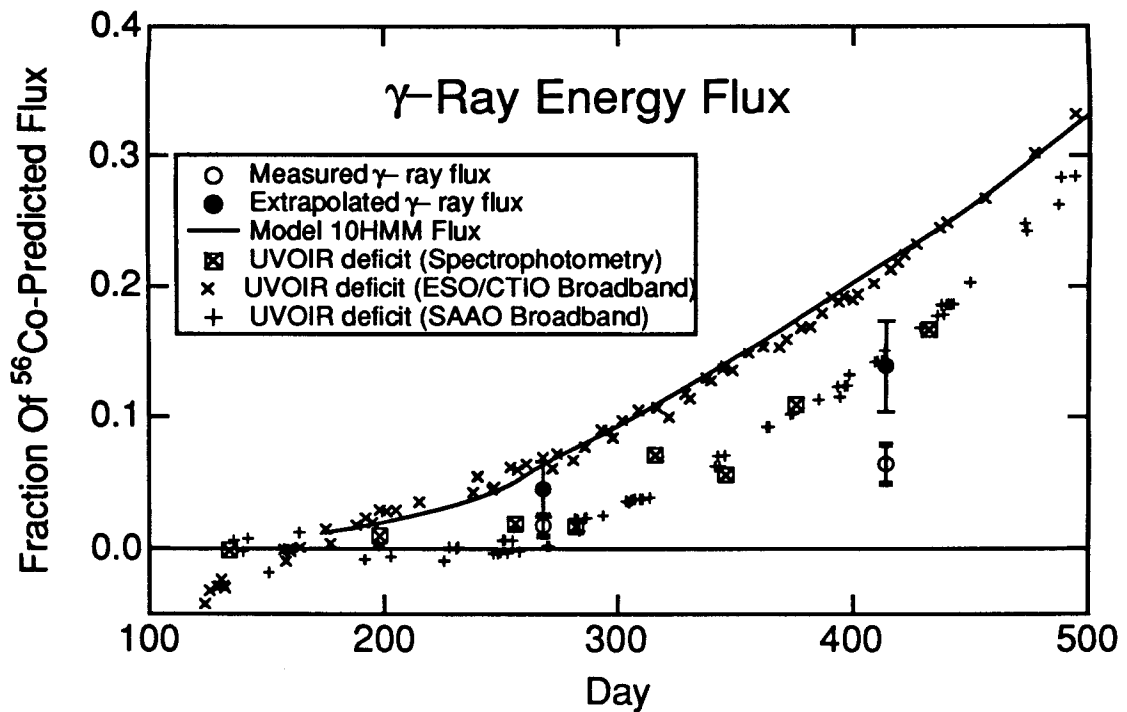
Figure 7.3 — Energy emitted as γ-rays and X-rays by SN 1987A as a fraction of the total energy produced by the ^{56}Co, compared to the 10HMM model predictions, and to deviations of the UVOIR luminosity from a pure exponential decay.

The GRIP measured and extrapolated γ-ray and X-ray flux are from Table 7.3. The curve is the γ-ray and X-ray flux predicted by model 10HMM.

The UVOIR deficits are based on spectrophotometry at ESO, La Silla, CTIO, and Kuiper Airborne Observatory (Bouchet *et al.* 1991), broadband photometry from CTIO and ESO (Suntzeff & Bouchet 1990), and broadband photometry from SAAO (Catchpole *et al.* 1987, 1988; Whitelock *et al.* 1988). For each dataset, the assumed initial mass of ^{56}Ni was adjusted assuming that the UVOIR luminosity was equal to the ^{56}Co energy production around day 160 (shortly after the transition of the luminosity curve from a steep decline to an exponential tail).

Within the systematic errors of the UVOIR luminosity measurements, the ^{56}Co energy production is totally accounted for by the sum of the UVOIR and extrapolated γ-ray and X-ray luminosities at the times of our measurements.

7.4   Future Measurements

Although the flux from ^{56}Co in SN 1987A has declined below the level detectable by our instrument, there are still measurements that can be made using other instruments.

7.4.1 ^{57}Co and Other Isotopes

After the ^{56}Co has decayed sufficiently (~800 days), ^{57}Co (produced initially as ^{57}Ni) is expected to dominate the γ-ray spectrum of SN 1987A. This second isotope has a longer half-life (271.80 days, *Nuclear Data Sheets* , (Burrows & Bhat 1986)) than ^{56}Co (77.12 days), and so, although it is produced in smaller quantities, it is expected to be the more common isotope a few years after the explosion.

Because the iron on Earth is believed to be the result of nucleosynthesis of nickel isotopes in supernovae prior to the time of the formation of the solar system (~5×10^9 years ago), the ratio of mass-57 to mass-56 isotopes is expected to be comparable to the ^{57}Fe:^{56}Fe = 0.024 abundance ratio for the Solar system (Anders & Grevesse 1989). This is only a rough estimate, however, because the iron in the solar system is presumably from multiple supernovae of different types and parameters, each having a different ratio. I will use the symbol R to

indicate the ratio of mass-57 to mass-56 isotopes in SN 1987A in terms of the

Solar system ratio:

$$R = \frac{^{57}Ni/^{56}Ni \text{ produced in SN 1987A}}{^{57}Fe/^{56}Fe \text{ in terrestial iron}}$$

where a larger R specifies a greater production of ^{57}Ni in SN 1987A.

Models of nucleosynthesis in SN 1987A predict that $0.5 \leq R \leq 2.5$ (Woosley
& Hoffman 1991). Production of ^{57}Co is sensitive to the neutron excess of the pre-
shock material, the dividing surface between material which is either ejected
from the supernova or falls back on the core, and the cooling rate as the material
drops from nuclear temperatures after the first seconds of the explosion. R
therefore provides information on the state of the material and the processes of
the explosion near the edge of the star's core, constraining theories of stellar
evolution and nuclear and particle physics.

The models which are used to predict the γ-ray flux from ^{56}Co are also
used to predict the flux from ^{57}Co (typically with the simplifying assumption
that the two, produced in the same region of the star, have the same spatial
distribution). The dominant γ-ray lines of ^{57}Co (122 keV and 137 keV) are more
heavily attenuated than the higher energy ^{56}Co lines, which increases the flux
sensitivity to attenuation in the ejecta. Comparing these model predictions to the
measured flux, the ^{57}Co ratio can be determined.

For $R \sim 1$, the ^{57}Co component is a significant fraction of the flux only for
our last (D771) observation. Our sensitivity at these low energies was such that
we obtained only an upper limit to ^{57}Co production of $R \leq 10$. The same method
has been used on the HEXE data to give an upper limit of $R \leq 1.5$ (Sunyaev et al.
1990). Observations by the OSSE instrument on the Compton Gamma-Ray

Observatory (GRO) place an upper limit of R<2.4 (Leising, 1992, private communication).

The UVOIR measurements indicate that the total luminosity of SN 1987A after day 700 is greater than that which would be produced by ^{56}Co alone (Bouchet *et al.* 1991; Suntzeff *et al.* 1991). Ascribing this excess to the decay of ^{57}Co gives a value of $R{\sim}5$ (Suntzeff *et al.* 1991), but there may be other sources of luminosity, such as an accreting central object (neutron star or black hole). Light echoes and radiation from dust heated by the supernova may also contribute to the measured luminosity. At late times, SN 1987A has cooled enough (to a temperature below 200 K at day 900, Bouchet *et al.* 1991) that it radiates predominantly in the infrared, with additional non-thermal emission complicating the spectrum, making estimates of its luminosity extremely difficult. Measurements made by different groups differ by as much as a factor of 2 (Suntzeff *et al.* 1991).

Study of the infrared spectrum has shown a decrease in the strength of cobalt lines relative to iron lines, which is interpreted as being due to the decay of Co isotopes to Fe isotopes. This change has slowed down with time, indicating that the remaining Co has a longer average half-life than it had before. The value derived from these measurements is $R{=}1.5{\pm}0.5$ (Varani *et al.* 1990).

^{44}Ti is another isotope that may be an important power and γ-ray (1.16 MeV) source in supernovae. The 47 year half-life of ^{44}Ti$\rightarrow^{44}$Ca allows it to outlast the ^{56}Co and ^{57}Co and become dominant after ${\sim}5$ years. Nuclear models constrain the ^{44}Ti production to less than twice the corresponding Solar-system isotope ratio (^{44}Ca/^{56}Fe = 0.00155 by number of atoms (Anders & Grevesse

1989)), and, as in the case of ^{57}Co, rapid cooling could result in much lower ^{44}Ti production—as little as 2% of the Solar-system ratio (Woosley & Hoffman 1991).

7.4.2   The Central Remnant

A core collapse supernova leaves behind a collapsed core. This compact object is probably in the form of either a neutron star or a black hole formed by further collapse of the neutron core sometime after the rebound. As the ejecta clears, and the radioisotopes decay away and no longer dominate the power budget, this object may become visible.

Periodic emission from the supernova remnant would demonstrate the presence of a neutron star pulsar. Many pulsar searches are currently underway in different regions of the spectrum, but no pulsed signal from SN 1987A has yet been found.

Other emission signatures could also indicate the fate of the remnant. Cyclotron lines, indicating a strong (~teragauss) magnetic field, would imply the existence of a neutron star, since black holes do not have intrinsic magnetic fields ("black holes have no hair") and do not produce such strong fields in their environment.

7.4.3   The Renaissance

As the ejecta from SN 1987A streams outwards at high speed, it will eventually encounter material in the circumstellar shell, believed to have been ejected from the progenitor star, Sk -69 202, during a red supergiant mass loss phase. When this occurs, approximately 15 years after the explosion (c. 2002), the supernova will increase its luminosity in each of UV, optical, radio, and X-ray emission to ~10^{38} erg s^{-1}, approximately the same total luminosity as it had

around day 850 (Luo & McCray 1991). This will provide the opportunity for further study and greater understanding of SN 1987A.

Chapter 8
Conclusions

SN 1987A provided the first opportunity to study a nearby supernova with modern instruments. In particular, it provided the first opportunity to study the γ-ray emission from a supernova and detect the signature of radio-isotopes produced in explosive nucleosynthesis.

We have detected line and continuum γ-rays from SN 1987A, emitted by ^{56}Co produced in the explosion. These measurements generally support the previously accepted model of core collapse supernovae, discussed in Chapter 2, while requiring some refinements which provide a better fit to all SN 1987A observations.

The major refinement to the core collapse model is the requirement for material formed near the collapsing core to propagate outwards and mix with material originating nearer to the surface of the star. The early emission and later behavior of γ-ray flux from SN 1987A indicate that this mixing has occurred to a previously unexpected degree. Measurements in other parts of the spectrum are also consistent with the mixing of ~0.07 $M_\odot$ of ^{56}Co in a ~15 $M_\odot$ envelope of ejecta.

Observations of SN 1987A showed that γ-ray emission is a significant fraction of the luminosity of supernovae. Our measurements, other γ-ray measurements, and models based on these, indicate that ~5% of the total luminosity of SN 1987A was emitted at X-ray and γ-ray energies by day 268, and that this fraction increases at later times. This emission must be considered to understand the energy balance of supernovae when analyzing UVOIR observations.

Appendix A
Coded Aperture Imaging

Coded aperture imaging was suggested independently by Dicke (1968) and Ables (1968) as a method of producing X-ray and γ-ray images at energies too high for lenses and mirrors to function. The use of Uniformly Redundant Arrays[1] (URAs) was suggested by Fenimore & Canon (1978) to produce higher-quality images than the previous random-pattern masks. Rotating Hexagonal URAs (HURAs) as are used on GRIP were developed at the California Institute of Technology by Cook *et al.* (1984). Caroli *et al.* (1987) provide a review of coded aperture imaging.

The generation of a source image using the GRIP coded-aperture instrument is described here in a mathematical context. A more complete treatment is found in Finger (1987). The specific details relating to the practical implementation of the method are not included in this thesis. Some of these details are found in Cook *et al.* (1988).

---

[1]"Uniformly Redundant" refers to the property that the autocorrelation function of the mask is constant away from the origin.

Figure A.1 — The vectors referred to in §A.1 (not to scale). A γ-ray coming from source j and interacting with the detector at the point $\vec{z}$ passes through the mask at point $\vec{z}+\vec{z}_j$. The center of the field of view is in the direction of the telescope axis.
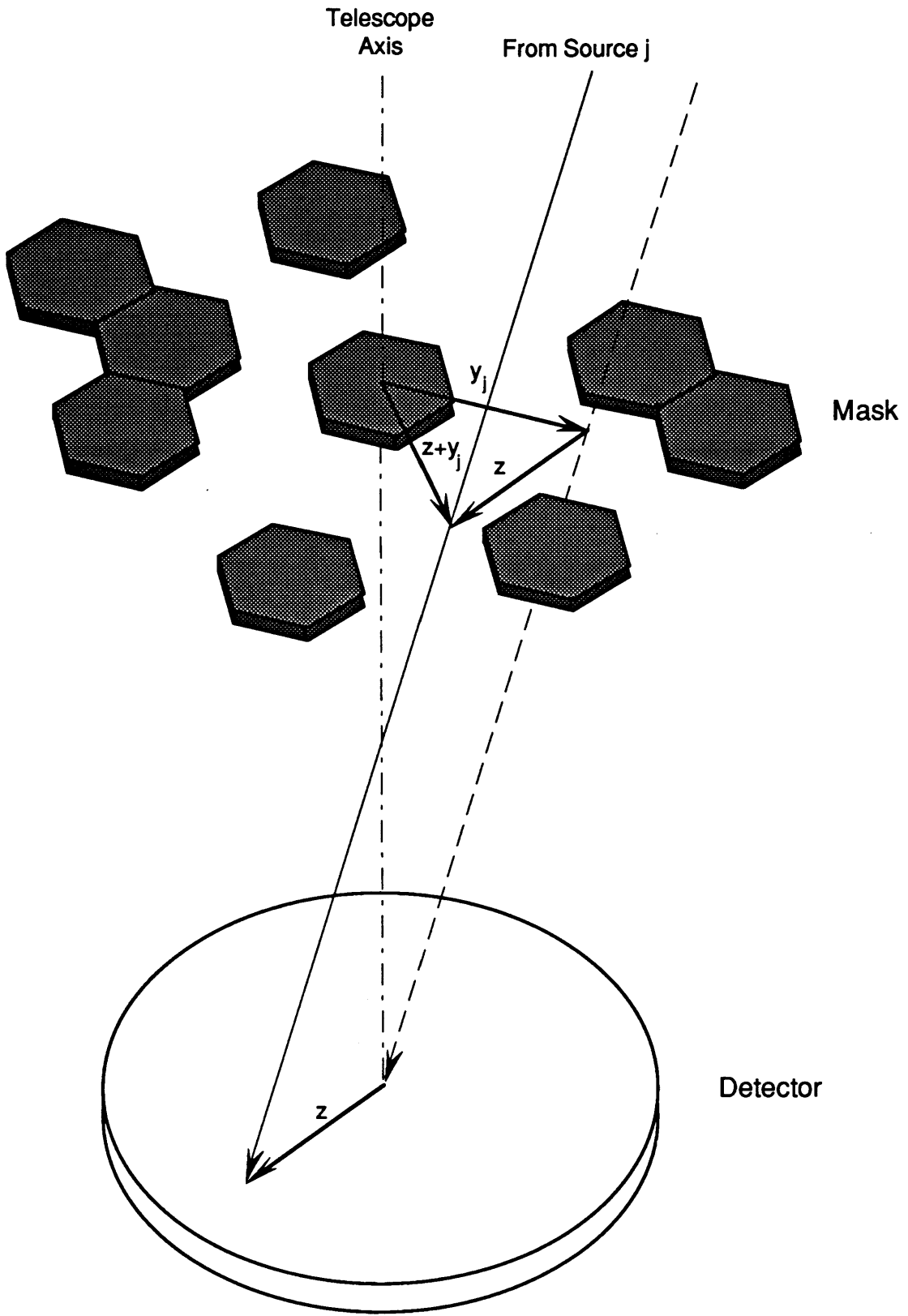
A.1   The Detected Event Distribution

Using the formalism of Finger (1987), the coded aperture mask is described by a function $M(\vec{y})$, where $\vec{y}$ is a 2-dimensional vector defining a location on the plane of the mask. $M(\vec{y})$ is unity if the mask is transparent at that point, and zero if it is opaque. The expected flux on the detector at a position $\vec{z}$, due to a point source, j, is proportional to a translated mask function:

$$\langle f_j(\vec{z}) \rangle = M(\vec{z} + \vec{y_j}) F_j,$$

where F_j is the intensity of the unmodulated source flux and $\vec{y_j}$ is the point at which a line between the source and the center of the detector ($\vec{z} = 0$) passes through the mask. (See Figure A.1).

The detector has a finite position resolution represented by the point spread function (PSF), $p(\vec{a})$, which gives the probability distribution of a detected photon's position error $\vec{a} = \vec{z}_{measured} - \vec{z}_{true}$. The detector also has a position-dependent background, $B(\vec{z})$. For the case of multiple point sources, j, in the field of view, the resulting expected distribution of detected photons is given by:

$$\langle D(\vec{z}) \rangle = \sum_j M^{eff}(\vec{z} + \vec{y_j}) F_j + B(\vec{z}),$$

where the effective mask function, M^{eff}, is the mask function convolved with the PSF:

$$M^{eff}(\vec{y}) = \int p(\vec{a}) M(\vec{y} - \vec{a}) d^2\vec{a}.$$

A.2   Background Subtraction

To eliminate the background term, measurements are made with a "mask-antimask" pair. These are pairs of mask patterns with all (or most) of the transparent and opaque cells interchanged:

$$M_+(\vec{y}) = 1 - M_-(\vec{y})$$

for all (or most) values of $\vec{y}$. $M_+(\vec{y})$ and $M_-(\vec{y})$ are the mask functions for the mask and antimask respectively.

Taking the difference between a single mask-antimask pair of measurements provides a measurement with no contribution from the position-dependent background:

$$\langle \Delta D(\vec{z}) \rangle = \langle D_+(\vec{z}) \rangle - \langle D_-(\vec{z}) \rangle$$
$$= \sum_j \Delta M^{eff}(\vec{z}+\vec{y_j})F_j,$$

where

$$\Delta M^{eff}(\vec{y}) = M^{eff}_+(\vec{y}) - M^{eff}_-(\vec{y}).$$

A.3   Image Reconstruction

The measured $\Delta D(\vec{z})$ (which has a contribution of either +1 or −1 for each event detected at $\vec{z}$ using the mask or the antimask) is converted into an image.

It is shown in Finger (1987) that, when imaging using a Uniformly Redundant Array (URA) mask pattern, the statistically optimal map of F_j in terms of both source location and flux is obtained by convolving $\Delta D(\vec{z})$ with $\Delta M^{eff}(\vec{y})$:

$$I(\vec{x}) = \int \Delta D(\vec{z}) \Delta M^{eff}(\vec{x}+\vec{z}) d^2\vec{z}, \qquad (A.1)$$

where $I(\vec{x})$ is the resulting image value at a point on the map, with an angular scale given by the geometry of the instrument. It is important to note that this method is valid only for a uniformly redundant array. This is not a valid technique to use with random-pattern and other masks, and will produce artifacts in the resulting images.

In our implementation of this convolution, we use a method called back-projection, which is described in Cook *et al.* (1984). This is a way of factoring the

convolution into computationally-efficient steps, and it yields the same image as would a direct implementation of the integral.

A.4   The GRIP Rotating HURA Mask

The GRIP instrument uses a Hexagonal URA (HURA) mask pattern that is anti-symmetric (except for the central cell of each unit pattern) under a 60° rotation about the center. Figure 3.1 in Chapter 3 shows the two mask patterns used in GRIP. During data acquisition the mask is rotated at 1 revolution per minute. As a result, each mask measurement is followed 10 seconds later by an antimask measurement.

In GRIP, the mask rotates continuously. To simplify analysis, the data is partitioned by the mask rotation angle into 60 data subsets, with labels $i=0,1,2...59$. Each subset contains the data from six 1° ranges of mask angle per rotation (three mask, and three antimask, spaced 60° apart). If the angle of rotation of the mask is expressed to the nearest degree as $(i+60n)°$ (where the integer n cycles from 0 through 5 with each 360° rotation of the mask), then even n's correspond to the mask orientation (each event is added to $\Delta D_i(\vec{z})$), while odd n's correspond to the anti-mask orientation (each event is subtracted from $\Delta D_i(\vec{z})$).

This results in a set of 60 "sub-images":

$$I_i(\vec{x}) = \int \Delta D_i(\vec{z}) \Delta M_i^{eff}(\vec{x}+\vec{z})d^2\vec{z} ,$$

which are added together to get a final image:

$$I(\vec{x}) = \sum_i I_i(\vec{x}) .$$

The use of a larger number of sub-images (*e.g.*, by dividing the data into 120 subsets, each separated by $\frac{1}{2}^{\bullet}$ of mask rotation) is straightforward, but does not significantly enhance the quality or accuracy of images produced by GRIP.

A.4.1   Artifacts And Their Removal

Because the mask is made up of repetitions of a basic pattern (with 79 or 31 cells for the two GRIP masks), the resulting sub-image, I_i, of a source for a given mask-antimask pair consists of a true source peak surrounded by a triangular lattice of "alias" peaks, one for each repetition of the unit cell. As the mask rotates, this lattice rotates around the true peak location, and the summation to obtain I spreads the alias peaks into a set of concentric rings.

These rings have a much lower amplitude than the peaks they surround ($\lesssim 20\%$ depending on the mask design and the PSF of the detector), therefore if a source is not detected at a significant level, its ring is also insignificant.

Because the coded aperture pattern used is uniformly redundant (*i.e.*, its auto-correlation function is constant except near the repetition lattice points), the area of a sub-image away from the source peak and its aliases is not affected by that source. Because the alias peaks rotate around the source peak with the mask, and are in a different place in each sub-image, an image can be accumulated which does not include the alias peaks.

The computational procedure to do this, called "WISK," was developed specifically for GRIP data analysis. It removes the rings around explicitly chosen sources by setting to zero the regions of each sub-image, $I_i(\vec{x})$, that correspond to the alias peaks of the selected sources. The image at a point on the ring, therefore, contains data only from those mask orientations that do not put it near an alias

peak of a known source. This corresponds to a measurement with a reduced (but well-defined) effective livetime.

At points away from the rings removed by WISK, the resulting image is identical to the un-WISKed image. In particular, for an image with a single strong source, the source peak and its surrounding region are completely unaffected.

WISKed images were used to search for additional sources in the field of view of SN 1987A. No other sources were found, and so the region near SN 1987A is free of ring artifacts and unaffected by WISKing. The images shown in Figures 6.1b-c have had the SN 1987A rings WISKed. Figures 6.1a,d have no detected sources, and are not WISKed.

A.5   Statistics of Source Peaks

For each sub-image, the expected shape of a peak due to a point source is a delta function convolved twice with the point-spread function (PSF) of the detector, and twice with a hexagon with the size and orientation of a mask cell. (The summation of the sub-images with different hexagon orientations, and the smoothing of the hexagons by the repeated convolution, allow the hexagons to be approximated by circles in practical implementation and analysis of the imaging.)

This peak shape is represented by the function $f(\vec{x}-\vec{x_0})$. The normalization of this function is chosen to set its integral to unity. (The unit of area used in the normalization integral is the area of one mask cell—approximately 0.3 and 1.0 square degrees for the Configuration I and Configuration II masks, respectively.)

If the detector PSF were a delta function (*i.e.*, the location of each γ-ray interaction is exactly determined) then the normalized value at the origin would

be $f(\vec{0}) = 1$. For a PSF with finite width, $f(\vec{0}) = \varepsilon < 1$. ε is called the *imaging factor*, and depends on the ratio of the mask cell size to the PSF size. The imaging factor as a function of energy is shown in Figure 3.13. Typical values at 100 and 500 keV are 0.50 and 0.74 for Configuration I, and 0.73 and 0.88 for Configuration II, respectively.

For a point source at $\vec{x_0}$ which produces N_s detected γ-rays during an observation[2], the expected image is $\langle I(\vec{x}) \rangle = N_s f(\vec{x} - \vec{x_0})$. The image value at the source location provides an unbiased estimator of the number of detected γ-rays from the source: $\langle N_s \rangle = I(\vec{x_0})/\varepsilon$. From the effective area of the instrument and the livetime of the observation, the number of detected γ-rays may be converted to a detector spectrum and thence to a source spectrum by the methods described in Chapter 5.

The variance in the image is:

$$\sigma_I^2 = \langle (I(\vec{x}) - \langle I(\vec{x}) \rangle)^2 \rangle$$
$$= \varepsilon N$$

where N is the total number of detected γ-rays, both source and background, which are included in the data analysis. The distribution is Poissonian, but in practice N is large enough that it may be treated as Gaussian. This variance is the

---

[2]At high energies, when the closed cells in the mask are slightly transparent, N_s is the difference between the number of detected source photons which pass through the transparent mask cells and the number which pass through the opaque cells. This is compensated for by an adjustment in the instrument transmission for the opacity of a closed mask cell (see §3.8). As seen in Table 3.2, this opacity at 1 MeV is 78% and 88% for Configurations I and II.

same at every point in an un-WISKed image, regardless of whether it is at a source location or away from a source. (For a WISKed image, the points on a removed ring have a lower variance than the rest of the image because some fraction of the events have been excluded from contributing to those points.)

The expected statistical significance of a source of a given strength (and, therefore, predictable $\langle N_s \rangle$) in an image is:

$$
\begin{aligned}
\langle \eta \rangle &= \frac{\langle I(\vec{x_0}) \rangle}{\sigma_I} \\
&= \frac{\varepsilon \langle N_s \rangle}{\sqrt{\varepsilon N}} \\
&= \langle N_s \rangle \sqrt{\frac{\varepsilon}{N}} \quad .
\end{aligned}
$$

This is a factor of $\sqrt{\varepsilon}$ below the formal statistical significance of a conventional (source–background) instrument. $(1 - \sqrt{\varepsilon})$ can therefore be considered the statistical penalty on the sensitivity of an imaging system. This penalty may be reduced by increasing the size of the mask cells (as was done for the Configuration II mask), which, however, reduces the angular resolution of the telescope. This trade-off between resolution and sensitivity is examined in Finger (1987), which shows that a reasonable balance can be found.

The location, $\vec{x}_{obs}$, of the summit of a peak corresponding to a source will have statistical errors about the location, $\vec{x_0} = \vec{x}_{actual}$, which would be predicted from a complete and accurate knowledge of the source location and the telescope pointing direction. These errors are calculated in Finger (1987) for the case of significant peaks ($\langle \eta \rangle \geq 3$).

The distribution of the statistical position error, $(\vec{x}_{obs} - \vec{x}_{actual})$, in the Finger calculation, is a circular Gaussian with a standard error in each axis of:

$$\sigma_x = \sigma_y \;\; = \frac{1}{\langle \eta \rangle} \sqrt{\frac{2f(\vec{0})}{|\nabla^2 f(\vec{0})|}} \;.$$

The square of the distance between the location of the source and the top of its image peak, $|\vec{x}_{obs} - \vec{x}_{actual}|^2$ is therefore χ^2 distributed (2 degrees of freedom) with a root-mean-value of:

$$\langle |\vec{x}_{obs} - \vec{x}_{actual}|^2 \rangle^{1/2} \;\; = \sqrt{\sigma_x^2 + \sigma_y^2}$$

$$= \frac{2}{\langle \eta \rangle} \sqrt{\frac{f(\vec{0})}{|\nabla^2 f(\vec{0})|}} \;.$$

Although the image value at the location of the source, $I(\vec{x}_{actual})$, provides a linear, normally distributed, unbiased estimator of the source strength, the image value at the observed peak, $I(\vec{x}_{obs})$, does not. $I(\vec{x}_{obs}) \geq I(\vec{x}_{actual})$ (because $\vec{x}_{obs}$ is at the maximum local to $\vec{x}_{actual}$), and so gives a positively biased flux estimator. The expected bias is found to be:

$$\langle I(\vec{x}_{obs}) - I(\vec{x}_{actual}) \rangle \;\; = \frac{1}{\langle \eta \rangle^2} \langle I(\vec{x}_{actual}) \rangle \;.$$

Therefore, the flux of a source estimated from a measurement of the image at the peak location will tend to be $(1 + \frac{1}{\langle \eta \rangle^2})$ of the true value, on average. The bias has a nominal significance of $\frac{1}{\langle \eta \rangle} \sigma$.

Appendix B
Limits On The Effects Of Pointing Errors

For both D414 and D268 observations, there is an image peak near to, but statistically inconsistent with, the nominal location of SN 1987A. The data analysis in this thesis is based on the belief that these peaks are actually due to SN 1987A, displaced by residual systematic errors in our determination of the instrument pointing direction. The size of the peak displacement ($\sim$0.3°) is comparable to the pointing offsets measured during observations of bright γ-ray sources at known locations, such as the Crab Nebula and Pulsar, and Cygnus X-1. These measured pointing errors tend to be consistent with errors in the determination of the telescope azimuth, with relatively little error in the elevation (see Tables C.1a-d in Appendix C).

The two main potential problems resulting from pointing error in our measurements are misidentification of the source responsible for the peak, and reduction in the measured source strength due to image blurring.

To bound the effects of the pointing error, I developed a procedure which determines the maximum flux which would be measured as coming from a point on the sky, consistent with reasonable azimuthal errors in the pointing direction. If this maximum flux is significantly less than the flux required to produce the

image peak, this indicates that the peak was not produced solely by flux coming from that point in the sky. The maximum flux places an upper bound on the flux that would be measured from a source if the telescope pointing direction were perfectly known.

These maximized fluxes thus allow an image peak to be ascribed to a specific source, and allow limits to be placed on the effects of pointing errors on measured fluxes.

B.1 Maximization Procedure

A point on the image, $\vec{x}_{target}$ (e.g., $\vec{x}_{target} = \vec{x}_{nom}$(SN 1987A) or $\vec{x}_{nom}$(LMC X-1)), is targeted for maximization. For each pointing, i, the azimuthal offset is adjusted away from the nominal:

$$\Delta'_{az,i} = \Delta_{az,i} + \delta_i$$

to maximize the image value for $\vec{x}_{target}$ in the composite image produced for that pointing. This is equivalent to choosing the highest point in a search region that is a line in the image (the line of constant elevation) that passes through the target and is parallel to the horizon at the time of the pointing, and shifting the image along that line to move that highest point to the target point.

The set of $\Delta'_{az,i}$ obtained in this way maximizes the significance of the composite image of the whole dataset at the target point, $\eta_\delta(\vec{x}_{target})$ with respect to the individual azimuthal pointing offsets. The value of the maximized $\eta_\delta(\vec{x}_{target})$ is thus an upper bound to the significance that would have been obtained if the instrument had had perfect pointing accuracy in the azimuthal direction, assuming that the pointing error does not vary significantly during each individual pointing.

The maximized $\eta_\delta(\vec{x}_{target})$, however, is positively biased above the value for perfect pointing. If there is not a significant peak due to a source in the image from a pointing the maximization procedure selects the largest noise peak in the search region. To reduce the contribution of noise peaks to the image, the constraint $|\delta_i| \leq 1.5°$ was added to keep the azimuthal pointing errors within the range we have experienced in our observations of sources at known locations.

In some cases, a large $|\delta_i|$ produces only a marginal improvement over a small one when a noise peak that is slightly higher than the true source peak is within the allowed $|\delta_i|$ range. This problem may be reduced by adding a penalty function to the function being maximized:

$$f(\vec{\delta}) \ = \ \eta_\delta^2(\vec{x}_{target}) - \sum_i \frac{\delta_i^2}{\vartheta^2} \ .$$

This determines the amount of preference given to peaks that are near to the nominal source location and, thus, more likely to be due to the source. An infinite ϑ corresponds to the case of no penalty function, specifying that a peak with an offset of 1.4° is just as likely to be due to the source as a peak with no offset. An infinitesimal ϑ forces the δ_is to zero, selecting only the value at the nominal location and yielding the nominal image. A ϑ comparable to a large but not unreasonable azimuthal offset (e.g., 0.5°) provides some protection against noise peaks while allowing the pointing to vary as the data suggests.

The images used were composite images, based on a $\gamma=1$ power-law template. However, the fact that the peak of the image moves by less than one pixel (0.1°) for composite images with templates in the range of $\gamma=0$ to $\gamma=3$ suggests that the same results (although with lower significance) would be obtained for analyses using any reasonable template.

B.2   Statistics of the Maximized Peaks

The maximization procedure described above accumulates a positively biased estimate of source intensity for each pointing, giving a summed measurement for an entire observation which is strongly positive-biased. This can result in high significance "detections" of sources which do not, in fact, exist.

The maximum value in the search area of the image for pointing i will have an expectation value, $\langle I_i^{max} \rangle$, greater than the expectation value of any specific point in the search region. If there is no source in the search area, so the expectation value of each point in the search region is zero, then $\langle I_i^{max} \rangle > 0$. If there is a source in the search region that is significant at the sensitivity of the image, then I_i^{max} will be positively biased compared to the source strength:

$$\langle I_i^{max} \rangle > \langle I(\vec{x}_{theor}) \rangle.$$

B.2.1   Statistics For A Sourceless Image

If there is no significant source in the image, $\langle I_i^{max} \rangle$ will depend on the size and shape of the search region, compared to the size and shape of the PSF of the image. Expressing the bias b_i in terms of the standard deviation, σ_i, of the image, $b_i = I_i^{max}/\sigma_i$ gives a distribution that is independent of the sensitivity of the image. The statistics of the maximum in the region can be calculated analytically (with approximations) or determined through numerical experimentation.

I chose an experimental approach, with a simplified analytic check for verification. I searched a large number (>>1000) of areas on images with no significant sources. The distribution of b_i depends on the configuration of GRIP, as expected.

I used the conditions: $|\delta_i| \leq 1.5°$, no penalty function, with the telescope pointing ~35° above the horizon. This gives a search area which is a line 2.5° long on the image.

For Configuration I, $\langle b_i \rangle = 1.42$ with a standard deviation of the maximum, $\sigma_{b_i} = \sqrt{\langle b_i{}^2 \rangle - \langle b_i \rangle^2} = 0.66$. For Configuration II, $\langle b_i \rangle = 1.21\sigma_i$, and $\sigma_{b_i} = 0.74$.

The statistics of b_i are difficult to calculate analytically, (although a related function, the height distribution of local maxima in an image, has been determined (Finger 1987)). A distribution that might be expected to have similar properties is the maximum of N independent samples of a normal distribution, with N approximately equal to the number of peaks which will fit in or near the search region. For the analytic check, I compared the measured distributions to the N-sample distribution, choosing N to make the means of the distributions equal (in terms of σ for the sampled distributions), and generalizing to allow non-integral values of N.

The means are equal at $N=8.6$ for Configuration I or $N=5.7$ for Configuration II, corresponding to a separation between independent samples of 0.29° and 0.43°, respectively. These separations are reasonable—a first-order intuitive guess for these values would be a characteristic radius of the PSF, divided by $\sqrt{2}$ to account for the search in one dimension for two-dimensional peaks. A further check is provided by a comparison of the widths of the measured and analytical distributions. For each configuration, these two widths were equal to within 20%.

B.2.2 Statistics For An Image Containing a Source

For the case of a significant source peak in the search region, analytical calculation of the bias is similar to the bias calculation described in Appendix A. A significant source peak is one whose expectation value in an image is significantly higher than the expected bias, $\langle b_i \rangle \sigma_i$, for a sourceless image .

For a 1-dimensional search, the positive bias of the maximum is one-half the bias of the local maximum found by a 2-dimensional search (see Appendix A). A source which would be expected to produce a detection at $\vec{x}_{theor}$ with a significance of $\eta_i \sigma_i$ would produce a peak of

$$\langle I_i^{max} \rangle = (1 + \frac{1}{2\eta_i^2})\langle I(\vec{x}_{theor}) \rangle$$

$$= (\eta_i + \frac{1}{2\eta_i}) \, \sigma_i \, .$$

so the bias (in standard deviations) is

$$\langle b_i \rangle = \frac{\langle I_i^{max} \rangle - \langle I(\vec{x}_{theor}) \rangle}{\sigma_i}$$

$$= \frac{1}{2\eta_i}$$

and the standard deviation of the maximum is just the standard deviation of the peak height: $\sigma_{b_i} = 1$.

B.2.3 Statistics of the Maximized Image

The total bias for an observation is composed of the biases for the individual pointings. Using images for each pointing calibrated in terms of flux for a given template, each with its own σ_i, the expected distribution of the significance of the peak can be obtained from:

$$I^{max} = \sigma^2 \sum_i \frac{1}{\sigma_i^2} I_i^{max}$$

where $\sigma^2 = (\sum_i \frac{1}{\sigma_i^2})^{-1}$ is the variance of the image you would get from the template-optimized addition without the maximization routine.

The distribution of the maximized image value is:

$$\langle I^{max} \rangle = \sigma^2 \sum_i \frac{1}{\sigma_i^2} \langle I_i^{max} \rangle$$

$$= \sigma^2 \sum_i \frac{1}{\sigma_i} \langle b_i \rangle + \langle I(\vec{x}_{theor}) \rangle$$

$$\sigma_I^{2\ max} = \sigma^4 \sum_i \frac{1}{\sigma_i^2} \sigma_{b_i}^2.$$

For the case where there is no source, $\langle b_i \rangle$ and $\sigma_{b_i}^2$ are constants (for a given instrument configuration). For the case of n equally sensitive pointings, the maximized peak will have a significance of $\langle I^{max} \rangle = \sqrt{n} \langle b_i \rangle \sigma$. The standard deviation of the maximized peak is the same (in terms of significance) as for the maximized peak of each pointing: $\sigma_I^{max} = \sigma_{b_i} \sigma$.

If there is a significant source, then $\langle I^{max} \rangle = (1 + \frac{\sqrt{n}}{2\eta}) \langle I(\vec{x}_{theor}) \rangle$, independent of the relative sensitivities of the pointings, with $\sigma_I^{max} = \sigma$.

B.3   Results of Maximization

The results of this analysis for all flights are shown in Table B.1.

Observation (number of pointings)	Target	Nominal $(\vartheta\to0)$ η	Restricted $(\vartheta=0.5°)$ η	$\bar{\delta_i}\pm\sigma_\delta$	Unrestricted $(\vartheta\to\infty)$ η	$\bar{\delta_i}\pm\sigma_\delta$
	Peak	2.49				
D85	SN 1987A	1.54	2.93	0.0°±0.3°	3.03	0.0°±0.5°
(4)	LMC X-1	0.72	2.01	-0.2°±0.3°	2.65	-0.1°±1.2°
	Peak	4.83				
D268	SN 1987A	3.36	4.68	0.3°±0.1°	4.80	0.5°±0.3°
(4)	LMC X-1	0.98	3.40	0.4°±0.5°	4.13	-0.2°±1.2°
	Peak	8.74				
D414	SN 1987A	7.71	9.11	0.2°±0.3°	9.24	0.0°±0.6°
(11)	LMC X-1	2.23	4.83	0.1°±0.5°	5.68	-0.3°±0.8°
	Peak	2.35				
D771	SN 1987A	0.79	1.06	0.1°±0.1°	1.99	-0.6°±0.4°
(3)	LMC X-1	-0.98	0.36	0.0°±0.1°	2.14	-0.5°±1.2°

Table B.1 — The results of the maximization routine for the locations of SN 1987A and LMC X-1. The nominal image is the image without any adjustments to the pointing. The restricted and unrestricted images have had offsets added to the azimuth of the telescope as required to maximize the image value at the target. In the case of the restricted image, a penalty function was added to preferentially choose smaller offsets, while in the unrestricted image, the azimuthal offset was constrained only by a limit of ±1.5°. η is the maximized statistical significance of the image at the target, while $\bar{\delta_i}$ is the average azimuthal offset required to obtain that η, and σ_δ is its standard deviation.

B.4 Bounds On The Flux Error for D414

The nominal image from the D414 observation has a peak significance of 8.7σ in the nominal image, and a significance at SN 1987A of 7.7σ. Although the 11 pointings of this observation have different sensitivities, each of the sub-images is expected to have a peak significance of $\geq 2\sigma$, based on the sensitivity and peak significance of the combined nominal image. Since the expected bias for an image with no source has a distribution $b_i = 1.21\pm0.74$, most of the peaks found for the subimages will be source peaks, rather than noise peaks.

When SN 1987A is maximized, only two of the pointings are significantly affected by the use of the $\vartheta=0.5°$ penalty function. These are probably noise peaks, while the other nine are close enough to the nominal location of SN 1987A ($\leq 0.7°$ of azimuthal pointing offset) that they are probably source peaks. The peaks selected for the two pointings by the penalty function are probably also source peaks. Therefore, the values produced by the search that is restricted by the $\vartheta=0.5°$ penalty function are probably most useful for determining the effects of pointing error on the flux determination.

The restricted maximization gives η_δ(SN 1987A) = 9.11σ, compared to the 8.74σ at the peak of the nominal image. This 0.35σ excess places an upper limit of 4% on the reduction in measurement sensitivity due to pointing errors. This upper limit is conservative in the sense that it ignores the expected bias, which at 0.19σ is more than half of the excess. However, even a 4% bias is not significant compared to the statistical accuracy of our measurements.

B.5   Bounds On Identification Error For D414

An equivalent maximization of LMC X-1 for the same observation, with no penalty function, results in a maximum $\eta_\delta(\vec{x}_{nom}(\text{LMC X-1})) = 5.68\sigma$. This is significantly (>3σ) below both the peak value and the maximized $\eta_\delta(\vec{x}_{nom}(\text{SN 1987A}))$ value, indicating that LMC X-1 is not the main source of the flux in the peak. The variance in the required δ_is is also large ($\sigma_\delta=0.8°$), suggesting that the maximization procedure is selecting the randomly-located noise peaks, rather than the systematic offsets produced by pointing errors. Use of the penalty function further reduces the value to $\eta_\delta(\vec{x}_{nom}(\text{LMC X-1})) = 4.83\sigma$, providing further evidence that the unpenalized maximization relies heavily on noise peaks in the search region.

The line comprising the search region for maximizing LMC X-1 is parallel to and offset from the SN 1987A search region. The separation between the lines can vary between the total separation of the sources (0.6°), and zero, as the sky rotates relative to the horizon. Thus, the highest point in the LMC X-1 search region is often the point that is nearest to the SN 1987A peak, where the line cuts across the shoulder of its point spread function. In the image maximized for LMC X-1 with the penalty function, the value at SN 1987A is almost 2σ higher than it is at LMC X-1 (6.74σ vs. 4.83σ) and the image peak is more than twice as far from LMC X-1 as it is from SN 1987A. Thus, even when every bias favors LMC X-1, SN 1987A is the dominant of the two sources.

If the instrument pointing was perfectly known, and the sole source of flux were SN 1987A, then the image value at the position of LMC X-1 would be ~50% of the value at SN 1987A, due to the width of the PSF (55% at 50 keV, 42% above 500 keV). This agrees with the values in Table B.1. The data, therefore, is

consistent with SN 1987A being the sole source of flux for D414 the D414 observations.

B.6   Bounds For Other Observations

For the D268 observations, the peak in the nominal image is more significant than the maximized value of either of the two sources. This implies that the positive bias in the flux due to the selection of $\vec{x}_{meas} = \vec{x}_{obs}$ (which has an expectation value of $\frac{1}{4.8}$=0.2σ based on the expression in Appendix A) is greater than the positive bias produced by the maximization procedure (also expected to be 0.2σ).

For the D268 observation, this analysis does not entirely rule out the possibility that flux comes from LMC X-1, but the large variance in δ (σ_δ=1.2˝) required to obtain LMC X-1 fluxes comparable to the values at the peak of the nominal image suggests that the maximization procedure is merely piling up noise peaks. Placing the restriction of the penalty function on the maximization drops the value at LMC X-1 to 1.4σ below the nominal peak, and 1.3σ below the restricted maximum value for SN 1987A, which is obtained with a much smaller variance in δ (σ_δ=0.1˝).

For the D86 and D771 observations, the results indicate that neither source produced significant flux. The predicted maximized values of η for sourceless images, based solely on the statistics of noise peaks, are 2.7±0.7 and 2.1±0.7 σ for D86 and D771, respectively. These are consistent with the maximized values for both sources.

B.7 Pointing Error Effects—Conclusions

By these tests, it was determined that the pointing errors do not smear out the image peaks enough to significantly reduce the sensitivity of the measurements. In addition, for the two observations that yielded positive detections of a source in the field of view, LMC X-1 was certainly (D414) or probably (D268) eliminated, leaving SN 1987A as the dominant source of flux near its location.

If LMC X-1 were producing significant flux (although at a lower intensity than SN 1987A) the shoulders of its peak could contribute to the image value at the location of SN 1987A's peak. However, this cross-contribution would cause an increase in the measured SN 1987A flux by only ~50% of the true LMC X-1 flux, which would not be a significant contribution. Using the restricted maximizations given in Table B.1, this implies that the contribution to the measured SN 1987A flux from LMC X-1 is $\frac{3.40}{4.68}50\% = 36\%$ and $\frac{4.83}{9.11}50\% = 27\%$ for D268 and D414, respectively. These must be considered extremely conservative upper limits. If LMC X-1 were, in fact, this strong, the images would appear double-peaked, or at least severely elongated in the direction of the line between SN 1987A and LMC X-1. The data analysis in this thesis, therefore, assumes that LMC X-1 does not significantly contaminate our measurements of SN 1987A.

Appendix C
Details Of Individual Pointings

C.1   Pointings

GRIP made four flights from Alice Springs, Australia to observe
SN 1987A. Each "observation" (defined as the set of data obtained for a particular
source during a flight) of SN 1987A was divided into multiple "pointings", each
typically ~1 hour long. These pointings are detailed in Tables C.1a-d.

Each pointing was analyzed using the mean line-of-sight atmospheric
depth between the instrument and the source as the basis for attenuation
calculations. The spectra obtained for each pointing were combined to give a
spectrum for the complete observation.

During our observations, GRIP alternately observed SN 1987A and the
Crab. The SN 1987A observations were typically longer (~1 hour) than the Crab
observations (~20 minutes). This provided a natural division of the observation
into SN 1987A pointings and Crab pointings. During some observations, GRIP
continuously tracked SN 1987A for much longer than 1 hour (*e.g.*, during the
D414 flight, 1988 April 12.058-12.196, SN 1987A was observed continuously for
3.3 hours). These periods were subdivided into shorter pointings, to give each

pointing a smaller range of atmospheric attenuation, resulting in a more precise flux measurement.

Data from each pointing was imaged with its own set of pointing offsets, Δ_{az} and Δ_{el}, which specify the difference between the telescope pointing direction as measured by on-board sensors, and a post-flight best determination of the true telescope pointing direction. During the Crab pointings, these offsets were determined from the location of the Crab on images obtained using the pointing direction calculated using the sensors. During the SN 1987A pointings, the offsets were based on the adjacent Crab measurements and (for the D414 and D771 flights) on data from the Sun camera system.

D86 Observed Source	Observation Period (UT Day of 1987 May)	Mean Line-of-sight Atmosphere (g cm^{-2})	Pointing Corrections (degrees)		Notes
			Δaz	Δel	
SN 1987A	19.970—20.003	10.4	-0.84	0.29	
SN 1987A	20.003—20.083	8.5	-0.84	0.29	
Crab	20.084—20.105	8.1	-0.84	0.29	
SN 1987A	20.106—20.172	6.4	-0.75	0.36	
Crab	20.173—20.195	6.9	-0.67	0.43	
SN 1987A	20.195—20.269	6.1	-0.38	0.41	
Crab	20.270—20.286	7.8	-0.09	0.38	

Table C.1a — Details of SN 1987A and Crab pointings during the D86 flight. The Δaz and Δel corrections for the SN 1987A pointings are based on adjacent Crab pointings.

D268 Observed Source	Observation Period (UT Day of 1987 Nov.)	Mean Line-of-sight Atmosphere (g cm^{-2})	Pointing Corrections (degrees)		Notes
			Δaz	Δel	
Crab	18.607—18.623	8.0	0.42	-0.17	
SN 1987A	18.624—18.648	7.0	0.40	-0.20	
Crab	18.668—18.670	7.1	0.20	-0.12	
SN 1987A	18.676—18.703	6.6	0.50	-0.10	
SN 1987A	18.736—18.761	7.1	0.78	0.00	
Crab	18.762—18.778	7.1	0.77	0.04	
SN 1987A	18.779—18.810	6.8	0.78	0.00	
Crab	18.812—18.821	8.5	0.88	-0.03	Mask Stopped at 18.821

Table C.1b — Details of SN 1987A and Crab pointings during the D268 flight. The Δaz and Δel corrections for the SN 1987A pointings are based on adjacent Crab pointings. The mask stopped rotating at 1987 November 18.821, so subsequent Crab and SN 1987A pointings are not listed.

D414 Observed Source	Observation Period (UT Day of 1988 April)	Mean Line-of-sight Atmosphere (g cm⁻²)	Pointing Corrections (degrees)		Notes
			Δaz	Δel	
SN 1987A	12.058—12.126	10.4	-0.20	0.00	
SN 1987A	12.126—12.196	8.2	-0.11	0.00	
Crab	12.205—12.217	8.4	-0.82	-0.02	
SN 1987A	12.220—12.250	7.3	-0.10	0.00	
Crab	12.252—12.266	7.9	-0.52	0.00	
SN 1987A	12.267—12.297	7.6	0.13	0.00	
Crab	12.298—12.313	7.6	-0.27	-0.03	
SN 1987A	12.314—12.352	7.8	0.40	0.00	
Crab	12.353—12.367	8.5	0.12	0.00	
SN 1987A	12.368—12.398	8.0	0.35	0.00	
Crab	12.400—12.414	9.4	0.41	0.02	
SN 1987A	12.414—12.453	7.8	0.32	0.00	
SN 1987A	12.463—12.492	8.7	0.36	0.00	
SN 1987A	13.058—13.126	9.5	0.11	0.13	Second day
SN 1987A	13.126—13.203	8.3	0.05	0.16	
Crab	13.205—13.219	8.4	-0.51	0.17	
SN 1987A	13.220—13.250	7.7	-0.10	0.18	
Crab	13.251—13.260	7.6	-0.20	0.19	

Table C.1c — Details of SN 1987A and Crab pointings during the D414 flight. For SN 1987A, Δ_{el} corrections are based on the adjacent Crab pointings; Δ_{az} corrections are based on Sun camera data.

D771 Observed Source	Observation Period (UT Day of 1989 April)	Mean Line-of-sight Atmosphere (g cm^{-2})	Pointing Corrections (degrees) Δaz	Δel	Notes
SN 1987A	4.171—4.224	7.1	0.55	0.20	
Crab	4.225—4.239	8.3	0.00	0.20	A0535+26 observed
SN 1987A	4.240—4.278	6.2	0.60	0.21	
Crab	4.279—4.370	7.6	-0.28	0.23	A0535+26 observed
SN 1987A	4.371—4.433	8.2	0.60	0.17	
Crab	4.434—4.466	12.8	0.77	0.11	A0535+26 observed

Table C.1d — Details of SN 1987A and Crab pointings during the D771 flight. For SN 1987A, Δ_{el} corrections are based on the adjacent Crab pointings; Δ_{az} corrections are based on Sun camera data.

References

Ables, J.G. 1968, *PASA* 1(4), 172-173

Ait-Ouamer, F., Kerrick, A.D., O'Neill, T.J., Tumer, O.T., Zych, A.D., and White, R.S. 1990, In *21st ICRC Conference papers*, IUPAP, University of Adelaide, 183-186

Allen, J.A.V., Baker, D.N., Randall, B.A., and Sentman, D.D. 1974, *J.G.R.* 79(25), 3559-3577

Althouse, W.E., Cook, W.R., Cummings, A.C., Finger, M.H., Palmer, D.M., Prince, T.A., Schindler, S.M., Starr, C.H., and Stone, E.C. 1985, In *Proc. 19th Int. Cosmic Ray Conf. (La Jolla) (NASA CP-2376)*, IUPAP, 299

Althouse, W.E., Cook, W.R., Cummings, A.C., Finger, M.H., Palmer, D.M., Prince, T.A., Schindler, S.M., Starr, C.H., and Stone, E.C. 1987, In *Proc. 20th Int. Cosmic Ray Conf. (La Jolla) (NASA CP-2376)*, IUPAP, 84

Anders, E. and Grevesse, N. 1989, *Geochimica et Cosmochimica Acta* 53, 197-214

Arnett, W.D. 1988, *ApJ* 331, 377-387

Arnett, W.D., Bahcall, J.N., Kirshner, R.P., and Woosley, S.E. 1989a, *ARA&A*, Annual Reviews Inc., Vol. 27 629-700

Arnett, D., Fryxell, B., and Müller, E. 1989b, *ApJ (Letters)* 341, L63-L66

Aschenbach, B., Briel, U.G., Pfeffermann, E., Bräuninger, H., Hippman, H., and Trümper, J. 1987, *Nature* **330**, 232-233

Bahcall, J. 1989, *Neutrino Astrophysics*, Cambridge University Press

Bartunov, O.S., Blinnikov, S.I., Levakhina, L.V., and Nadezhin, D.K. 1987, *Soviet Astr. Letters* **13**(5), 313-316

Berger, M.J. and Hubbell, J.H. 1987, *XCOM: Photon cross sections on a personal computer*, Computer Software from National Institute of Science and Technology,

Bevington, P.R. 1969, *Data reduction and error analysis for the physical sciences*, McGraw-Hill

Bionta, R.M. *et al.* 1987, *Phys. Rev. Letters* **58**(14), 1494-1496

Birks, J.B. 1953, *Scintillation Counters*, McGraw-Hill

Bouchet, P., Phillips, M.M., Suntzeff, N.B., Gouiffes, C., Hanuschik, R.W., and Wooden, D.H. 1991, *A&A* **245**, 490-498

Bouchet, P., Danziger, I.J., and Lucy, L.B. 1991, *AJ* **102**(3), 1135-1146

Burki, G., Cramer, N., and Nicolet, B. 1991, *A&A Suppl.* **87**, 163-175

Burrows, T.W. and Bhat, M.R. 1986, *Nuclear Data Sheets* **47**(1), 1

Burrows, D., Nousek, J., and Garmire, G. 1987, *IAU Circular No. 4494*,

Bussard, R.W., Burrows, A., and The, L.S. 1989, *ApJ* **341**, 401-413

Caroli, E., Stephen, J.B., Cocco, G.D., Natalucci, L., and Spizzichino, A. 1987, *Space Science Reviews* **45**(3-4), 349-403

Catchpole, R.M. *et al.* 1987, *MNRAS (Short Communication)* **229**, 15p-25p

Catchpole, R.M. *et al.* 1988, *MNRAS (Short Communication)* **231**, 75p-89p

Catchpole, R.M. *et al.* 1989, *MNRAS (Short Communication)* **237**, 55p-68p

Chahan, G.A., Helfand, D.J., and Reynolds, S.P. 1984, *ApJ (Letters)* **L287**(1), L23-L26

Chan, K.W. and Lingenfelter, R.E. 1987, *ApJ (Letters)* **318**, L51

Chan, K.W. and Lingenfelter, R.E. 1988, In *AIP Conference Proceedings 170: Nuclear Spectroscopy of Astrophysical Sources*, Gehrels, N. and Share, G.H. *ed.*, AIP, AIP, 110-115

Clark, D.H., Tuohy, I.R., Long, K.S., Szymkowiak, A.E., Dopita, M.A., Mathewson, D.S., and Culhane, J.L. 1982, *ApJ* **255**(2), 440-446

Clayton, D.D., Colgate, S.A., and Fishman, G.J. 1969, *ApJ* **155**, 75-82

Clayton, D.D. 1974, *ApJ* **188**(2), 155-157

Cook, W.R., Finger, M., Prince, T.A., and Stone, E.C. 1984, *IEEE Trans. Nucl. Sci.* **NS-31**(1), 771-775

Cook, W.R., Finger, M., and Prince, T.A. 1985, *IEEE Trans. Nucl. Sci.* **NS-32**(1), 129-133

Cook, W.R., Palmer, D.M., Prince, T.A., Schindler, S.M., Starr, C.H., and Stone, E.C. 1988, *ApJ (Letters)* **334**, L87-L89

Cook, W.R., Grunsfeld, J.M., Heindl, W.A., Palmer, D.M., Prince, T.A., Schindler, S.M., Starr, C.H., and Stone, E.C. 1991, In *Advances in Space Research - Proceedings of COSPAR 1990*. Pergammon Press, (8)191-(8)202,

Cook, W.R., Grunsfeld, J.M., Heindl, W.A., Palmer, D.M., Prince, T.A., Schindler, S.M., and Stone, E.C. 1991, *ApJ (Letters)* **372**(2), L75-L78

Craig, I.J.D. and Brown, J.C. 1986, *Inverse Problems in Astronomy, a guide to inversion strategies for remotely sensed data*, Adam Hilger Ltd, Bristol and Boston

Cropper, M., Bailey, J., McCowage, J., Cannon, R.D., Couch, W.J., Walsh, J.R., Strade, J.O., and Freeman, F. 1988, *MNRAS* **231**, 695-722

Dicke, R.H. 1968, *ApJ (Letters)* **153**, L101-L106

Doggett, J.B. and Branch, D. 1985, *AJ* **90**(11), 2303-2311

Dotani, T. *et al.* 1987, *Nature* **330**, 230-232

Ebisuzaki, T. and Shibazaki, N. 1988a, *ApJ (Letters)* **327**, L5-L8

Ebisuzaki, T. and Shibazaki, N. 1988b, *ApJ* **328**, 699-703

Efremov, G.A., Titenkov, A.F., Lupenko, G.V., Nazarova, N.I., Postnikov, I.Y., and Sukhanov, V.P. 1990, *Soviet Astr. Letters* **16**(5), 337-338

Evans, R.D. 1955, *The atomic nucleus*, Krieger Publishing

Falk, S.W. and Arnett, W.D. 1973, *ApJ (Letters)* **180**, L65-L68

Fenimore, E.E. and Cannon, T.M. 1978, *Appl. Optics* **17**(3), 337-347

Fenimore, E.E., Klebesadel, R.W., and Laros, J.G. 1983, *ASR* **3**(4), 207-210

Filippenko, A. *et al.* 1992, *ApJ (Letters)* **384**(1), L15-L18

Finger, M.H. 1987, *The imaging of extra-galactic low-energy gamma-ray sources. Prospects, techniques, and instrumentation*, Ph.D. dissertation, California Institute of Technology,

Fishman, G.J., Wilson, R.B., Paciesas, W.S., Meegan, C.A., Pendleton, G.N., and Sandie, W.G. 1990, *ASR* **10**(2), (2)55-(2)58

Fowler, W.A. and Hoyle, F. 1964, *ApJ Suppl.* **9**(91), 201-320

Fu, A. and Arnett, W.D. 1989, *ApJ* **340**, 414-425

Garcia, M.R., Grindlay, J.E., Burg, R., Murray, S.S., and Flanagan, J. 1986, *IEEE Trans. Nucl. Sci.* **33**(1), 735-740

Grebenev, S.A. and Sunyaev, R.A. 1987, *Soviet Astr. Letters* **13**(6), 397-405

Grebenev, S.A. and Sunyaev, R.A. 1989, In *Physics of Neutron Stars.* Nova Science Publishers, Varshalovich, D.A., Kaminker, A.D., Pavlov, G.G., and Yakovlev, D.G. *ed.*, New York,

Grebenev, S.A., Sunyaev, R.A., Pavlinskii, M.N., Dekhanov, I.A., Markevich, M.L., and Yamburenko, N.S. 1991, *Soviet Astr. Letters* **17**(2), 130-134

Haas, M.R., Colgan, S.W.J., Erickson, E.F., Lord, S.D., Burton, M.G., and Hollenbach, D.J. 1990, *ApJ* **360**, 257-266

Hamuy, M., Suntzeff, N.B., Bravo, J., and Phillips, M.M. 1990, *PASP* **102**, 888-897

Harkness, R.P. and Wheeler, J.C. 1990, In *Supernovae*. Springer-Verlag, Petschek, A.G. *ed.*, Ch. 1, 1-29,

Hirata, K. *et al.* 1987, *Phys. Rev. Letters* **58**(14), 1490-1493

Inoue, H., Hayashida, K., Itoh, M., Kondo, H., Mitsuda, K., Takeshima, T., Yoshida, K., and Tanaka, Y. 1991, *Pub. Astr. Soc. Japan* **43**, 213-223

Isern, J., Canal, R., and Labay, J. 1991, *ApJ* **372**, L83-L86

Jeffery, D.J. 1987, *Nature* **329**, 419-421

Jeffrey, W. and Rosner, R. 1986, *ApJ* **310**(1), 463-472

Junde, H., Dailing, H., Chunmei, Z., Xiaoling, H., Baohua, H., and Yaodong, W. 1987, *Nuclear Data Sheets* **51**(1), 1

Jung, G.V. 1989, *ApJ* **338**, 972-982

Kirshner, R.P., Sonneborn, G., Crenshaw, D.M., and Nassiopoulos, G.E. 1987, *ApJ* **320**(2), 602-608

Kumagai, S., Itoh, M., Shigeyama, T., Nomoto, K., and Nishimura, J. 1988, *A&A* **197**, L7-L10

Lampton, M., Margon, B., and Bowyer, S. 1976, *ApJ* **208**(2), 177-190

Lederer, C.M. and Shirley, V.S. 1978, *Table of isotopes (Seventh Edition)*, John Wiley & Sons, New York

Leising, M.D. and Share, G.H. 1990, *ApJ* **357**(2), 638-648

Loredo, T.J. and Epstein, R.I. 1989, *ApJ* **336**, 896-919

Luo, D. and McCray, R. 1991, *ApJ* **379**(1), 659-662

Mahoney, W.A., Varnell, L.S., Jacobson, A.S., Ling, J.C., Radocinski, R.G., and
Wheaton, W.A. 1988, *ApJ (Letters)* **334**, L81-L85

Matteson, J., Pelling, M., Bowman, B., Briggs, M., Lingenfelter, R., Peterson, L.,
Lin, R., Smith, D., Hurley, K., Pehl, R., von Ballmoos, P., Niel, M., and
Durouchoux, P. 1990, In *21st ICRC Conference papers*, IUPAP,
University of Adelaide, 174-177

Mayle, R.W. 1990, In *Supernovae*. Springer-Verlag, Petschek, A.G. *ed.*, Ch. 1, 267-
289,

McCray, R., Shull, J.M., and Sutherland, P. 1987, *ApJ (Letters)* **317**(2), L73-L77

Menzies, J.W. *et al.* 1987, *MNRAS (Short Communication)* **227**, 39p-49p

Miyaji, S., Nomoto, K., Yokoi, K., and Sugimoto, D. 1980, *Pub. Astr. Soc. Japan* **32**,
303-329

Myra, E.S. and Burrows, A. 1990, *ApJ* **364**, 222-231

Panagia, N., Gilmozzi, R., Macchetto, F., Adorf, H.M., and Kirshner, R.P. 1991,
ApJ (Letters) **380**(2), L23-L26

Paul, J. *et al.* 1991, In *Advances in Space Research - Proceedings of COSPAR 1990*.
Pergammon Press,

Pinto, P.A. and Woosley, S.E. 1988, *Nature* **333**, 534-537

Podsiadlowski, P., Fabian, A.C., and Stevens, I.R. 1991, *Nature* **354**, 43-46

Rester, A.C., Coldwell, R.L., Dunnam, F.E., Eichhorn, G., Trombka, J.I., Starr, R., and Lasche, G.P. 1989, *ApJ (Letters)* **342**, L71-L73

Riegler, G.R. 1987, In *ESO Workshop on the SN 1987A*, Danziger, I.J. *ed.*, ESO, 663

Sandie, W.G., Nakano, G.H., Chase, Jr., L. F., Fishman, G.J., Meegan, C.A., Wilson, R.B., Paciesas, W.S., and Lasche, G.P. 1988a, *ApJ (Letters)* **334**, L91-L94

Sandie, W.G., Nakano, G.H., Chase, Jr., L. F., Fishman, G.J., Meegan, C.A., Wilson, R.B., and Paciesas, W. 1988b, In *Supernova 1987A in the Large Magellanic Cloud*, Kafatos, M. and Michalitsianos, A.G. *ed.*, Fourth George Mason Astrophysics Workshop, Cambridge University Press, 366-370

Schwartz, D.A., Wheeler, J.C., and Harkness, R.P. 1991, *ApJ* **374**, 266-280

Seward, F.D., Harnden, Jr., F.R. and Helfand, D.J. 1984, *ApJ (Letters)* **287**(1), L19-L22

Shelton, I. 1987, *IAU Circular No. 4316,*

Shibazaki, N. and Ebisuzaki, T. 1988, *ApJ (Letters)* **327**, L9-L12

Shigeyama, T. and Nomoto, K. 1990, *ApJ* **360**, 242-256

Skinner, G.K. *et al.* 1987, *Nature* **330**(544)

Sood, R.K., Thomas, J.A., Waldron, L., Manchanda, R.K., Ubertini, P., Bazzano, A., Padula, C.L., Staubert, R., Kendziorra, E., Rochester, G.K., Sumner, T.J., Frye, G., Jenkins, T., Koga, R., and Albats, P. 1988, *MNRAS* **234**, 73p-77p

Spyromilio, J., Meikle, W.P.S., and Allen, D.A. 1990, *MNRAS* **242**, 669-673

Suntzeff, N.B. and Bouchet, P. 1990, *AJ* **99**(2), 650-663

Suntzeff, N.B., Phillips, M.M., Depoy, D.L., Elias, J.H., and Walker, A.R. 1991, *AJ* **102**(3), 1118-1134

Suntzeff, N.B., Phillips, M.M., Elias, J.H., DePoy, D.L., and Walker, A.R. 1992, *ApJ (Letters)* **384**, L33-L36

Sunyaev, R.A., Kaniovsky, A.S., Efremov, V.V., Grebenev, S.A., Kuznetsov, A.V., Englhauser, J., Döbereiner, S., Pietsch, W., Reppin, C., Trümper, J., Kendziorra, E., Maisack, M., Mony, B., and Staubert, R. 1987, *Nature* **330**, 227-229

Sunyaev, R.A., Kaniovsky, A.S., Efremov, V.V., Grebenev, S.A., Kuznetsov, A.V., Englhauser, J., Döbereiner, S., Pietsch, W., Reppin, C., Trümper, J., Kendziorra, E., Maisack, M., Mony, B., and Staubert, R. 1990, *Soviet Astr. Letters* **16**(3), 171-176

Thielemann, F.K., Hashimoto, M., and Nomoto, K. 1990, *ApJ* **349**, 222-240

Trümper, J., Hasinger, G., Aschenbach, B., Bräuninger, H., Briel, U.G., Burkert, W., Fink, H., Pfeffermann, E., Pietsch, W., Predehl, P., Schmitt, J.H.M.M., Voges, W., Zimmermann, U., and Deuermann, K. 1991, *Nature* **349**, 579-583

Tueller, J., Barthelmy, S., Gehrels, N., Teegarden, B.J., Leventhal, M., and MacCallum, C.J. 1990, *ApJ (Letters)* **351**, L41-L44

Ubertini, P., Bazzano, A., Sood, R., Staubert, R., Sumner, T.J., and Frye, G. 1989, *ApJ (Letters)* **337**, L19-L22

Varani, G.F., Meikle, W.P.S., Spyromilio, J., and Allen, D.A. 1990, *MNRAS* **245**, 570-576

Whitelock, P.A. *et al.* 1988, *MNRAS (Short Communication)* **234**, 5p-18p

Whitelock, P.A. *et al.* 1989, *MNRAS (Short Communication)* **240**, 7p-24p

Wilson, J.R. 1982, In *Numerical Astrophysics, Proceedings of a symposium in honor of James R. Wilson held at the University of Illinois in October, 1982*, Centrella, J.M., LeBlanc, J.M., and Bowers, R.L. *ed.*, Johns and Bartlett Publishers, Inc., Boston, 422-434

Woosley, S.E., Axelrod, T.S., and Weaver, T.A. 1981, *Comments Nucl. Part. Phys.* **9**(6), 185-197

Woosley, S.E. and Weaver, T.A. 1986, *ARA&A* **24**, 205-253

Woosley, S.E., Pinto, P.A., and Ensman, L. 1988, *ApJ* **324**(1), 466-489

Woosley, S.E. 1988, *ApJ* **330**(1), 218-253

Woosley, S.E. 1990, In *Supernovae.* Springer-Verlag, Petschek, A.G. *ed.*, Ch. 1, 1-29,

Woosley, S.E. and Hoffman, R.D. 1991, *ApJ (Letters)* **368**(2), L31-L34

Xu, Y., Sutherland, P., McCray, R., and Ross, R.R. 1988, *ApJ* **327**, 197-202

Young, T.R. and Branch, D. 1989, *ApJ (Letters)* **342**, L79-L82